ANALYSIS OF PIEZOMETER MEASUREMENTS AND STRATIGRAPHY AT SUGAR LAKE DAM

by

CHRISTIAN DESJARLAIS

B.A.Sc., University of British Columbia, 2018

A THESIS SUBMITTED IN PARTIAL FULFILLMENT OF

THE REQUIREMENTS FOR THE DEGREE OF

MASTER OF APPLIED SCIENCE

in

THE COLLEGE OF GRADUATE STUDIES

(Civil Engineering)

THE UNIVERSITY OF BRITISH COLUMBIA

(Okanagan)

January 2022

The following individuals certify that they have read, and recommend to the College of Graduate Studies for acceptance, a thesis/dissertation entitled:

ANALYSIS OF PIEZOMETER MEASUREMENTS AND STRATIGRAPHY AT SUGAR LAKE DAM

submitted by Christian Desjarlais in partial fulfillment of the requirements of the degree of Master of Applied Science in Civil Engineering.

Dr. Dwayne Tannant, School of Engineering
Supervisor

Dr. Bernard Bauer, Irving K. Barber Faculty of Science
Supervisory Committee Member

Dr. Nicolas Paleato, School of Engineering
Supervisory Committee Member

Dr. Sunny Li, School of Engineering
University Examiner

Abstract

Piezometric measurements in the right abutment of Sugar Lake Dam read higher than the reservoir level and fluctuate seasonally with the operation of the reservoir. This thesis examines the influence of abutment geometry, stratigraphy, reservoir operation, and regional groundwater on the piezometric readings within the abutment. To complete this, a thorough review of the regional bedrock and glacial geology was completed, as well as of the right abutment geology and construction history. Field work consisted of site investigations on foot and by use of a UAV. UAV data was processed in Pix4D and ADAM 3DM software where photogrammetric methods produced orthophotos, digital elevation models, and joint set mapping.

Statistical analyses of historical piezometer measurements were conducted with the open-source software R. Time series decompositions, cross-correlation analysis, spectral decomposition, and Fourier coupled ARIMA modelling were completed. A 3-dimensional finite element seepage model, created within the Rocscience software RS3, was used to validate the physical assumptions of the inter-abutment relationships. The model geometry was created using the photogrammetry outputs and supplemented with LiDAR data. Borehole logs were also used to guide the construction of the subsurface geometry.

Results of the statistical and finite element modelling demonstrated that the regional groundwater levels are the driver for the elevated piezometer readings while the reservoir dominates the fluctuations. This is made possible by the stratigraphy of the abutment and the geometry of the dam and its appurtenant structures.

Lay Summary

Ground water levels in the right abutment of Sugar Lake Dam are higher than that of the reservoir level, a situation that is unusual considering the topography of the abutment and the distance of the piezometers to the reservoir. The reservoir level and the groundwater level fluctuate together. It is hypothesized that the regional ground water, combined with the structure of the soil layering in the abutment, causes this. A review of the geology of the area and the construction of the abutment was completed to gain further insight. This included both a literature review and field inspections. A statistical analysis took place with the goal of correlating the movement of the groundwater level with the movement of the reservoir level. To validate the statistical work, a computer model was created to simulate groundwater flow in the area.

Table of Contents

Table of Figures

Table of Tables

Acknowledgements

I cannot adequately express in words my appreciation for my thesis supervisor, Dr. Dwayne Tannant. You have been a constant inspiration both professionally and academically in terms of what it means to be a geotechnical engineer. Thank you for everything, both contained by this thesis scope and outside it.

This project would have not have been possible without the support of BC Hydro, in particular, Tom Stewart. His knowledge of the Sugar Lake Dam system and the data he shared, have been instrumental to the project's completion. Acknowledgement must also be given to Tolko Industries, facilitated by David Melville, for their contribution of the LiDAR data set of the Sugar Lake area.

Dedication

To my family, friends, and colleagues; without you, this work would have been competed two years sooner.

1 Introduction

Sugar Lake Dam is a storage dam owned and operated by BC Hydro, located north of Cherryville, British Columbia. The right abutment of the dam experiences changes in groundwater level that fluctuate seasonally with the reservoir level. Three piezometers installed in the right abutment of the dam often read higher total head than the reservoir level, which considering their proximity to the reservoir and the topography of the abutment, is unusual. The elevated phreatic surface throughout the abutment creates a large hydraulic gradient between the abutment and the dam tailwater. There is little observable lag between changes in the reservoir and piezometric levels when casually examining the data.

The piezometer readings are affected by local groundwater flow, abutment stratigraphy, reservoir level, and the geometry of the dam and appurtenant structures. The goal of this thesis is to explain the relationship between these system components. In particular, the mechanism that creates the observed head difference between piezometers and reservoir while allowing a unified fluctuation. A better understanding of the groundwater flow regime within the abutment facilitates a more robust dam safety system for BC Hydro.

1.1 Research Objectives

The thesis had the following research objectives.

- Determine general relationships between piezometer measurements, reservoir levels, time of year, and precipitation using appropriate statistical methods.
- Postulate an abutment stratigraphy contributing to the observed piezometric levels that is consistent with the available data.
- Validate the postulated abutment stratigraphy that causes unusual piezometric levels through 3D seepage modelling.

1.2 Research Tasks

The following tasks were completed to complete the research objectives:

- complete a thorough review of regional bedrock and glacial geology, examine the geology of the right abutment, and review the construction history and documentation

- complete fieldwork to supplement the above reviews and collect data for terrain analysis and model construction
- complete statistical analysis of the available data
- create a 3D finite element seepage model to validate the postulated causal mechanism.

2 Sugar Lake Dam

2.1 Location and Physiography

Sugar Lake Dam is located approximately 55 km east of Vernon, British Columbia. The dam impounds Sugar Lake on the Shuswap River. Sugar Lake acts as a storage facility for a downstream power generating station at Wilsey Dam, ensuring a consistent flow can be maintained through the station’s turbines (BC Hydro, 2014). Figure 1 shows the Sugar Lake Dam location on the Shuswap River.

Figure 1. Location of Sugar Lake Dam (Atlas of Canada, 2020).

Sugar Lake is located within the Shuswap River Highlands. The region is characterized by a moist climate and steep-sided valleys, with gentle to moderate rolling uplands (Demarchi, 2011). Topography varies from 600 m above sea level at the dam site to over 2400 m in the mountain peaks to the east and northeast of Sugar Lake. Moisture-laden Pacific air can move deep into western-facing valleys of the area; in other areas of the region, air currents rise over the region creating rain shadows or slopes with heavy precipitation (Golder Associates Ltd., 2012). Heavy snowfall in the winter is common, particularly when combined with cold Arctic air (Demarchi, 2011). The surface runoff of the area typically exceeds 1000 mm/yr (Golder Associates Ltd., 2012).

2.2 Dam History

Sugar Lake Dam, also known as Peers Dam, was originally constructed in 1929 as a 5.2 m high concrete buttress dam. No records of the original construction are available (BC Hydro, 2014). Over the years, the dam has been upgraded multiple times to keep up with continuously changing regulatory and safety requirements.

In 1942, the dam was raised to a height of 13 m and the crest extended to 150 m in length (HDR Corporation, 2013). In 1985, the left and right earthfill abutments, cut-off walls, and non-overflow sections were raised to accommodate the revised probable maximum flood event (BC Hydro, 2001). An aerial photo of the dam operating at low flow (21 m^3/s) is shown in Figure 2.

The dam maintains the reservoir's normal operating levels at elevations between 589.64 and 601.72 m (BC Hydro, 2005). The storage capacity of the reservoir is approximately 133.7 million m^3.

Figure 2. Aerial view of Sugar Lake Dam in October 2018.

When the dam was constructed in 1929 by the Canadian Hydroelectric Corporation, it was built upon a cataract of the Shuswap River downstream of Sugar Lake. The cataract was formed due to the presence of durable bedrock in the riverbed. Sugar Lake Dam was constructed upon this bedrock, and the dam abutments were formed in the overburden of the riverbanks. Except for cut-off walls, no special features were incorporated into the dam design to mitigate seepage through the abutments (BC Hydro, 1996).

2.3 Right Abutment of Dam

The general arrangement of the right abutment can be seen in Figure 3. The area of focus for this thesis can be seen in Figure 4. The right abutment of the dam is situated atop an old river terrace. The top of the terrace is at an elevation of approximately 605 m, which is approximately 20 m above the river level at the dam site. At the buttress base, where the abutment meets the dam, the top of the bedrock is at an elevation of approximately 595 m. About 25 m downstream, the top of the bedrock forming the right riverbank is at an elevation of approximately 598 m. A concrete and rock retaining wall, and a seepage cut-off trench, extend west and northwest from the buttress, respectively. A training wall runs parallel to the river protecting the right abutment from erosion by the dam outflow. Adjacent to the right bank, the ground slopes upwards at about 20° and is heavily forested. No bedrock outcrops are present in the immediate vicinity of the right abutment.

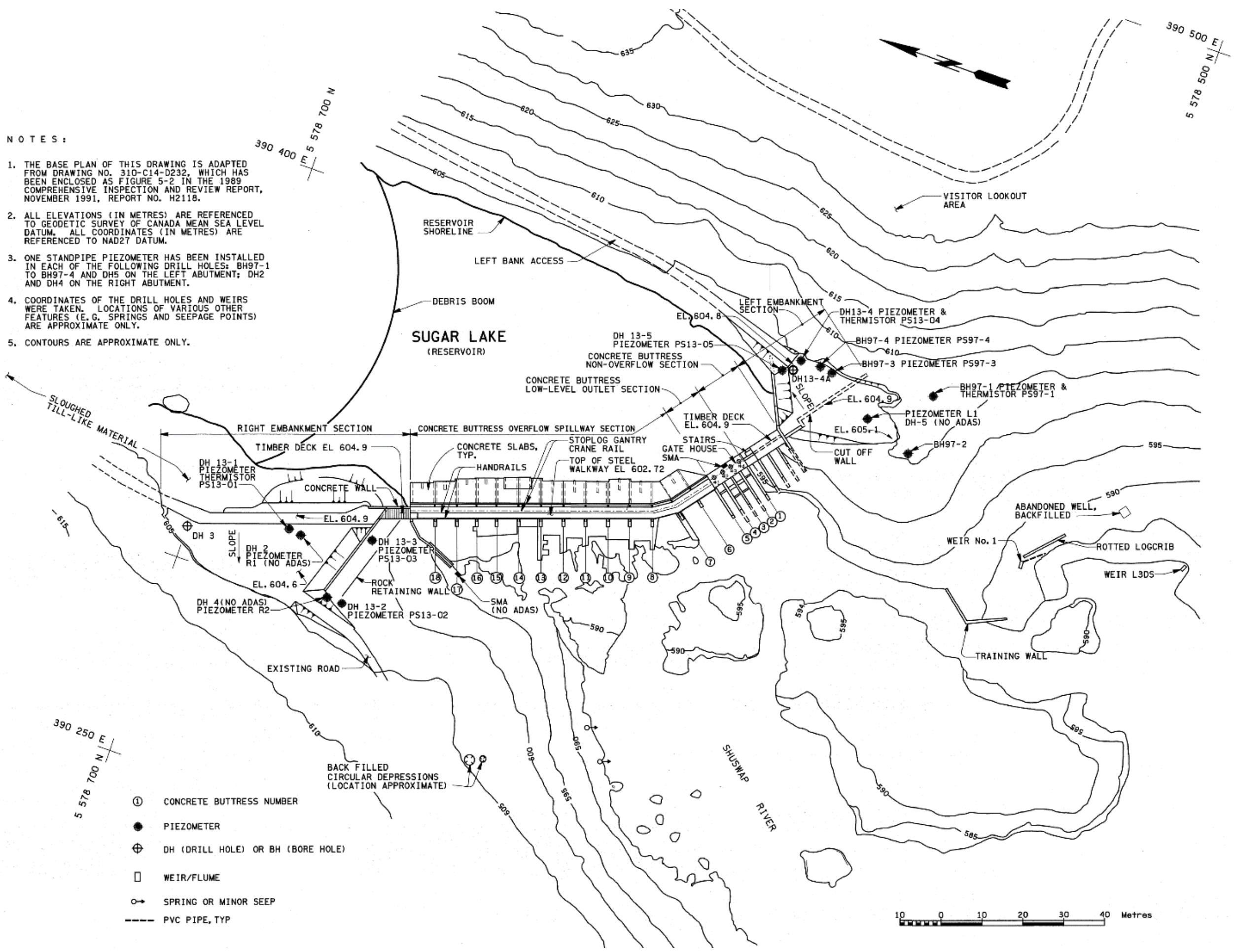

Figure 3. General layout of the Sugar Lake Dam site (BC Hydro, 2013).

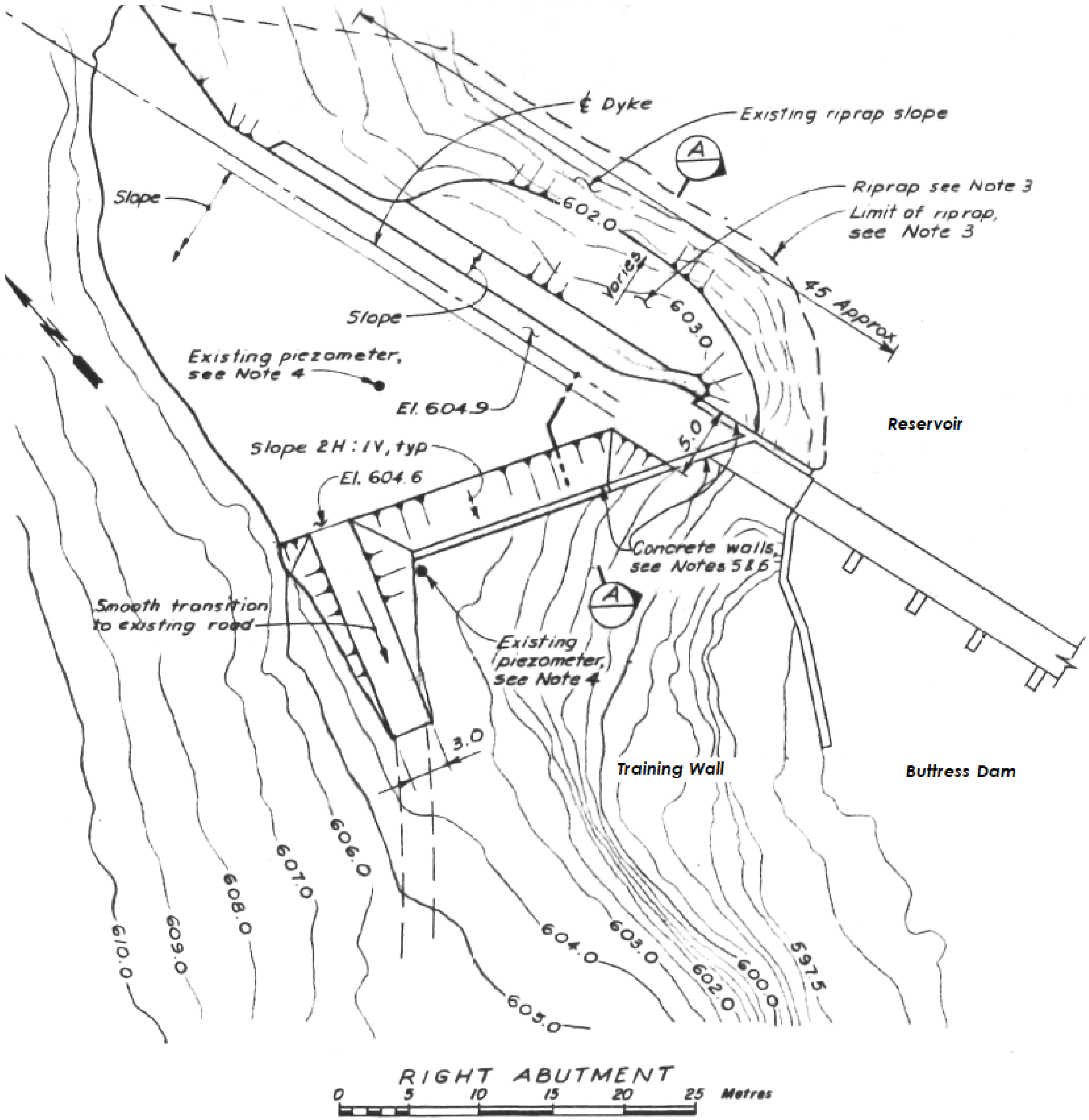

Figure 4. Plan drawing of the Sugar Lake Dam right abutment (BC Hydro, 1985).

At the time of construction in 1929, the dam was low enough that only relatively impermeable material was present below the reservoir level. When the dam was raised in 1942, permeable overburden material was exposed to the reservoir. The upstream concrete cut-off wall was constructed at this point, extending down to bedrock and hardpan materials. By 1952 the backfill around the concrete cut-off had eroded, and the cribbing was beginning to deteriorate. In 1963 rock backfill was added, and slope shaping was performed to provide protection. In 1985 the abutment, cut-off wall, and retaining wall were raised almost 2 m, and the upstream slope was armoured with riprap to provide protection during a newly calculated probable maximum flood event. Additionally, a 55-m long compacted till seepage cut-off was constructed across the length of the right abutment.

2.4 Seepage History

In the right abutment, seepage was considered negligible until June of 1974, when running water was detected. Simultaneously, a sinkhole that had been noted upstream of the seepage was showing signs of enlargement. By August, seepage had visibly increased. From 1974 until 1978, no further instances of seepage were recorded. During a highwater inspection in 1978, a line of seepage was observed. No flowing water was observed, but the sand was saturated, and minor slumping was taking place. During July 1990, at a reservoir elevation of 600.7 m, seepage flow was observed again, at rates up to 4 litres/min. Flows were clear, with no transported particles.

Dye testing, water constituent analysis, and water temperature measurements were performed as aids to identify the source of the seepage. Water temperature measurements showed the seepage flows to be about 10 degrees colder than water in the forebay. Trace ion analysis of water samples taken from both the seepage and the forebay indicated that the seepage water had ion concentrations 700 to 800% higher than the forebay water. The analysis showed a common source, but the reservoir water's lower concentrations suggest dilution by snowmelt and surface runoff. Ion concentrations of the seepage sample were assumed by BC Hydro to be typical for local groundwater.

Two depressions are present approximately 100 metres downstream of the dam and at an elevation of approximately 600 m. The origin of these depressions is unclear and appears to be unrelated to the sinkhole observed in the right abutment in 1974. In this area, a silty overburden overlies the bedrock, and only small seeps, originating from groundwater are present at the riverbank, as seen in Figure 3. These depressions do not appear to be sinkholes and have not shown activity in many years. It is BC Hydro’s guess that these depressions are remnants of past exploratory excavations for sandy construction materials. No further information was available regarding the aforementioned sinkhole, and the field investigation undertaken as part of this research did not reveal any evidence of it.

In 1985, two shallow standpipe piezometers were installed in the right abutment, downstream of the cut-off structures, to monitor the abutment seepage behaviour. Upon installation, the instrumentation indicated that piezometric levels in the right abutment were the same as the reservoir level and responded rapidly to reservoir fluctuations. The piezometer measurements suggested there must be a high hydraulic gradient in the small slope between the right abutment and the river. Monitoring the piezometers led to the determination that the 1985 cut-off was ineffective. At the time, it was considered likely that the seepage path was located at one or both ends of the cut-off wall.

In April 2013, improvements were made to the instrumentation and monitoring equipment of the dam abutments. At the time, the stratigraphy and seepage regime of the right abutment were poorly understood. The purpose of these upgrades was to better assess the relationship between the reservoir and the seepage regime. To accomplish this, real-time monitoring equipment was installed.

Three vertical drill holes were advanced into the right abutment, using a Prosonic Drill Rig DB-320 mounted on tracks. Continuous core samples were obtained from all drill holes. The drill holes were advanced using a 152 mm diameter casing with a 102 mm diameter core barrel. DH13-01 (P1) was drilled first, practically beside the existing piezometer DH2-R1, in the right abutment. DH13-03 (P3) was drilled second behind the retaining wall, while DH13-02 (P2) was the final hole drilled into the right abutment, just downstream of the existing piezometer DH4-R2. Figure 5 shows the installed piezometer locations.

Figure 5. Right abutment piezometer layout.

After installing the piezometers in 2013, unexpected piezometric levels were detected, with piezometer readings showing total head measurements higher than that of the reservoir. As seen in Figure 6 these elevated levels appeared to fluctuate seasonally with the reservoir level and responded almost immediately to reservoir fluctuations. All piezometer data such as elevation of piezometer tips, calibration of instrumentation, and proper operation of the system components were thoroughly reviewed to ensure these were not causing unexpected measurements. Manual measurements of water levels in the piezometers confirmed water level measurements by the new instrumentation.

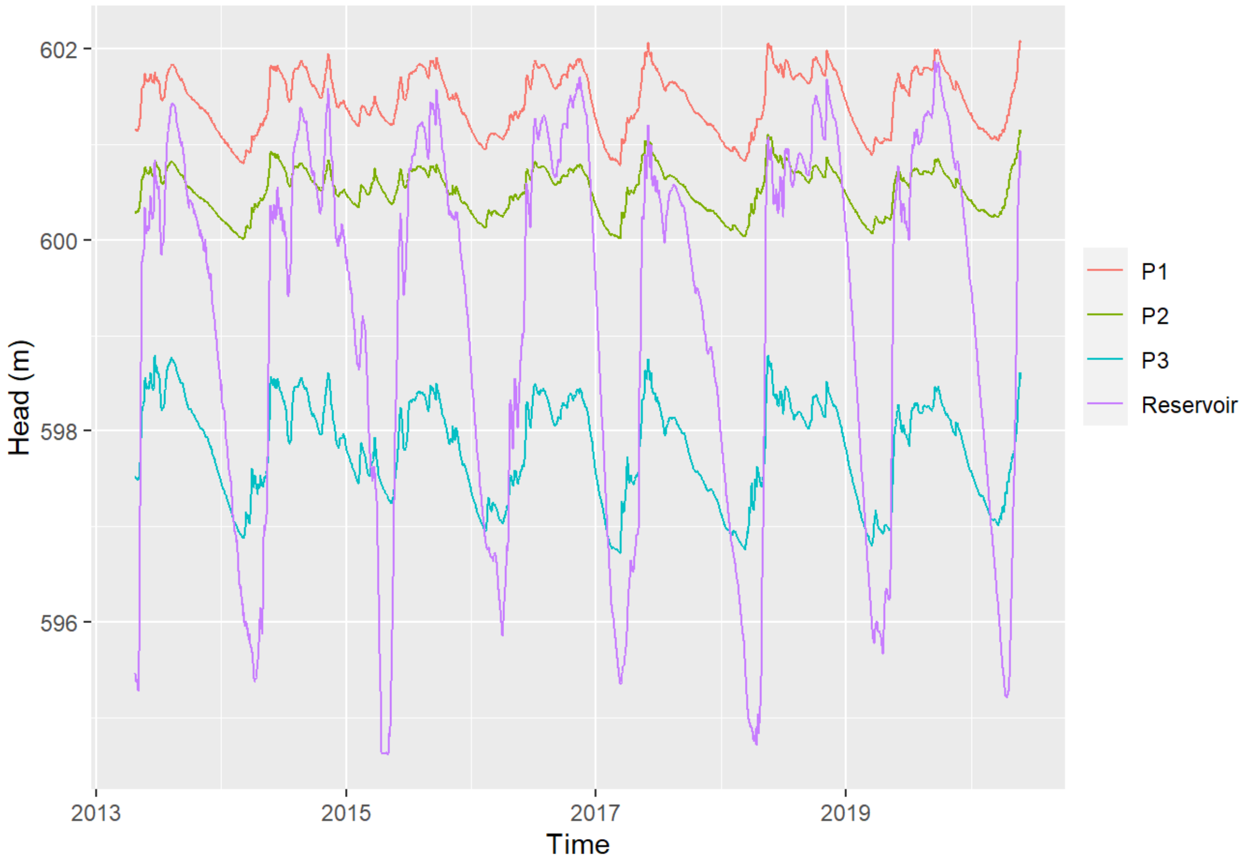

Figure 6. Right abutment piezometer and reservoir levels

3 Geology

3.1 Regional Bedrock Geology

During the Cretaceous and early Tertiary periods, the Shuswap area's general topography began to form through the compressional forces of plate tectonics causing the uplifting of the area’s mountains (EBA Consulting, 1998). During a long period of relative stability that followed, erosion and deposition formed a landscape with streams that generally followed lines of structural weakness (folds, contacts, faults). Uplift again dominated during the late Tertiary period, causing streams to cut down into the old erosion surface, forming steep-sided narrow valleys separated by gently sloping upland areas. The general geology is shown in Figure 7. The rock around Sugar Lake is comprised of the Shuswap assemblage, the Nicola group, the Monashee complex, and an unnamed stratigraphic unit (British Columbia Digital Geology, 2019). The east side of the valley is comprised of the unnamed stratigraphic unit, the Monashee complex, and the Nicola group. The west side of the Sugar Lake valley is composed almost entirely of the Shuswap assemblage. Remnants of flat-lying Tertiary volcanic rock can be observed on the surrounding mountain peaks (BC Hydro, 1996).

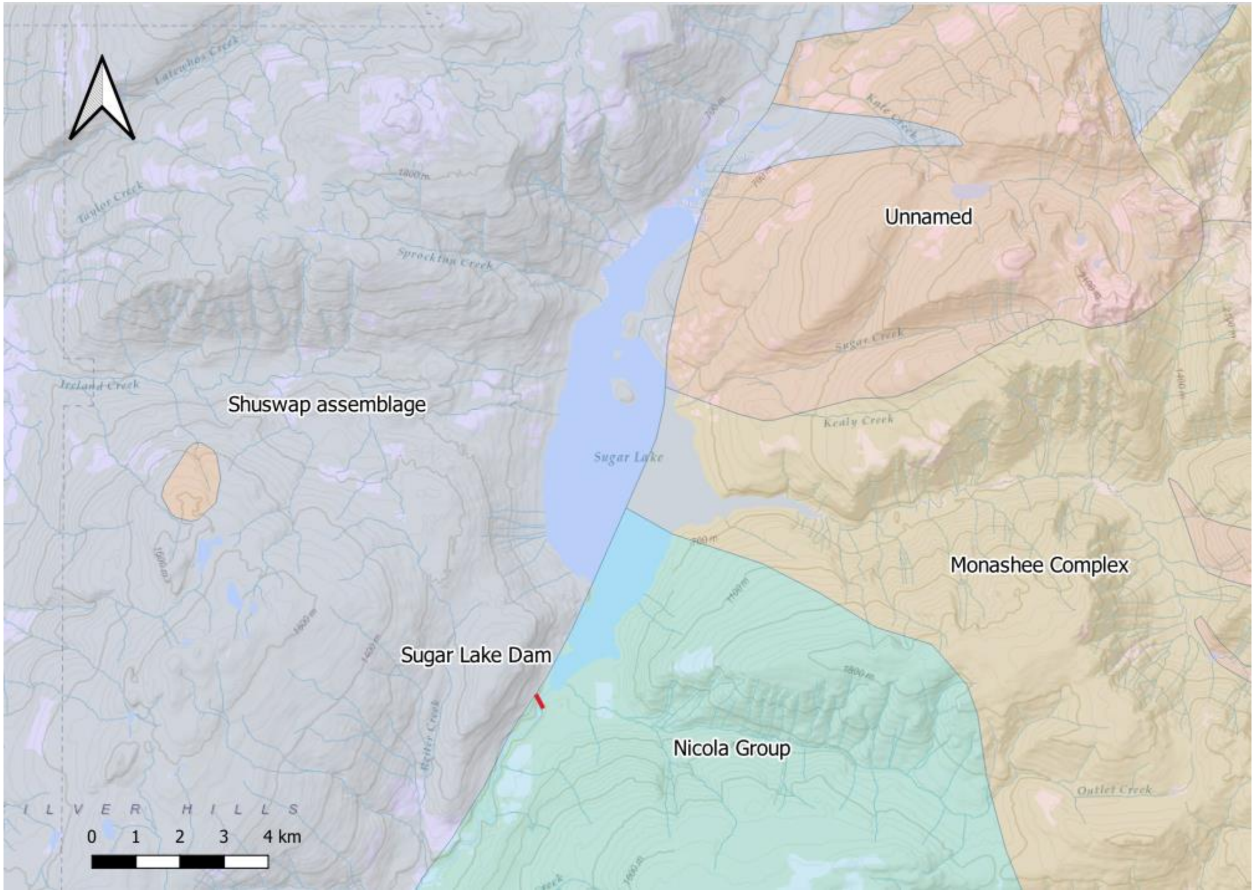

Figure 7. Sugar Lake bedrock geology (British Columbia Digital Geology, 2019).

The Nicola group is of the upper Triassic age and is composed of mudstone, siltstone, shale, and fine clastic sedimentary rocks (Schiarizza, 1996). Snow Mountain Schist has been identified within the Nicola group's mapped area and is assumed to be of the upper Triassic age. It is a predominantly coarse, black weathering, sillimanite-muscovite-biotite schist with minor quartzite interlayers from l to 200 mm thick. Schist identified on the shores of Sugar Lake contains staurolite crystals up to 15 cm long. The schist contains clean marble, quartzite, semi-pelitic layers, and minor felsic layers (Carr, 1989). The unnamed unit is of the late Paleocene to early Eocene age and comprised of granite, alkali feldspar granite intrusive rocks. Foliated plutonic rocks in the Mabel and Sugar Lakes areas are possibly of Jurassic age and thought to be extensions of the Eocene granitic suite (Okulitch, 1989). Rare areas of biotite-schist and muscovite-schist were also observed north of Sugar Lake in the Gates Creek area, as well as several minor crosscutting (younger) mafic dikes (EBA Engineering Consultants, 1999).

The Monashee Complex is of Proterozoic to Lower Paleozoic age and consists of paragneiss metamorphic rocks (Höy et al., 1994). There is a very weakly deformed pegmatite 10 km east of

Sugar Lake on Sitkum Creek that is 56.3 ± 0.5 Ma (Carr, 1989). These coarse-textured rocks disintegrate into a sandy residue that imparts a predominantly sandy texture to surficial material such as ablation till, glaciofluvial materials, and colluvium (EBA Consulting, 1998).

The Shuswap assemblage is of Proterozoic to Paleozoic age and is comprised of undivided metamorphic rocks (Schiarizza, 1996). Field observations indicated that both areas were dominated by leucocratic, medium to coarse-textured, massive, medium grey weathered, equigranular to locally porphyritic biotite- hornblende granitic rock and muscovite-granitic rock (EBA Engineering Consultants, 1999). In the Sugar Lake area, texture is predominantly a primary igneous fabric with westerly-directed discrete shear zones (Carr, 1989).

The Monashee decollement delineates the western boundary of the Monashee Group of rocks and has been mapped to follow the Shuswap River from the north end of Sugar Lake to Shuswap Falls. Where it has been exposed, the decollement is a mylonitic and brecciated fault zone (BC Hydro, 1996). Discrete 10 cm to 50 cm wide shear zones have been identified near Sugar Lake and in the Silver and Park hills between the Shuswap River valley and Mabel Lake. Asymmetry of mylonitic fabrics indicates a westerly-directed shear sense which may be related to the Okanagan fault zone (Carr, 1989).

The Geological Survey of Canada has mapped two regional faults in the vicinity of Sugar Lake Dam (BC Hydro, 1984). One has a predominately strike-slip displacement, tracing through the east side of the dam site, striking south-southwest, and dipping nearly vertical. The second fault traces about 4 km north of the dam and is truncated by the first fault near Sugar Lake's centre and, therefore, must be older (BC Hydro, 1984). Rocks on the shores exposed at low water levels show east-west trending stratigraphic units, contacts, and metamorphic isogrades. These features match on both sides of the lake (Carr, 1989).

3.2 Regional Surficial Geology

The region's most recent glaciation was the Fraser glaciation, peaking approximately 14,600 years before present. During this time, the Cordilleran ice sheet covered the land with a layer of ice up to elevations of 2000 m above sea level; this is evident by the rounded nature of the mountain peaks and ridges in the area (Holland, 1964). Glacier movement was predominantly south to south-southwest; this is evident based upon exposed bedrock throughout the region (Smith, 1969). An abundance of large-and small-scale directional features attests to the local control exerted by the valley topography on the southward-flowing ice.

Upland areas and valleys transverse to ice flow seem to have experienced little change. The area’s transverse valleys lack a distinctive U shape. The area's major valleys running parallel to ice movement experienced the most change; glaciation deepened and widened these valleys and over steepened their walls. Surficial materials within the area consist of a sequence of interglacial sediments, glacial deposits of the last stage of regional glaciation, and varied late-glacial and post-glacial fluvial and lacustrine sediments.

Sediments predating the last regional glaciation are comprised of a lower unit of coarse gravel, a middle unit of sand and silt containing shells of mollusks, lenses of peat, and a thin layer of volcanic ash, and an upper unit of gravel and sand (Smith, 1969). Radiocarbon dating ages the sediment to be of the Olympian Interglacial episode, occurring between 20,000 and 26,000 years before present (Armstrong et al., 1965). These deposits have been mapped at the north end of Sugar Lake, with the deposit being approximately 9 m thick.

Glacial till was deposited by the actively moving glacier during glacial advance and retreat. The material is assumed to form a continuous sheet within the area’s valleys and is generally mantled by younger fluvial and lacustrine sediments or alluvial fan debris (Smith, 1969). This material is only exposed in areas of erosion or excavation where overlying material has been removed. These morainal deposits consist of a very compact, unsorted, and unstratified mixture of pebbles and cobbles in a silt and sand matrix. The deposit can be as thick as 12 m, but within the valleys, it is generally in the range of 1 to 3 m (EBA Engineering Consultants, 1998). The thickness of the deposit in the uplands generally ranges from approximately 3 m to a thin veneer.

Olive gray to grayish brown morainal till occurs near the surface where conditions are dry, while moist material at greater depths is dark gray and somewhat softer. These deposits reflect the underlying bedrock, both texturally and compositionally. Pebble counts of deposits within the greater Shuswap area reflect the underlying bedrock's lithology (Smith, 1969). Morainal tills in the sugar lake area are composed of approximately 60% gneiss, 14% schist, and the remaining 26% of various other rock types.

Deposits accumulated during the late stages of glacial occupation and withdrawal experienced very different depositional environments than those described above. These late-stage deposits originated from conditions of stagnant or dead ice. During this depositional period, glacial ice was primarily confined to individual valleys while the uplands were free of ice. Meltwater played the dominant role in depositional mechanics; these sediments include materials deposited in streams and lakes surrounded by glacial ice, confined between ice and higher ground, or controlled by the presence of ice within the drainage system (Smith, 1969).

These glaciofluvial sediments initially accumulated atop stagnant or dead ice submerged beneath the water of an ice-dammed lake. Some of these deposits display distinctive ice contact topography. In contrast, others are perched on hillsides in positions indicating that the streams or lakes they accumulated in must have been confined by glacial ice (EBA Consulting, 1998). Deposits formed in contact with glacial ice are generally gradational into sediments deposited away from the direct influence of glacial ice.

Within the Sugar Lake valley, these deposits are mainly found in the form of kame terraces. North of Sugar Lake, prominent terraces occur along both sides of the valley, ranging from 23 to 46 m above the Shuswap River's current level. Smaller terraces have been observed at elevations of 210 m above the valley floor. Sediment from these terraces generally ranges from fine sand to small boulders (EBA Engineering Consultants, 1998). South of Sugar Lake, kame terrace deposits form a thick fill for approximately 6.5 km. These deposits are primarily composed of gravels and cobbles but include beds of silt and sand. The deposits are generally horizontally stratified though some display slumped and contorted bedding (Smith, 1969).

Post glaciation to the present, the area has mainly experienced down wasting of materials and accumulation of colluvium. Current dominant geomorphological processes are gully erosion and landslides. The once sediment-rich streams and rivers of the area have been cleaned out of finer sediments, and only gravelly beds remain.

3.3 Dam Site Geology

3.3.1 Bedrock Geology

At the dam site, bedrock consists of hard and generally sound, banded calcareous gneiss and quartzite, with outcrops exposed immediately downstream of the dam (BC Hydro, 1996). Foliation in the gneiss sequence strikes across the river and dips upstream at approximately 50 degrees (50°/050°). Exposed outcrops have a ribbed appearance due to variations in composition; the more calcareous beds are softer and less durable. Joints, fractures, and cleavages within the rock mass are generally either tight or have been rehealed, but occasional open features are present. A prominent joint set strikes northerly and dips steeply to the west

(80°/290°). A cleavage zone consisting of closely spaced, healed or hairline joints was mapped downstream from the dam and traces diagonally under the dam. In the area of the cleavage zone, the cleavage and foliations cut the rock into small (0.3-1.0 m) tightly interlocked blocks (BC Hydro, 1984).

Photographs from 1961 showing the dam at a low reservoir level indicate that the right abutment is embedded against good to fair quality rock (BC Hydro, 1984). The bedrock profile along the dam centreline is shown in Figure 8, and the profile through the right abutment, in a roughly north to south direction, is shown in Figure 9.

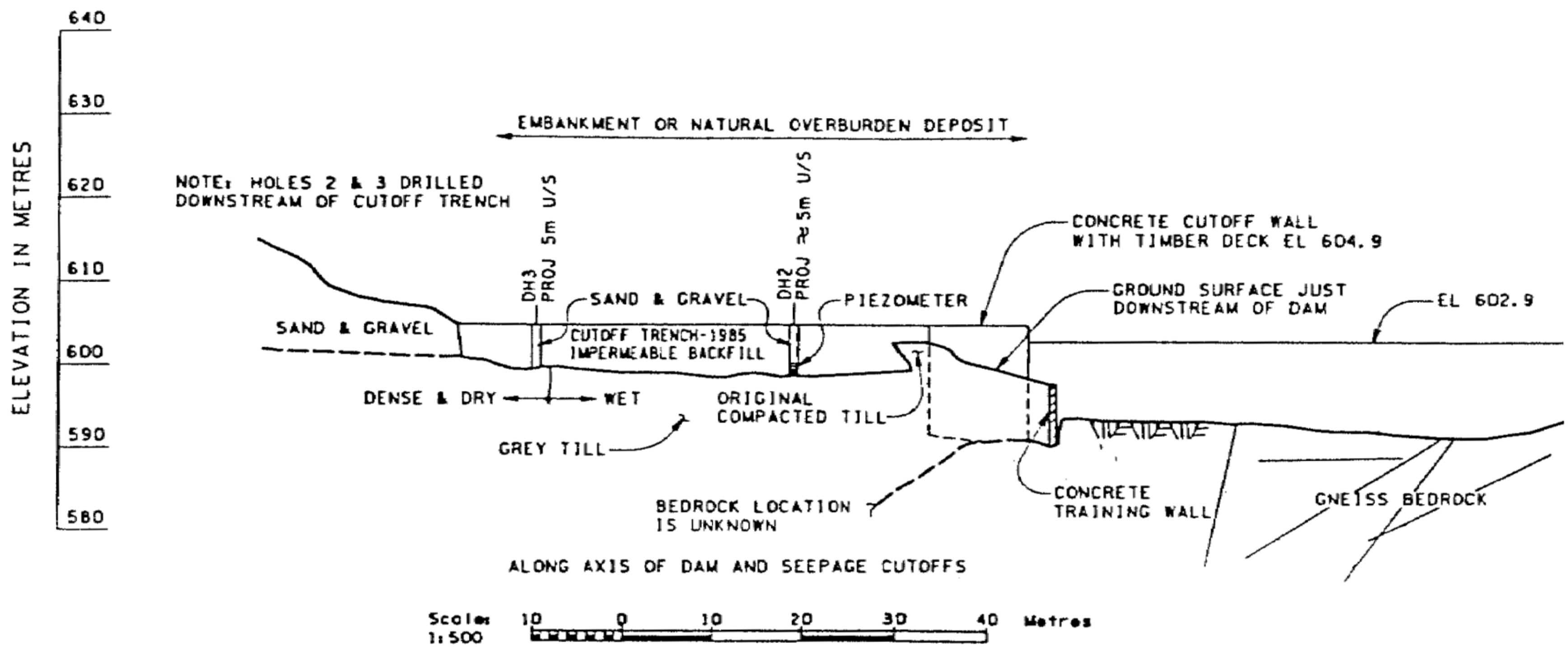

Figure 8. Bedrock profile through Sugar Lake Dam (BC Hydro, 1996).

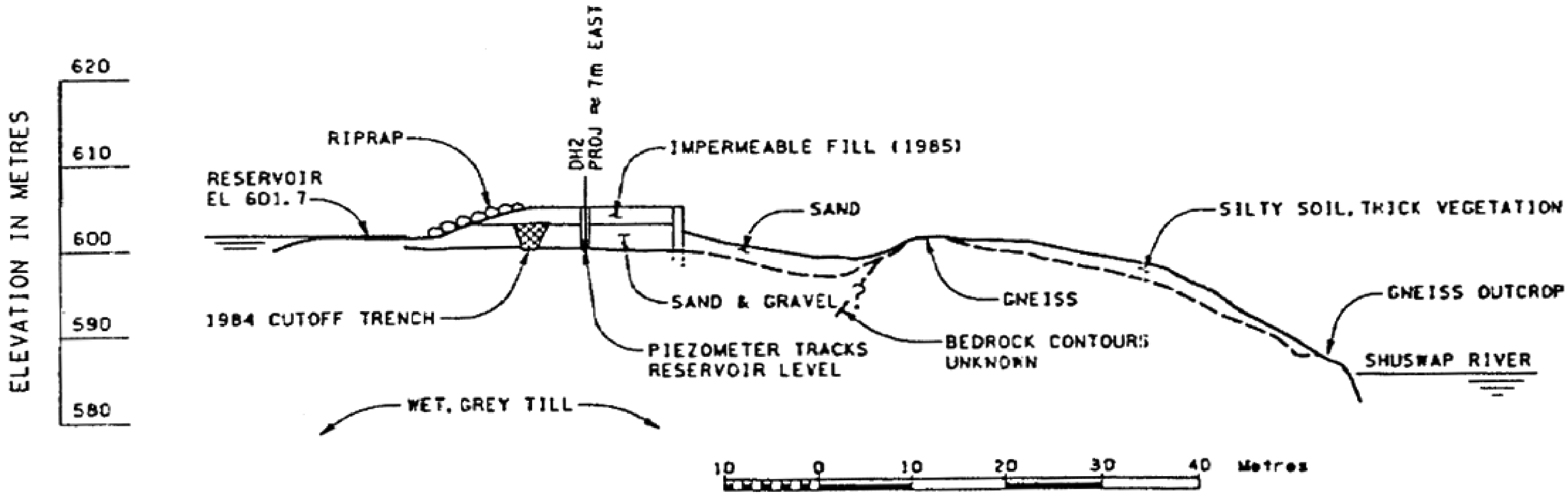

Figure 9. Sugar Lake Dam right abutment bedrock profile (BC Hydro, 1996).

The Monashee decollement defines the western boundary of the Monashee Group of rocks and passes through the dam site. A 0.2 m wide healed mylonite zone and two fracture zones have been mapped 20 to 50 m downstream of the dam. Where it has been exposed elsewhere, the decollement is a mylonitic and brecciated fault zone. The dam is founded below this and not affected by it. If there were another shear like this under the dam's base, it would likely be well healed (BC Hydro, 1984). Although faults and minor mylonite zones have been mapped in the dam site's vicinity, no major cataclastic zone has been reported. Seismic monitoring has not indicated that the Monashee decollement is active (BC Hydro, 1996).

3.3.2 Right Abutment Surficial Geology

The overall stratigraphy of the right abutment is poorly defined. The right abutment is a terrace consisting of till overlain by alluvial deposits and fill. Construction documentation from the installation of the cut-off trench provides insight into the stratigraphy of the abutment. The trench where the till was placed and compacted was excavated to depths ranging from 2.5 to 4 m and founded in the existing till of the abutment. Two types of till were encountered during the trench excavation; dense, dry, blue-grey till and moist, grey till. Figure 10 and Figure 11 show drawings of the cut-off trench construction.

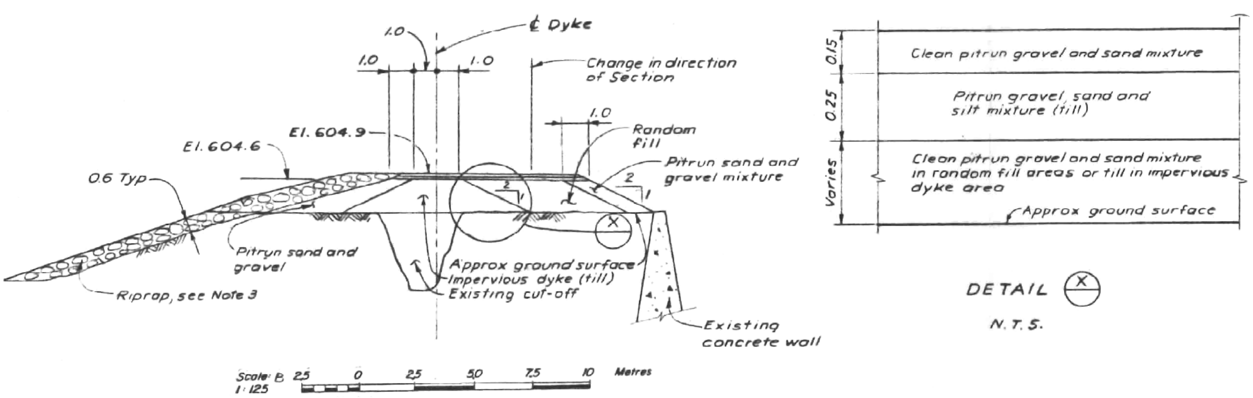

Figure 10. Cut-off trench construction drawing (BC Hydro, 1985).

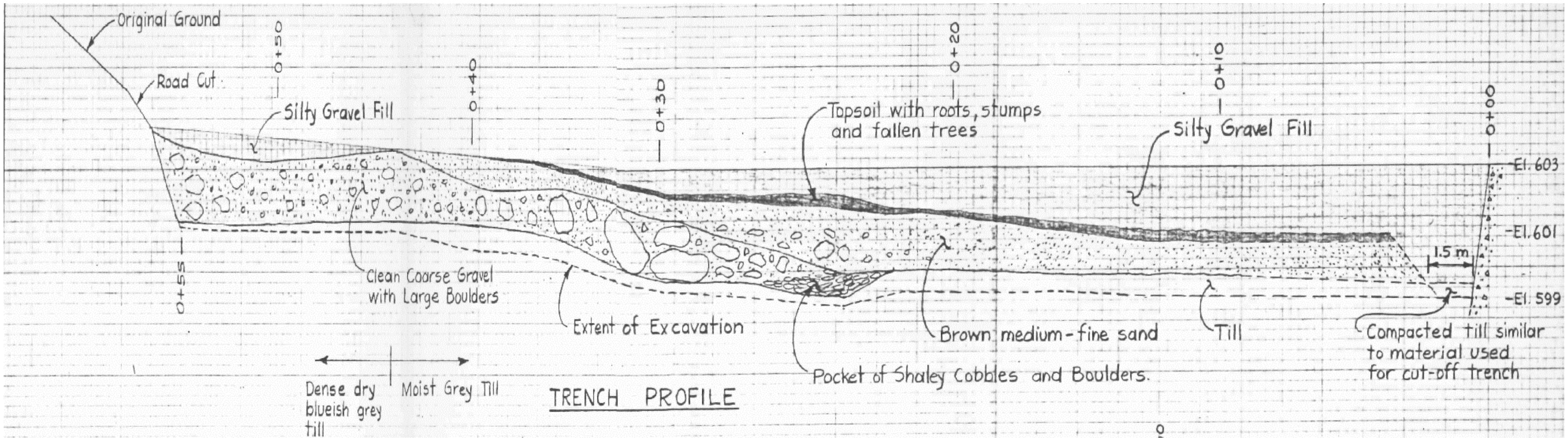

Figure 11. Cut-off trench construction drawing (BC Hydro, 1985).

Figure 11 provides the best insight into the upper stratigraphic layers of the right abutment. Based on this drawing, multiple stages of glaciofluvial sediments were deposited above the top of the till layer at approximately 599 m. Descriptions in the drawing indicate that a small meltwater channel, or possibly a side channel of a larger meltwater channel, flowed through the area that is presently the right abutment. The pocket of shaley cobbles and boulders at the low point of the till surface (0+25) highlight the possibility of this. The large boulders referenced at 0+30 are likely remnants of previously deposited ablation till, eroded by the meltwater, or remnants of colluvium.

During the piezometer installation in 2013, subsurface conditions were found to vary between the drill holes and with proximity to the cut-off walls and dam structure. Laboratory tests were completed on sampled soils. Sonic drilling is generally a wet vibratory method, and as such, moisture contents were only completed on samples from holes drilled without water (DH13-03). Sieve testing was completed at various depths of all holes; however, no hydrometer testing was completed. Atterberg limit tests were attempted on the finer fraction of several samples; none of the tests were successful due to a large fraction of angular sand in the samples. This indicates the finer fraction of the soil consists of silt. Full lab testing results are available in Chapter 9, while bore logs are presented in Figure 12, Figure 13, and Figure 14.

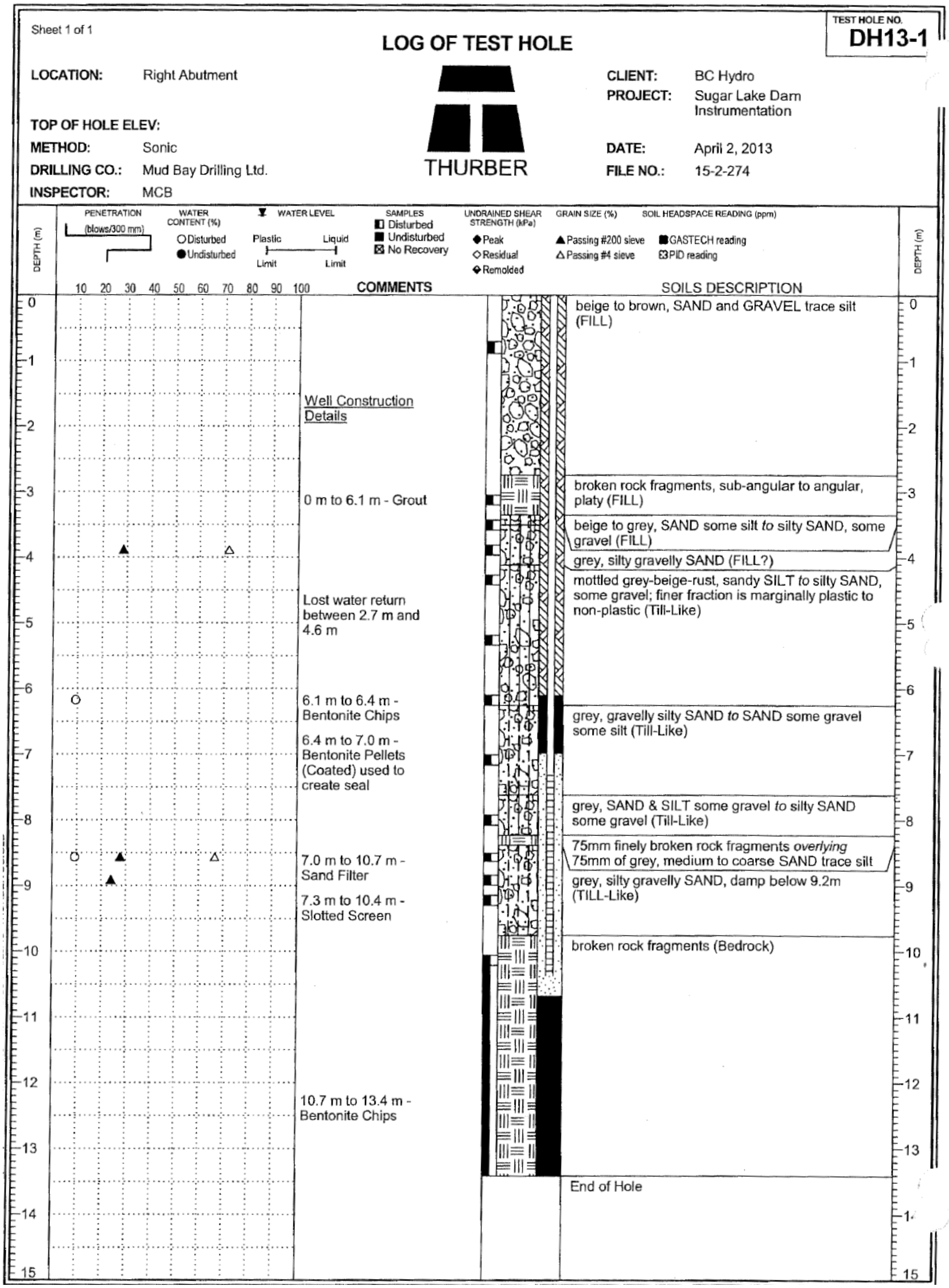

Figure 12. DH13-1 borehole log (BC Hydro, 2013).

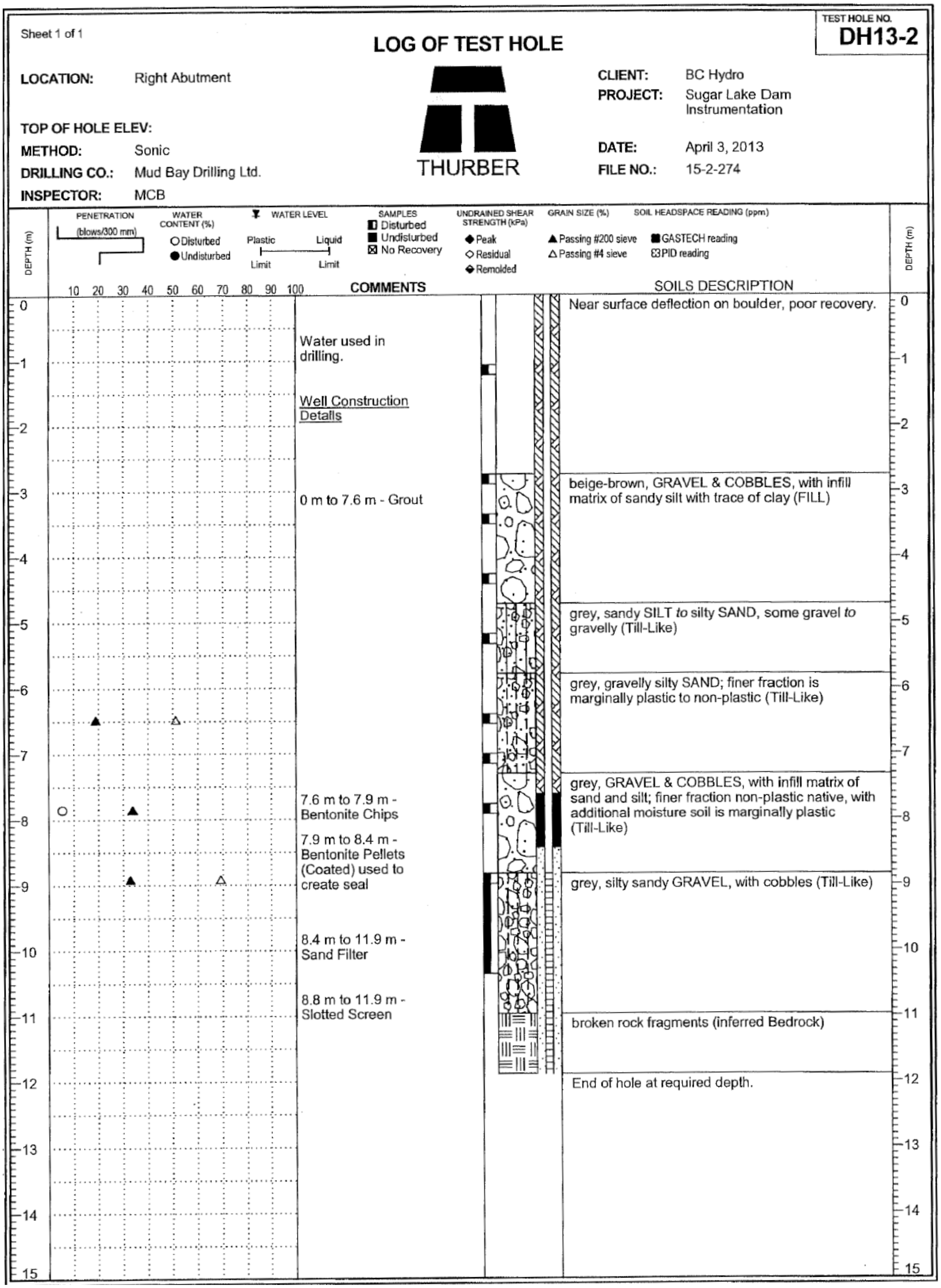
Sheet 1 of 1

TEST HOLE NO. **DH13-2**

LOG OF TEST HOLE

THURBER

LOCATION: Right Abutment

TOP OF HOLE ELEV:

METHOD: Sonic

DRILLING CO.: Mud Bay Drilling Ltd.

INSPECTOR: MCB

CLIENT: BC Hydro

PROJECT: Sugar Lake Dam Instrumentation

DATE: April 3, 2013

FILE NO.: 15-2-274

DEPTH (m) | PENETRATION (blows/300 mm) | WATER CONTENT (%) ○ Disturbed ● Undisturbed | Plastic Limit | Liquid Limit | WATER LEVEL | SAMPLES: Disturbed, Undisturbed, No Recovery | UNDRAINED SHEAR STRENGTH (kPa): ◆ Peak, ◇ Residual, Remolded | GRAIN SIZE (%): ▲ Passing #200 sieve, △ Passing #4 sieve | SOIL HEADSPACE READING (ppm): GASTECH reading, PID reading

10 20 30 40 50 60 70 80 90 100

COMMENTS

Water used in drilling.

Well Construction Details

0 m to 7.6 m - Grout

7.6 m to 7.9 m - Bentonite Chips

7.9 m to 8.4 m - Bentonite Pellets (Coated) used to create seal

8.4 m to 11.9 m - Sand Filter

8.8 m to 11.9 m - Slotted Screen

SOILS DESCRIPTION

Near surface deflection on boulder, poor recovery.

beige-brown, GRAVEL & COBBLES, with infill matrix of sandy silt with trace of clay (FILL)

grey, sandy SILT *to* silty SAND, some gravel *to* gravelly (Till-Like)

grey, gravelly silty SAND; finer fraction is marginally plastic to non-plastic (Till-Like)

grey, GRAVEL & COBBLES, with infill matrix of sand and silt; finer fraction non-plastic native, with additional moisture soil is marginally plastic (Till-Like)

grey, silty sandy GRAVEL, with cobbles (Till-Like)

broken rock fragments (inferred Bedrock)

End of hole at required depth.

Figure 13. DH13-2 borehole log (BC Hydro, 2013).

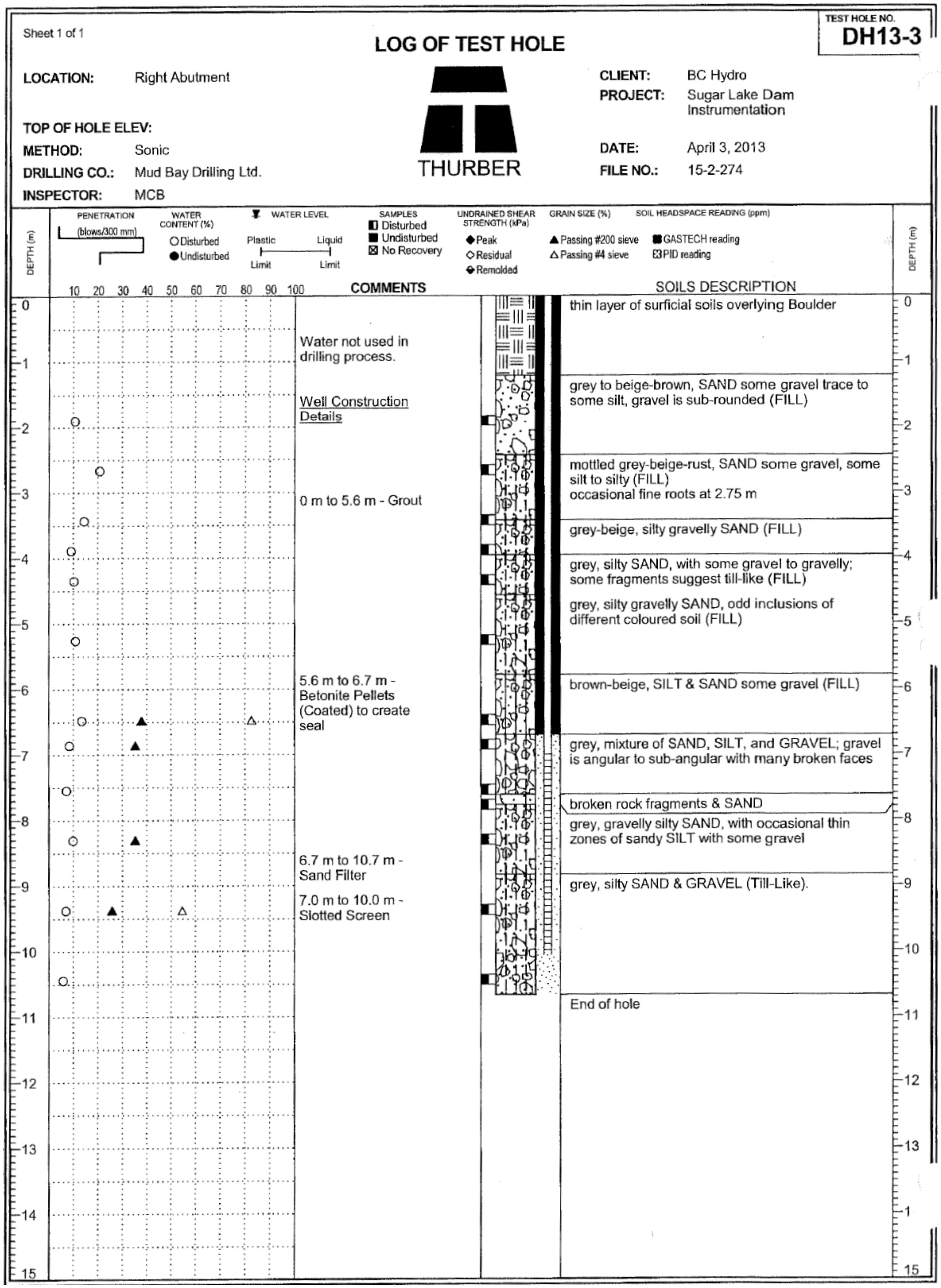

Figure 14. DH13-3 borehole log (BC Hydro, 2013).

Based on the laboratory test results, the soils present in the right abutment consist of gravels, sands, and silts. The presence of cobbles is noted at various depths within the borehole logs, but due to the nature of sampling, cobbles were not accounted for during sieve testing. Till-like materials are present at greater depths and in contact with bedrock. These discoveries agree with previous work completed on the abutment. In particular, the borehole logs support the geological interpretation depicted in Figure 11.

4 Field Investigation

4.1 Site Inspection

Field visits to Sugar Lake Dam were conducted on October 11, 2018, and May 23, 2020. The 2018 visit was conducted to examine the right abutment, dam and appurtenant structures, and the bedrock foundation at low water levels. The inspection was completed to capture aerial photos utilizing an unmanned aerial vehicle (UAV), to be used in a photogrammetric analysis. The 2020 inspection was completed to view the dam at high water levels and to examine evidence of seepage occurring in the right abutment.

4.1.1 October 11, 2018

On October 11th, Tom Stewart (BC Hydro) gave a tour of the site for Dwayne Tannant (UBC) and Christian Desjarlais (UBC) from approximately 11:00 am-2:00 pm. Weather was slightly overcast with occasional sunny breaks through the cloud cover; a layer of fog had been present in the morning but had burnt off on the drive to the site. Temperatures ranged from approximately 6-9°C during the site visit. The reservoir was at an elevation of 601.4 m, and outflow from the dam was approximately 21 m^3/s. Upon arrival at the site, a tailboard meeting regarding safety was conducted, and a tour of the dam was given by Tom Stewart. The UAV flight was subsequently completed.

4.1.1.1 Aerial Photography

A DJI Phantom 4 Pro was the UAV employed to capture images. The Phantom 4 is equipped with a 20-megapixel camera and a 1-inch sensor. Photos taken by the UAV's camera were at a 3:2 aspect ratio with 5472x3648 pixels and were taken with a calibrated focal length of 8.59 mm, an aperture of f/5.6, and at a shutter speed of 1/125-seconds. Dwayne Tannant operated the UAV under a Special Flights Operation Certificate, authorized through Transport Canada. Two separate flights were piloted; both flights were flown in a "free flight" pattern instead of a predefined flight path. Photos were taken in both oblique and vertical orientations.

During the first flight, 311 photos were captured from an elevation of 650-653 m above sea level (asl). The flight's goal was to obtain photos to be used to create a photogrammetric model to generate an orthomosaic photo of the dam area, a densified point cloud, and a digital elevation model (DEM) for survey purposes. The second flight was flown in a smaller, tighter pattern; 276

photos were taken from an elevation varying from 615-631 m asl. The purpose of this flight was to capture photos to be used for the analysis of the bedrock foundation at the toe of the dam, primarily mapping joint sets and their properties. Flying at a lower elevation enabled more details to be captured, allowing for a more accurate analysis of the rock faces. Additionally, oblique photos of the area were taken at a higher elevation, approximately 700m asl, to provide an overview of the dam and surrounding area and a regional perspective of the dam.

Processing of the photos was completed using Pix4D and ADAM 3DM software. Details of this procedure are available in Chapter 10. The photogrammetric modelling outputs completed on the higher flight using Pix4D were used to generate surfaces inputted into the seepage modelling software. These surfaces were also used to aid in the interpretation of the surficial geology of the right abutment. ADAM 3DM was used to analyze the lower flight and complete mapping of the bedrock foundation. Aside from the obvious benefit of having joint mapping, the joint set properties (orientation, spacing, and the number of joints) are required for the seepage model as they dictate the anisotropy of the rock’s permeability.

4.1.1.2 Ground Investigation

The right abutment was traversed by foot, as well as the terraced area downstream of the abutment. Large boulders of quartzite gneiss were observed along an old access road. Their sugary colour and granular texture are supposedly where Sugar Lake gets its name. It was found that the soil in the area of the previously noted depressions is shallow, with bedrock close below the surface. A large outcrop is seen below in Figure 15, with the sugary colour and texture shown in Figure 16. The inspection did not reveal the depressions themselves, and it was left undetermined if they were the results of groundwater springs or small test pits from the early dam construction. Additionally, the piezometers were measured manually. All information gathered while on-site validated that which was previously available.

Figure 15. Bedrock outcrop present downstream of the right abutment.

Figure 16. Sugary colour and texture of the right abutment rock outcrop.

4.1.2 May 23, 2020

An additional site inspection was conducted on May 23, 2020, during a period of high snowmelt and runoff, with the intent to investigate recent signs of seepage in the right abutment. At the time of inspection, the dam's reservoir level and outflow were 600.9 m and 179 m^3/s, respectively. The flow during the May 23 inspection was 8.5 times higher than the previous inspection in October 2018. Following a tailboard meeting led by Tom Stewart, a quick site investigation took place. In the week previous to the inspection, a small sinkhole had formed upstream of the cut-off trench. The sinkhole was approximately 0.65 m^2 and 0.5 m deep. Piezometers levels were measured and found to be within the range typical for that time of year, as was that of reservoir level. No indication of seepage downstream of the cut-off trench was observed.

4.2 Desktop Review

To supplement the completed field investigations, efforts to find a lidar data set of the site were successful. Tolko Industries provided a LiDAR data set encompassing the Sugar Lake area. The resolution of the DTM generated from the LiDAR data is 1m x 1m. Figure 17 shows an oblique view of the data set looking approximately north. As the LiDAR extends far beyond the dam site's immediate area, it is useful in validating the geological review undertaken in Chapter 3.

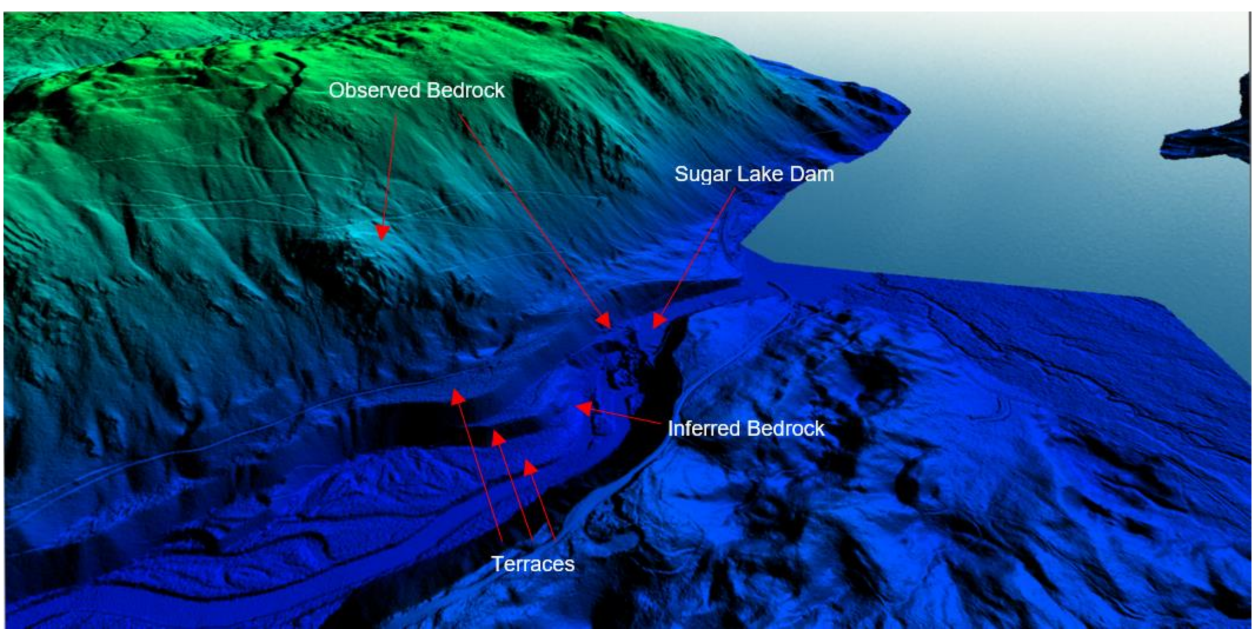

Figure 17. DTM overview of bedrock and terrace locations.

Bedrock was observed in the LiDAR at or near the ground surface at elevation ranges of 700 – 850 m and within the river bottom. Three prominent terraces were observed within the vicinity of the dam site. The presence of bedrock at or near the ground surface is also inferred to occur at the Shuswap River's first meander point. This observation is based on the river's erosional pattern; the river has eroded its way across the valley bottom. An erosion-resistant structure, such as bedrock, would have to be present to maintain the pronounced point.

Inspection of the LiDAR data set also identified three discernable slip surfaces on the slopes in the right abutment area. These three surface failures are shown in Figure 18. Two of the slope failures appear to have been triggered by the construction of access/forestry roads or the poor drainage practices associated with these roads. The failure directly above the right abutment appears to have been triggered by a spring, indicative of high groundwater levels. These surface failures have not been noted before and are a new addition to site history.

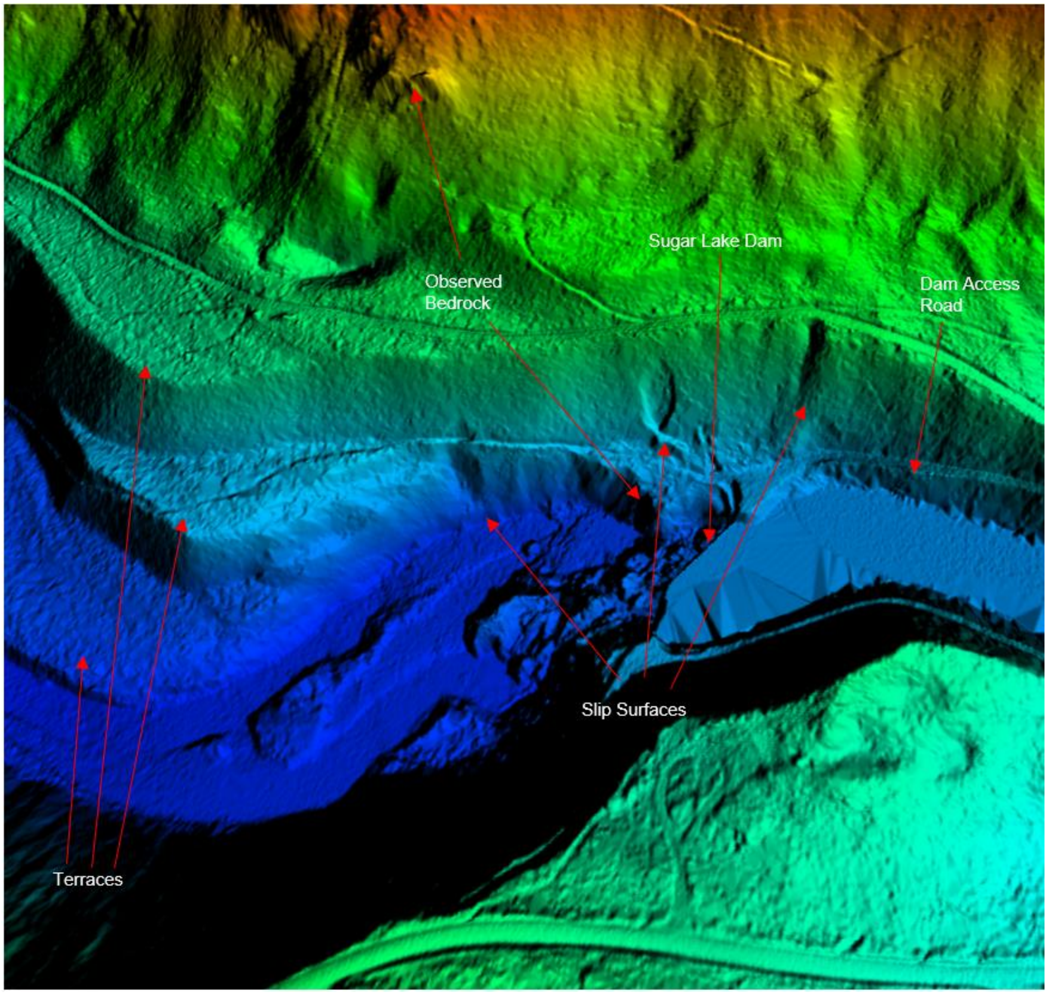

Figure 18. Identified slip surfaces within the right abutment vicinity..

5 Piezometer and Reservoir Data

5.1 Instrumentation

Available instrumentation data related to the reservoir and piezometric levels were reviewed. Instrumentation included the reservoir level gauge, the onsite rain gauge, and the right abutment piezometers. In 2013 improvements were made to the instrumentation at the dam site to understand better the relationship between the reservoir levels and seepage regime. This instrumentation update included adding a new rain gauge and piezometers in the left and right abutments. Figure 19 depicts the location of the reviewed instrumentation.

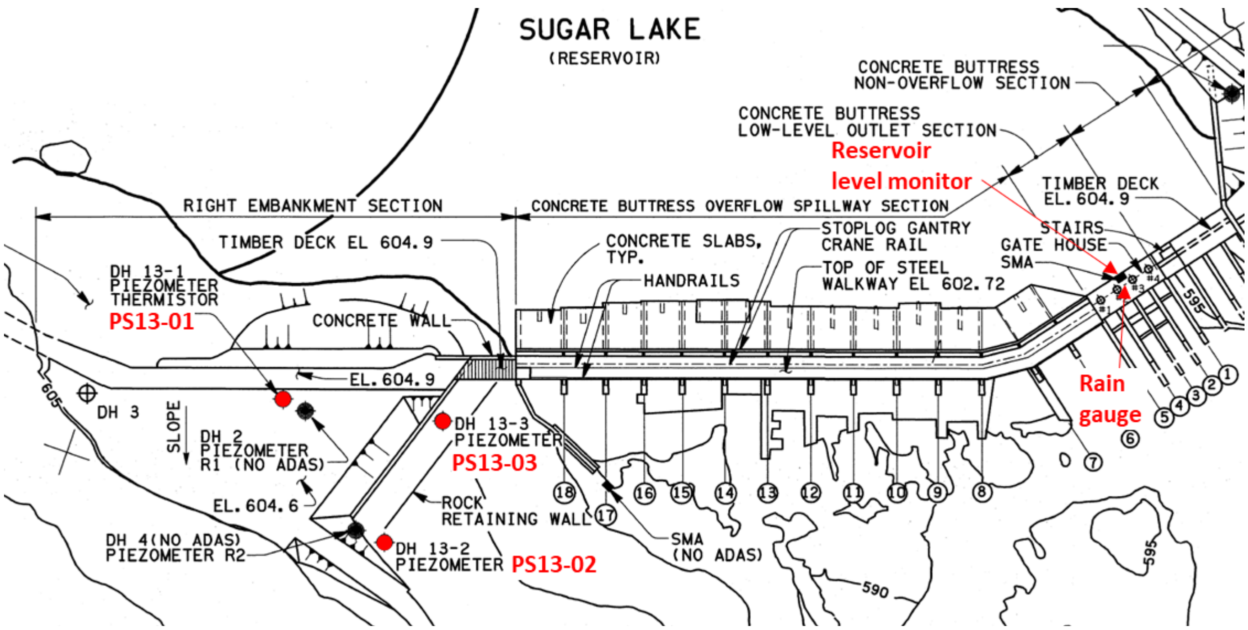

Figure 19. Instrument layout (BC Hydro, 2013).

The rain gauge installed in 2013 is a tipping bucket design with a 24.5 cm receiving orifice diameter and an 18.3 cm funnel depth. The gauge is mounted on an aluminum schedule 40 pipe, along with a radio receiver antenna and barometer. The aluminum mounting pipe is located on the dam crest, at the gatehouse.

The installed standpipe piezometers are constructed of 10-foot sections of 2-inch diameter flush thread schedule 80 PVC pipe. Standpipe screens consist of 10-foot slotted PVC sections. Piezometers were installed with filters consisting of 10-20 silica sand and are encased in coated bentonite pellets. Cement bentonite grout was used to backfill the holes to the surface. Drilling and installation of the standpipes occurred between April 2-5, 2013.

RST brand strain gauge pressure transducers were installed to measure the total head within the standpipe. The strain gauge piezometers have an output range of 4-20mA, correlating to a pressure range of 0-35 PSI (0-24.6m) above atmospheric pressure. The elevation of the tips of the tranducers are shown in Table 1. Calibration of the piezometers obtained full-scale errors within 0.005%. Calibration records for the piezometers and reservoir level instrumentation are available in Appendix B. Real-time results are logged to a FLEXDAQ Logger 1000 using an automated data acquisition system and transmitted to the Dam Safety division at the Revelstoke Dam.

Table 1. Elevation of transducer tips.

Piezometer	Transducer Tip Elevation (masl)
PS-1301	594.44
PS-1302	592.82
PS-1303	592.44

5.2 Measurements

After installing the piezometers in 2013 piezometer readings showing elevations higher than the reservoir level began to be recorded. These elevated levels appeared to fluctuate seasonally with the reservoir level and respond almost immediately to reservoir fluctuations. All piezometer data, such as elevation of piezometer tips, calibration of instrumentation, and proper operation of the system components, were thoroughly reviewed to ensure there were no errors. Manual measurements of water levels in the piezometers confirm water levels measured by the strain gauge piezometers.

Piezometric head data for the right abutment are available on a quarter-daily basis (every 6 hours) for all piezometers. In this thesis, the piezometer naming convention has been shortened from PS13-01, PS13-02, and PS13-03 to P1, P2, and P3, respectively. Reservoir-level data are available on an hourly basis. Hourly rainfall data and daily total rainfall are also available.

Data were selected for a seven-year period from April 26, 2013, at 00:00 to May 25, 2020, at 06:00. Next, the data were visually screened for missing data and abnormalities. Lapses in recordings were identified in all piezometer and reservoir data. The amount of missing data is shown in Table 2. Only daily data were analyzed to reduce computational time. Because there is little variation in the data within each day, the data at 00:00 were taken to represent the entire day. Missing data points were linearly interpolated. The data was converted into a time series object in R and set to a frequency of 365 to represent daily data. February 29 of leap years was omitted to make this an appropriate frequency.

Table 2. Data summary (April 26, 2013, to May 25, 2020).

Data Set	**Missing Points**	**Total Points**	**Percent Missing**
P1 Quarter Daily	180	10345	1.7
P2 Quarter Daily	80	10345	0.8
P3 Quarter Daily	68	10345	0.7
Reservoir Quarter Daily	127	10345	1.2
P1 Daily	49	2587	1.9
P2 Daily	24	2587	0.9
P3 Daily	21	2587	0.8
Reservoir Daily	36	2587	1.4

Figure 20 shows the piezometer and reservoir readings with respect to time. It can be seen that P1 is always above the reservoir, P2 is above the reservoir for the majority of the year, and P3 is generally below the reservoir level. This chart highlights the apparent unified fluctuation of the reservoir and piezometer levels. When observing P2 and P3, they appear most correlated when the reservoir level is above the piezometer level. As a general statement for all piezometers, there is seemingly a higher correlation between the reservoir and piezometer fluctuations at higher reservoir levels.

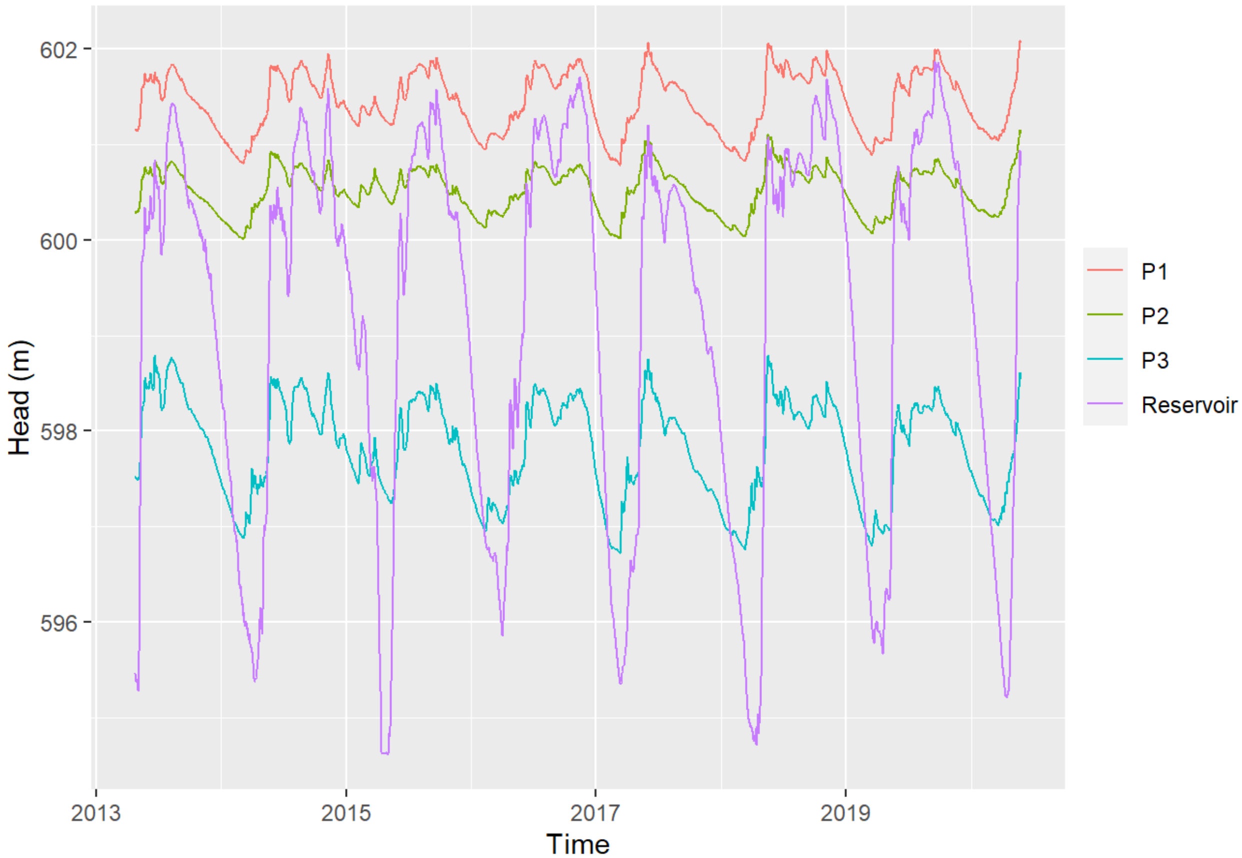

Figure 20. Piezometer and reservoir level versus time.

The available data is again plotted in Figure 21, this time as the piezometer level versus the reservoir level. The diagonal of this plot represents a 1:1 correlation. Data points to the left of the line represent periods when the piezometers are above the reservoir level, and data points to the right represent when the piezometers are below the reservoir. It can be seen that the data is more concentrated when the reservoir level is high; a broader, more distinct variation occurs in all piezometers below an elevation of approximately 599 m. This variation is seen particularly well in the P3 data. Additionally, the general trend of the data appears to change for each piezometer around this elevation. Again, this approximate inflection point is most prominently seen in the P3 data.

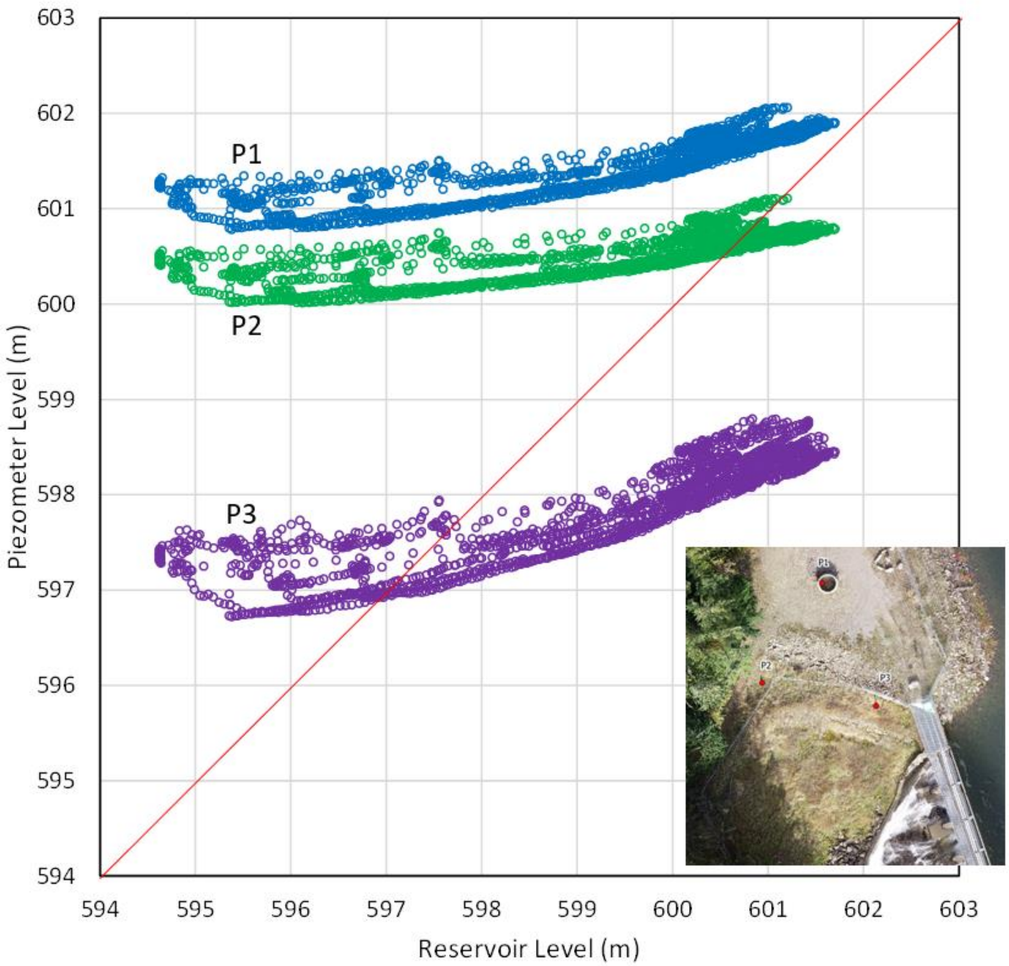

Figure 21. Piezometer level versus reservoir level.

5.3 Statistical Analyses of Data Sets

Statistical analyses were completed on the available piezometer, reservoir, and rain gauge data at the Sugar Lake Dam site. This was done to understand the interaction between the system components better and identify relationships not discernable by visual interpretation of the data. The results of these analyses support choices made during the seepage modelling completed in Chapter 6.

The piezometer, reservoir, and rainfall data were analyzed using the open-source program R (R Core Team, 2020). Packages used were the zoo, tseries, forecast, ggplot2, GGally, trend, modifiedmk fpp2, tidyverse, lubridate, dplyr, tsfeatures, reshape2, and lomb packages.

The minimum, 1st quartile, median, mean, 3rd quartile, maximum, variance, and standard deviation were calculated for each time series. These descriptive statistical parameters are listed in Table 3. It can be seen that relative to the piezometers, the reservoir has a much greater range of measurements. Additionally, the mean and medium of the piezometers are relatively the same, while the median is substantially larger than the mean of the reservoir elevation data. This is because the reservoir is typically operated with goal of maintain storage.

Table 3. Data statistics for the period April 26, 2013 to May 25, 2020 (heads in metres asl).

Data Set	**Min**	**1st quartile**	**Median**	**Mean**	**3rd quartile**	**Max**	**Variance**	**Standard deviation**
P1	600.8	601.2	601.5	601.4	601.7	602.1	0.099	0.315
P2	600.0	600.3	600.6	600.5	600.7	601.1	0.056	0.236
P3	596.7	597.4	597.9	597.8	598.3	598.8	0.274	0.523
Reservoir	594.6	597.5	600.0	599.2	600.8	601.9	3.976	1.994

The distributions of the raw data with a normal distribution overlaid are given in Figure 22. The piezometers levels do not follow a normal distribution very well. The distribution of the reservoir level is left-skewed. The reservoir level tends to be operated most frequently in the 600 to 601.5 m range.

The autocorrelation of the data was calculated to assess the data's dependence on itself. The presence of a trend component was determined using the non-parametric Mann-Kendall test, while the slope and magnitude of the trend were calculated using the Sen's Slope method. The Mann-Kendall and Sen's Slope tests were performed on both raw and pre-whitened data. All data sets were decomposed into three components, a seasonal component St, a trend component Tt, and a remainder component Rt using the STL method of decomposition. The distribution of the variances of the decomposed time series were compared between data sets.

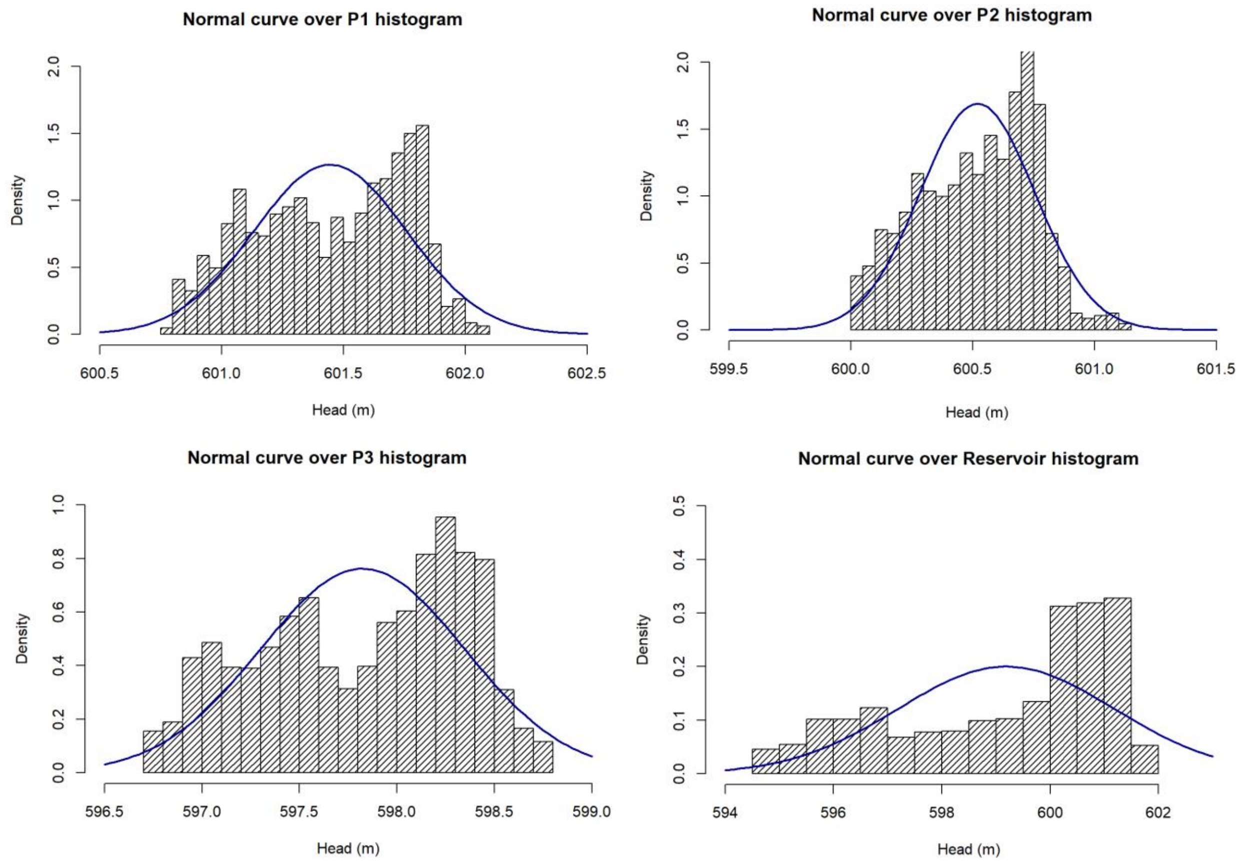

Figure 22. Dataset distributions with an overlaid normal distribution.

Spectral analysis was completed to determine any periodicity within the data, using the Lomb-Scargle method. Correlation and cross-correlation analyses were performed on the data sets. The data were analyzed for correlations and cross-correlations as a whole and during periods of rising and falling reservoir levels. Additionally, correlation and cross-correlation analyses were completed for periods when reservoir levels were below all piezometer heads.

ARIMA modelling was additionally completed as an alternative to STL decomposition. The data sets were fitted using a coupled Fourier model. The model was chosen based on the Akaike information criterion (AIC) and the Bayesian information criterion (BIC). ARIMA modelling allows for the decomposition of the time series where residuals can be analyzed for abnormalities. Full details of the statistical analyses are available in Appendix D.

5.4 Results and Discussion of Statistical Analyses

5.4.1 Rainfall Data

The interaction between rainfall and groundwater dynamics has been studied by many researchers (Kim and Lee, 2017; Cai and Ofterdinger, 2016; Scheliga et al., 2018). Rainfall data are available from the on-site rain gage at daily increments within the same period of the reservoir and piezometer data record. An impediment to this data set is that the tip bucket records throughout the winter and measurements of rainfall are indistinguishable from snowfall. Literature indicates that because of the close proximity of the piezometer locations to each other, any rainfall signal would be common to all piezometers, and as such, any variability can only be related to site-specific structural and functional variability of the hydrological processes (Delbert et al., 2016; Chiaudani et al., 2017). Based on this, in combination with the imperfect data set, no analysis of the impact of rainfall, snowmelt, or any other climatic data was pursued.

5.4.2 Piezometer and Reservoir Data

Autocorrelation testing showed that, as expected, all data sets display linear dependence and thus strong memory effects. By visual examination, a dominant yearly periodicity to the data is seen. The trend analysis using the Mann-Kendall test determined that P3 is the only data set with a significant trend with a calculated Sen's Slope of -1.34×10^{-4} m/day.

As expected, decomposition of the data using the STL method and subsequent component analysis revealed that the seasonal component in the data sets is much stronger than the trend component. The component analysis also clearly grouped the piezometers separately from the reservoir, with the reservoir being more dominated by its seasonal component than the piezometers. P2 was the least similar to the reservoir level in all cases, implying a relationship between reservoir distance and reservoir influence as P2 is located the farthest from the reservoir. The ratio of trend variance to total variance was negligible in all cases. Autocorrelation of the remainder component of the STL decomposition revealed structure was still present in the data set that was not accounted for by the trend and seasonality components.

Spectral analysis reinforced the presence of an overriding seasonality, showing a largely dominant period of one year for all raw data sets. A half-year period was also revealed to be statistically significant in all raw data sets. In contrast, a 2-year period was statistically significant in the raw piezometer data sets but not in the raw reservoir data set.

Correlation analysis revealed, as expected, that the piezometers and reservoir are all strongly correlated to each other. There is a relationship between the reservoir and piezometer correlation and the distance from the reservoir to the piezometer. The farther a piezometer is from the reservoir, the less correlated it is to the reservoir level. There is also a relationship between the inter-piezometer correlations. P2 has a weaker correlation to P3 than to P1. This relationship is most likely due to the change in stratigraphy between the three piezometers and, to a lesser extent on the effectiveness of the respective seepage barriers separating them. The stronger correlation between P1 and P3 is most likely due to their similar distance to the reservoir and the reservoir's influence.

Cross-correlation of the entire data set revealed that the reservoir response lags behind the piezometer levels by 5.25, 20.25, and 3.5 days for P1, P2, and P3, respectively. This lag appears to be correlated to distance, with P2 leading the reservoir by the longest time. A difference in lag times between the reservoir and P1, and the reservoir and P3, indicate differences in soil permeabilities in the general area, and therefore, a difference in the hydraulic efficiency of their connection to the reservoir. The time lag difference between piezometers is most likely caused by changes in stratigraphy and associated differences in hydraulic conductivity, as the piezometers are roughly equidistant from each other.

Correlation of the raw piezometer and reservoir level data during periods of rising reservoir level revealed no lag between any of the data sets, and they are all strongly correlated. During periods of falling reservoir level, there was no clear pattern to the correlations. The lack of a clear pattern is likely due to the yearly variation of how the reservoir is operated during the summer months. The cross-correlation results were again muddled for periods when the reservoir level was below all the piezometer levels. For the most part, with the exception of 2015 and 2017, the reservoir and piezometers are not correlated during these periods.

A coupled Fourier ARIMA model was found to fit the data sets well, and as such, was used to analyze their interrelations. Unlike the STL decomposition, the ARIMA model's residual component displayed no remaining data structure, indicating a better model fit. Because of the bitter model fitment, the ARIMA results were given precedence over that of the STL decomposition. During periods of the reservoir filling, cross-correlation results of the residual data were similar to the raw data cross-correlation values, exhibiting correlation coefficients between 0.65 and 0.89 at a lag of 0 days for all data sets. During falling periods, it was identified that the piezometers and reservoir were weakly correlated with little to no lag between data sets. During these periods, correlations between piezometers were generally high and occurred at a lag of 0 days. Correlations between piezometers when the reservoir was below all piezometer levels occurred at a lag of 0 days with correlation coefficients ranging from 0.4 to 0.85. Significant correlation between piezometer and reservoir levels was not identified during these periods.

6 Seepage Modelling

6.1 Introduction

The goal of the modelling was to explore and produce a simplified, steady-state, seepage model that could capture the interactions between the reservoir level, groundwater, and piezometer levels. Two-dimensional modelling was initially attempted, but due to the complex topography and stratigraphy in the region of the piezometers, 2D modelling was found to be inadequate in capturing the observed relationships between the reservoir level and piezometric heads. Therefore, a three-dimensional seepage model was created using the finite element modelling (FEM) software RS3 from Rocscience.

Finite element modelling is a numerical technique in which the solution to the governing general differential equation is obtained by an approximate solution. The law of conservation of mass for steady-state flow through a saturated porous medium requires that the rate of fluid mass flow into any elemental control volume be equal to the rate of fluid mass flow out of any elemental control volume. The equation of continuity for this case can be described as

$$-\frac{\partial(\rho v_x)}{\partial x}-\frac{\partial\left(\rho v_y\right)}{\partial y}-\frac{\partial(\rho v_z)}{\partial z}=0$$

Substituting Darcy's equation for specific discharge

$$v=-K\frac{\partial h}{\partial l}$$

yields the governing equation of steady-state flow through an anisotropic saturated porous medium.

$$\frac{\partial}{\partial x}\left(K_x\frac{\partial h}{\partial x}\right)+\frac{\partial}{\partial y}\left(K_y\frac{\partial h}{\partial y}\right)+\frac{\partial}{\partial z}\left(K_z\frac{\partial h}{\partial z}\right)=0$$

FEM is implemented by discretizing the soil volume into tetrahedron or hexahedron elements. In RS3, Galerkin's method of weighted residuals is used to solve the total head at each nodal point of the elements. Flow rates are then calculated through the nodal element faces. Boundary conditions constrain the model and allow for the solution of the governing equation. The observed relationships between the reservoir level and piezometric heads as determined by the statistical analysis in Chapter 5 were used to constrain and guide the seepage model development.

6.2 3D Seepage Model

6.2.1 Soil Interpretations

Based on the available background information, soils within the right abutment can generally be described as non-cohesive silts, sands, and gravels. Soils are described as being either "till-like" or "fill". Descriptors from the 2013 borehole logs are rather lacking, using the term till in a somewhat haphazard manner, with no description as to what till encompasses. A similar descriptive problem is encountered in the available drawings, as seen in Figure 8, Figure 9, and Figure 11. It appears that the use of the term till is based solely on the grey colouring of the soil, while alternatively, the term fill is based on brown colouring.

To interpret the borehole logs, the beige to brown soils were considered to be fill. These materials are assumed to be more or less uniform in terms of composition (i.e., grain size, void ratio, permeability, etc.) and their placement/compaction. They are considered to be primarily sands and gravels. The grey soil is considered to be till originating from glacial deposition. Based upon the logging descriptions in Figure 12, Figure 13, and Figure 14, and sieve testing in Appendix A, the till is generally interpreted to be sandy silt with gravel or silty sand with gravel. Unlike the soils considered to be fill, the till was not interpreted to be of uniform composition.

Examining the till layers of boreholes 1 (BH1) and 2 (BH2), it can be ascertained that a layer of higher permeability soil exists, sandwiched in between the upper and lower extents of the till. In BH1, the layer from a depth of 6.3 m to a depth of 7.6 m is described as predominately sand. Another layer in BH1, from a depth of 8.2 to 8.4 m, is described as consisting of rock fragments and coarse sand. Considering the lack of fine-grained material described within these zones, both layers are considered more permeable than the other till layers. In a similar fashion, the layer in BH2 described as consisting predominately of gravels and cobbles, from a depth of 7.3 to 8.8 m, indicates a higher permeability layer. BH3 does not have any indication of a layer of higher permeability till, although the layer of fill over laying the till is much thicker than that of BH1 and BH2.

It is assumed that the higher permeability layer present in BH1 and BH2 was deposited during a period of relatively higher energy meltwater flow and is from here on termed the "fluvial" layer.

This would explain the decreased fines and higher proportion of gravels and cobbles in this layer. Lenses of higher permeability soils are commonly seen in glacial deposits. A 3D interpretation of the layering, using a linear approximation between boreholes, is shown in Figure 23, with the yellow layer being fill material, the blue layers being till material, the orange layer being the fluvial material and the grey layer being bedrock.

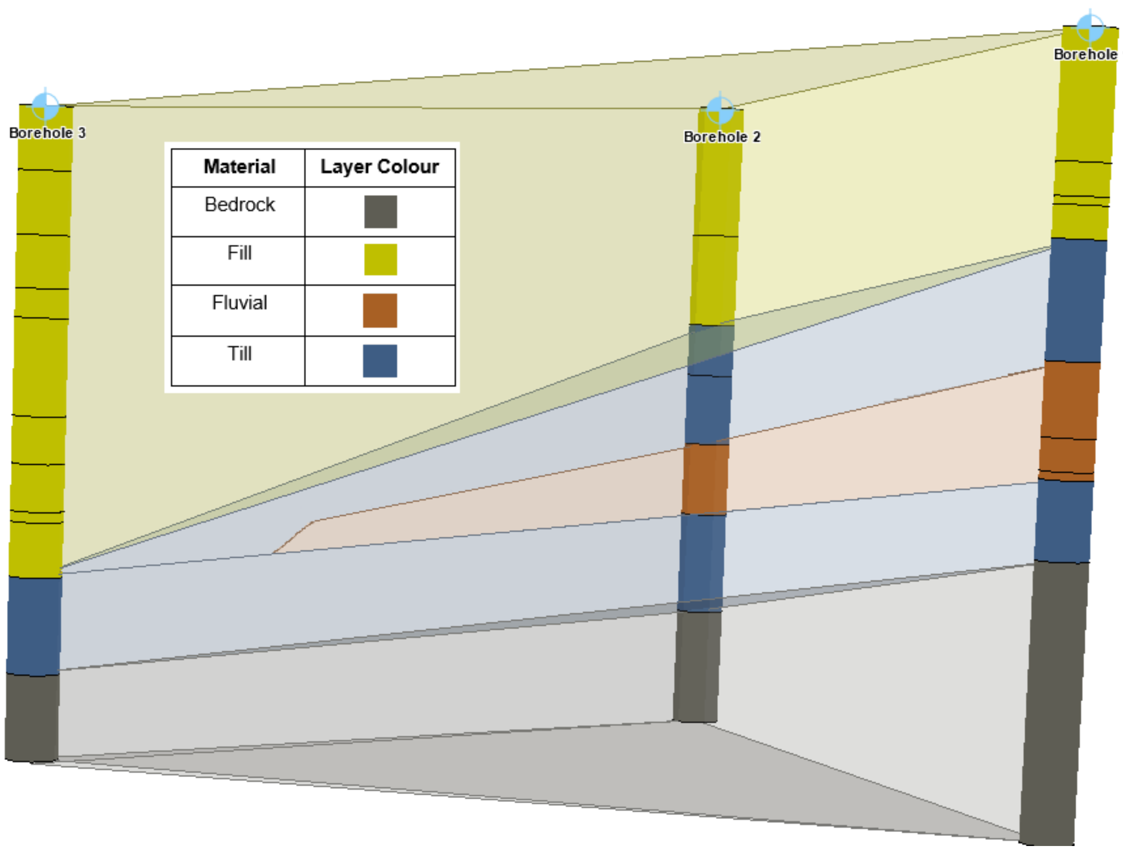

Figure 23. 3D borehole log interpretation.

The geometries of the dam buttress and concrete cut-off wall were determined using Figure 8. Where the concrete cut-off wall meets the right abutment, there is an area of non-bedrock contact. This lack of a concrete foundation to bedrock contact was included in the geometry of the model, as it creates a more direct seepage path from the reservoir to piezometer 3. The concrete retaining wall was constructed using the geometry in Figure 10. It was assumed based on this drawing that the wall terminates at a depth deeper than the soil cut-off trench, and as such, the top of till layer in the vicinity of the retaining wall reflects this. The exception to this is near BH3, where till is not present in the borehole log at this elevation.

The soil cut-off trench was constructed based on the information in Figure 10 and Figure 11. The drone imagery and generated DEM, along with the supplied LiDAR data, were used to create the surface of the model as well as the training wall, as no design drawings were available for this structure. Field investigations verified that the training wall is founded upon bedrock, the elevations of which were taken from the DEM.

6.2.2 Boundaries Between Different Materials

The seepage model geometry was constructed using the interpreted borehole data, historical drawings and surveys, drone imagery, and LiDAR mapping. The extents of the seepage model are shown in Figure 24. Points files with northing, easting, and elevation attributes were created in QGIS using the drawings, orthophotos and lidar to guide the spatial extents of the dam and appurtenant structures, as well as the abutment soil and rock layers. Points were assigned to create upper and lower surfaces for the dam, training wall, and retaining wall. Soil and rock layers within the abutment were created in the same manner. Coordinates for a ground surface layer, overburden layer, till layer, fluvial layer, bedrock layer, and cut-off trench were obtained.

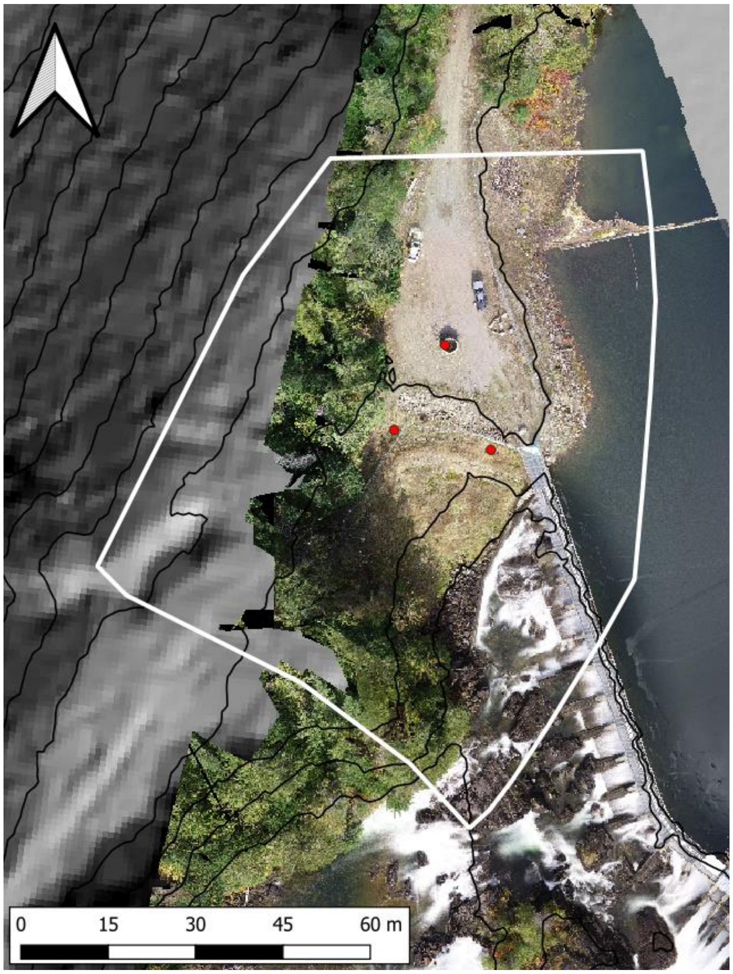

Figure 24: Seepage model extents.

These points were then imported into AutoCAD Civil 3D. TIN surfaces were created from the points, using break lines and boundaries to control the spatial extents of the surface triangulation. The created surfaces were then extruded into solids, representing the 3D geometric components of the model. The solids were then imported into RS3.

RS3 uses Boolean algebra to generate the model geometry. The ground surface volume created in Civil3D was set as the external volume. The dam, training wall, and retaining wall structures were added to the external volume. Following this step, the 'divide all' function was used to create different segmented volumes, representing the stratigraphical units. The various volumes were then assigned as different materials. An oblique view of the created model can be seen in Figure 25.

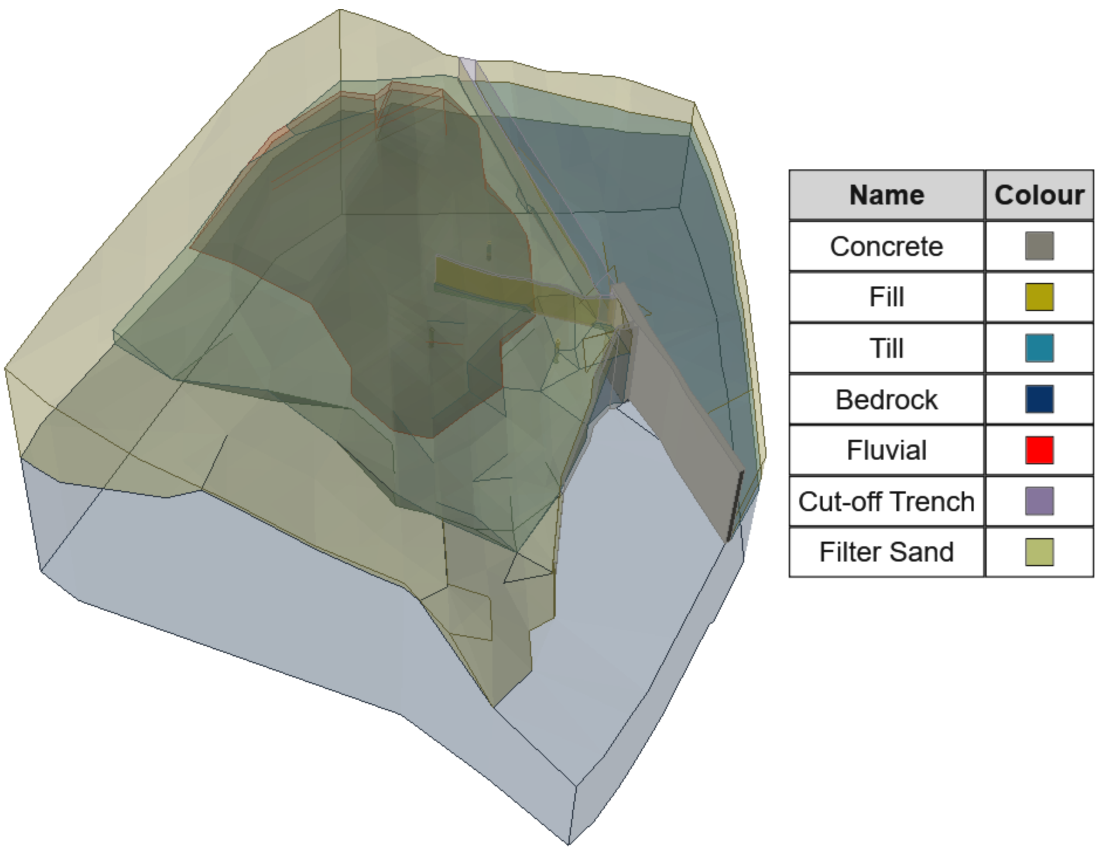

Figure 25. Oblique view of RS3 model geometry.

The 2D vertical cross-sections in Figure 26, Figure 27, and Figure 28 are taken through the piezometer locations. They represent the soil geometry between the boreholes, as seen initially in Figure 23. Additionally, the filter sand surrounding the piezometers was incorporated into the model geometry. For the seepage modelling, results for the piezometer head were taken at the coordinate corresponding to the centre of the piezometer screen in each piezometer.

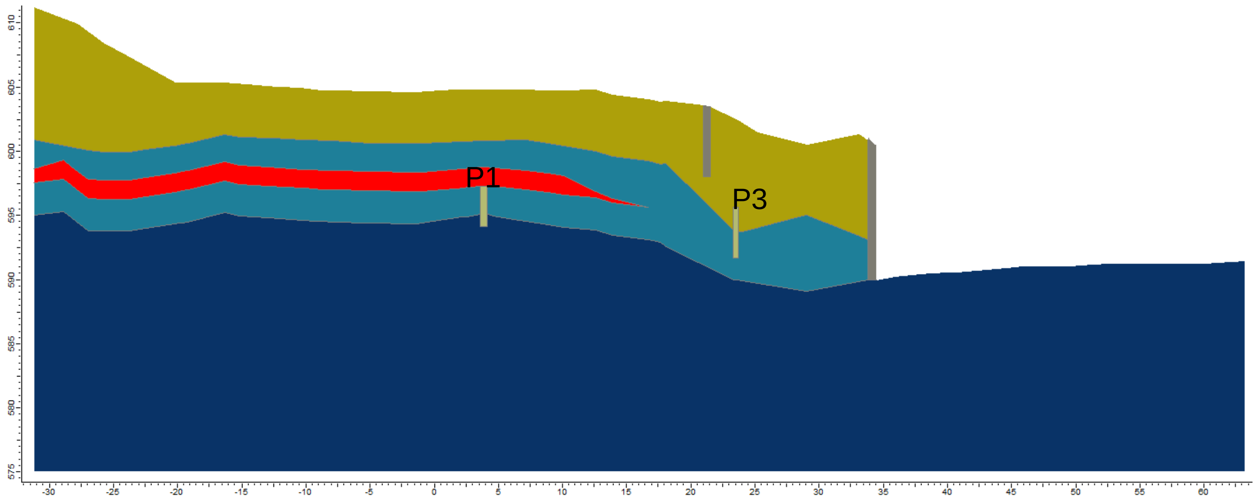

Figure 26. Cross-section from piezometer 1 to piezometer 3.

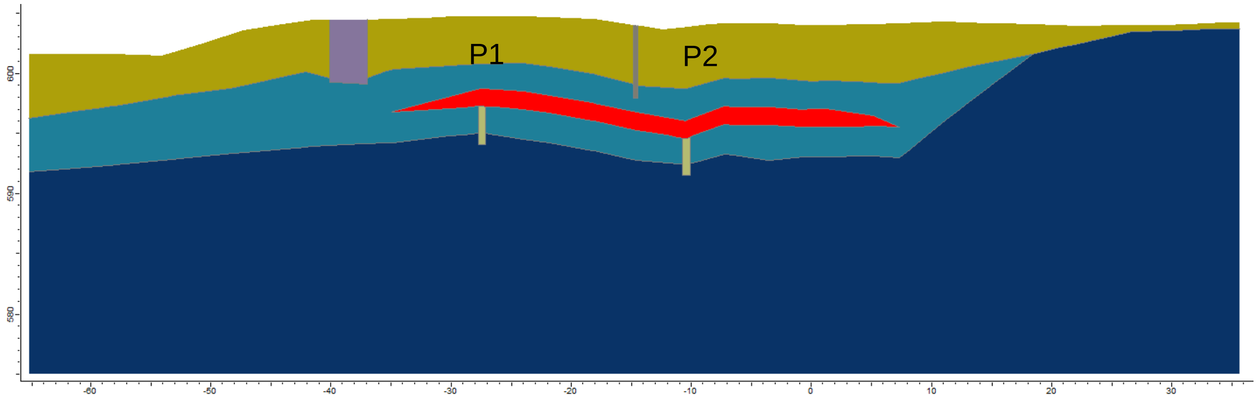

Figure 27. Cross-section from piezometer 1 to piezometer 2.

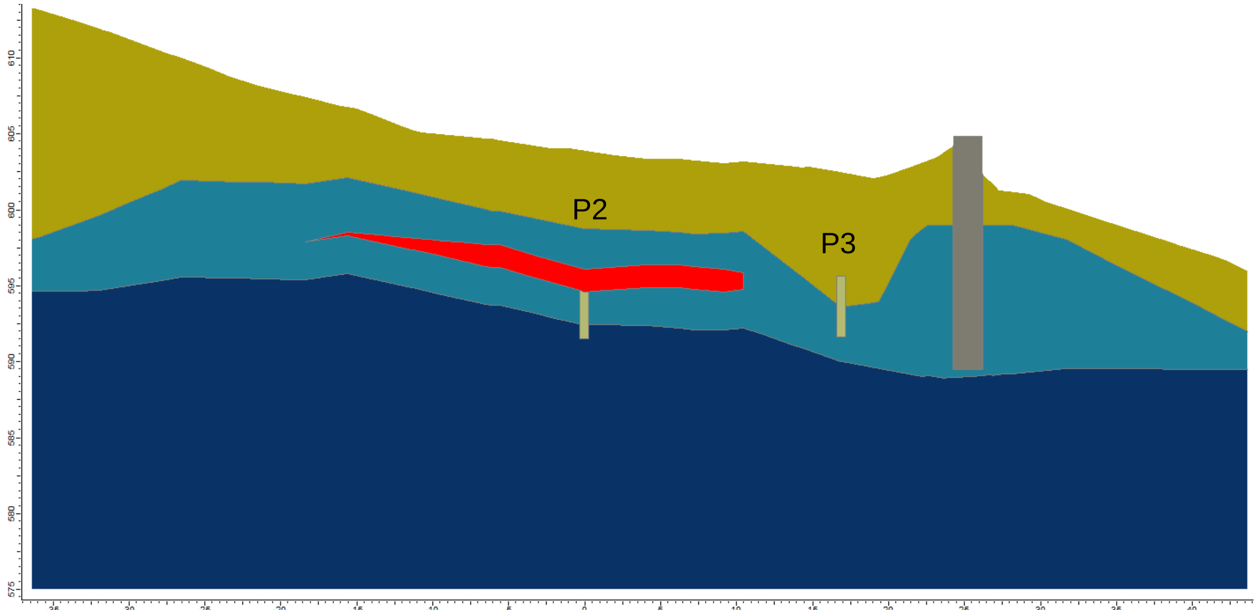

Figure 28. Cross-section from piezometer 2 to piezometer 3.

6.2.3 Finite Element Mesh

The finite element mesh of the model was generated using the built-in meshing function. The finite elements consisted of 4-noded tetrahedrons. A graded mesh was employed, where the element density is based upon the complexity of the geometry. More complex geometries have a higher density of elements, with the mesh grading away to lower density in regions of simpler geometry. The minimum and maximum element sizes were automatically chosen by the software based on the geometric complexity. An oblique view of the model mesh is seen in Figure 29, while a cross-section of the mesh is presented in Figure 30.

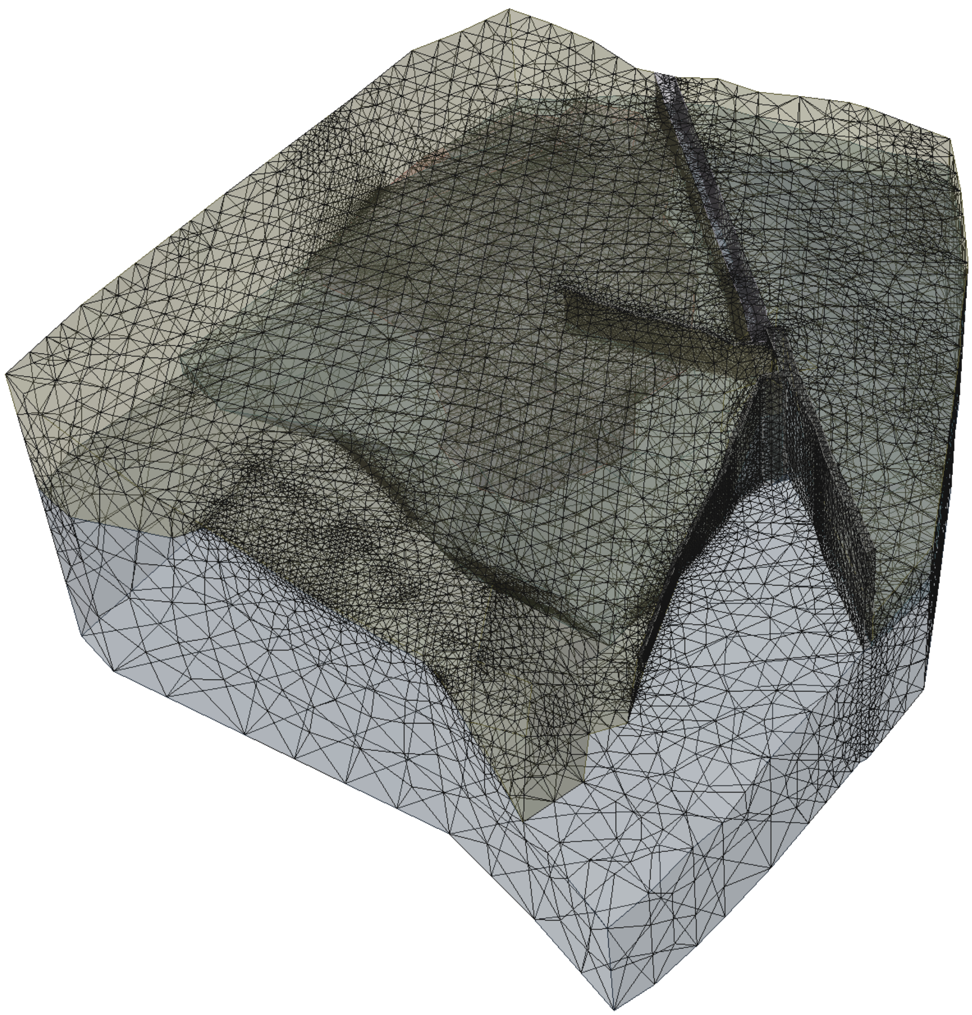

Figure 29. Oblique view of seepage model finite element mesh.

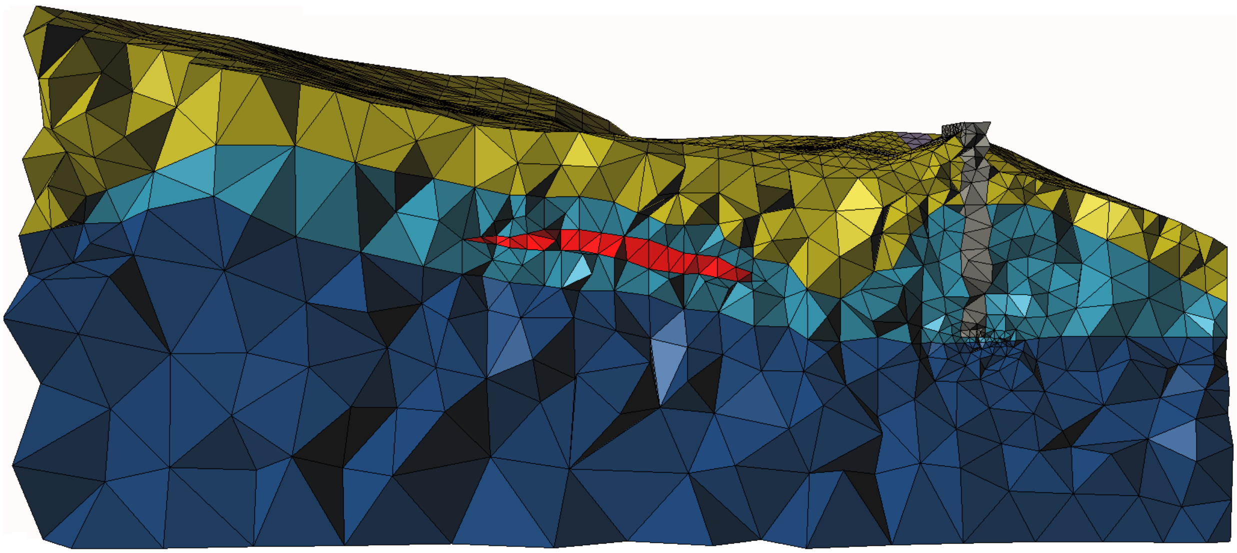

Figure 30. Cross-section of the finite element mesh between piezometer 2 and 3.

RS3 has the functionality to assess the quality of the created finite element mesh. This is an important step in the model creation, as elements with a large aspect ratio can lead to inaccurate results or even, in some cases, non-convergence. Mesh quality is assessed via a shape quality metric; the quality of the mesh is proportional to the ratio of the element volume to the product of the length of the longest face and surface area of the element. The metric can range from 0 to 1, where a value of 1 means the four triangles of the tetrahedron are equilateral. For the seepage model, 99% of tetrahedrons have a mesh quality metric greater than 0.3 and 94% have a mesh quality greater than 0.5. This was considered to be an overall high-quality mesh.

6.3 Material Properties

No field testing of soil conductivity, such as a falling head test within the piezometers, has been completed and recorded for the right abutment piezometers. Therefore, the hydraulic conductivities of the right abutment materials were estimated based on typical published values for these materials (Sherard et al., 1984). Typically, these estimates would be validated by an empirical relationship such as the Kozeny–Carman equation (Chapuis, 2004; 2012), which is suitable for granular soils and non-plastic silt, as found in the right abutment. This equation intrinsically accounts for water at 20°C. For field conditions where the groundwater temperature can be lower, the hydraulic conductivity will be roughly two times (2x) lower due to increased water viscosity. This was taken into account by the sensitivity analysis completed in section 6.6.2.

Empirical relationships for permeability are generally based on material porosity, a function of void ratio and grain size. Typically, the D10 grain size is required, as with the Kozeny–Carman equation. Information regarding the void ratios and gradation of the finer fractions of the abutment materials is unfortunately unknown. Sieve testing in Appendix A shows that the D_{10} of all tested soils is less than the #200 sieve size, and no hydrometer testing was completed. The hydraulic conductivity of sand and gravel with silt is highly sensitive to the silt content (Bandini and Sathiskumar, 2009; Chapuis, 2012). Since sand and gravels are less permeable if there is more silt, the actual hydraulic conductivities of the proposed abutment layers could vary considerably from each other and could vary spatially throughout the embankment.

For the cut-off trench material, the hydraulic conductivity in the horizontal direction was assumed to be higher than the vertical hydraulic conductivity to reflect the layered construction nature. Other materials were considered to behave in a linear isotropic fashion. Glacial deposits typically have anisotropic permeabilities, with deposits generally having horizontal permeabilities much greater than their vertical permeabilities (Culshaw et al., 1991). Additionally, contrary to popular opinion, when dynamically compacted, the horizontal permeability of sands will be lower than the vertical permeability (Chapuis, Gill, and Baass, 1989). An assumption prior to modelling was that flow occurred preferentially in the horizontal direction. As such, anisotropic permeability of the materials was considered during the sensitivity analysis. In consideration of the above, initial hydraulic conductivities were selected. These values are consistent with published values (Freeze and Cherry, 1979) and are summarized in Table 4.

Table 4. Initially assumed hydraulic conductivities.

Material	Hydraulic Conductivity (m/s)
Concrete	1×10^{-14}
Bedrock	1×10^{-8}
Fill	1×10^{-3}
Trench	1×10^{-5}
Fluvial	1×10^{-4}
Till	1×10^{-5}
Filter Sand	1×10^{-1}

The above discussion is only applicable for flow within the saturated zone. For flow within the unsaturated zone, RS3 offers various models to describe the permeability as a function of matric suction. Unsaturated models include Brooks and Corey (1964), Fredlund and Xing (1994), Gardner (1956), and van Genutchen (1980). These models all require either a bubbling pressure or an air entry pressure, parameters that are unknown for the soils of the right abutment. Therefore, the default RS3 unsaturated model was chosen using a general soil type. Using this option, the unsaturated permeability decreases by an order of magnitude within the initial range of matric suction values and then remains constant for higher values of suction. Plots of matric suction vs permeability for the right abutment soils are available in Appendix E.

6.4 Boundary Conditions

Five different boundary conditions were employed within the model, with data from the site visit on October 11, 2018, being used as the initial boundary conditions. The reservoir level and the downstream water level were set as total head conditions, corresponding to the reservoir level and the downstream water level. At this date, the reservoir was at an elevation of 601.4 m. The downstream river channel was at an approximate elevation of 591.1 m, based on the generated orthophoto and DSM. The training wall has a substantial joint separation, as seen in Figure 31. Therefore, the downstream total head (TH) condition was applied just behind the training wall at this point.

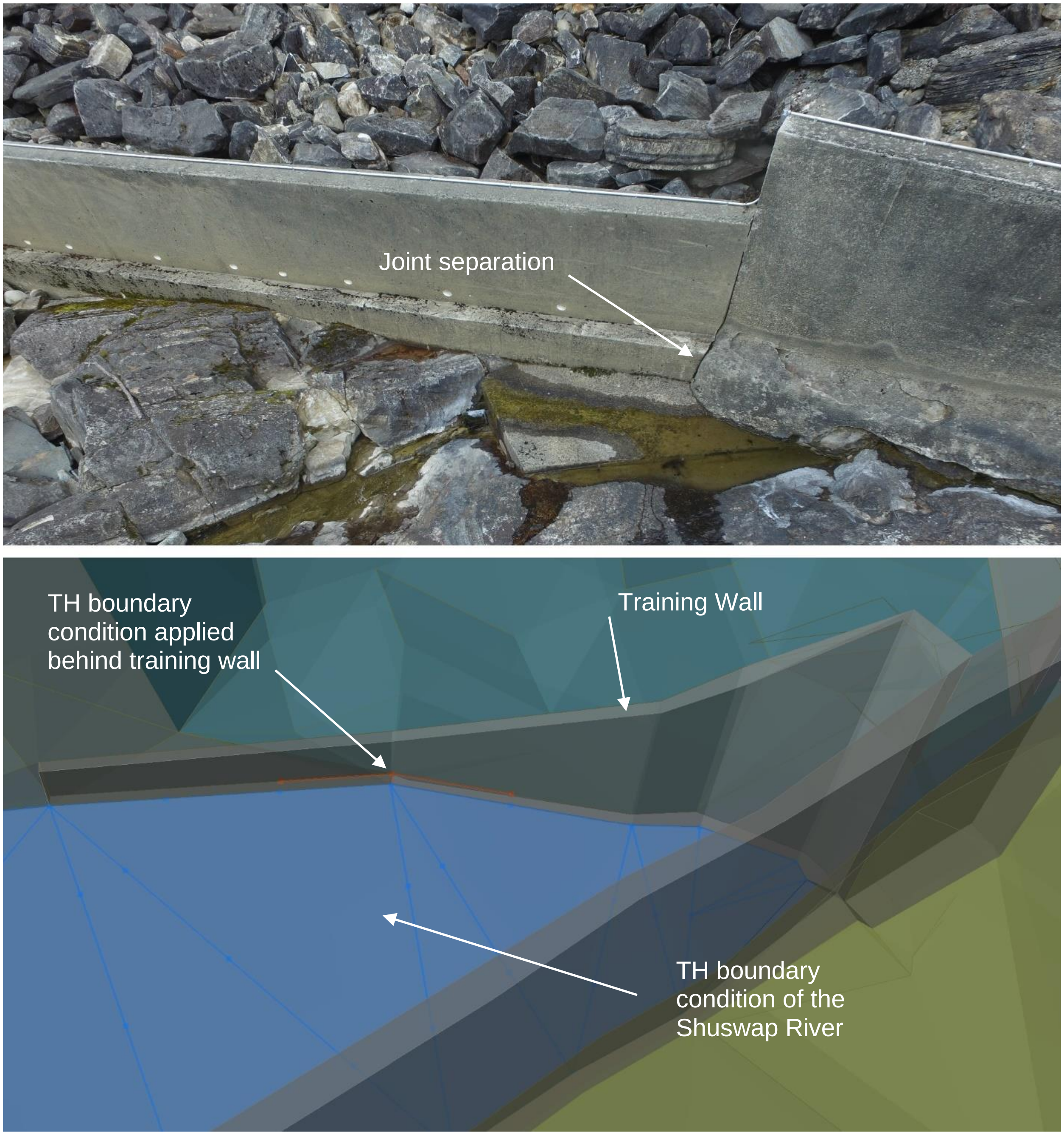

Figure 31. Training wall joint separation and applied boundary condition.

A total head condition was also used for the estimated groundwater level and was uniformly applied along the west side of the model, where the topography continues up the hillside. The groundwater elevation was approximated through trial and error. To match observed conditions, the groundwater elevation must be higher than the reservoir and piezometer levels and lower than the ground surface at the edge of the model. Leaving the soil permeabilities values constant, the groundwater condition was changed until the piezometer readings were within an acceptable starting range of the Oct 28 readings. This was done to generate a baseline to complete a sensitivity analysis of the material properties and boundary conditions.

The remaining ground surfaces of the model were set as seepage face boundary conditions, allowing for either 0 pressure head or 0 flow. All other remaining boundaries were set as no-flow boundary conditions. This was deemed appropriate for the bottom of the model because the bedrock permeability is much lower than the surficial deposits, and vertical downward flow through the bedrock out of the model was negligible. A no-flow boundary condition was also appropriate along the eastern boundary where the river is located. The downstream side of the model where the bedrock rises to the ground surface was also treated as a no-flow boundary condition. The upstream section of the model was also treated as a no-flow condition based on the assumption that groundwater flow coming from the valley side follows perpendicular to the topographic contour lines and laterally into the reservoir; thus, no flow occurs across the northern model boundary. Figure 32 and Figure 33 depict the model's boundary conditions.

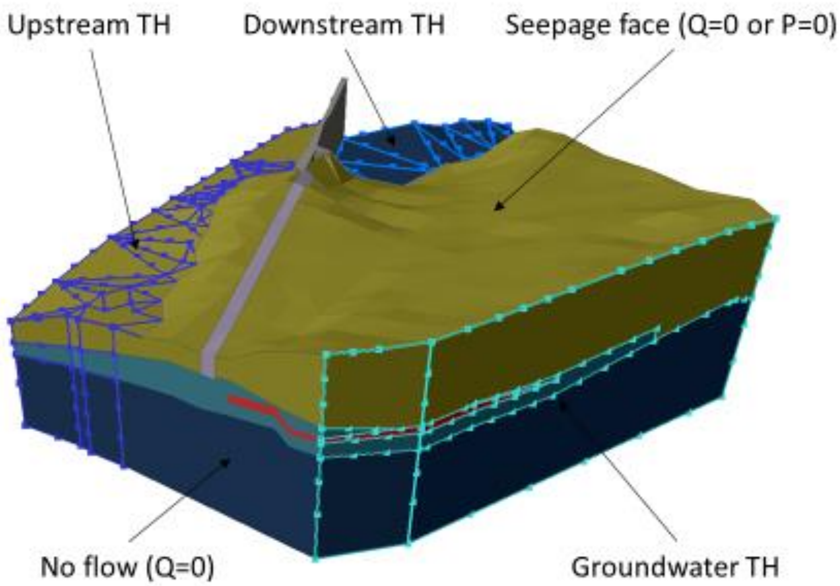

Figure 32. Applied boundary conditions looking south.

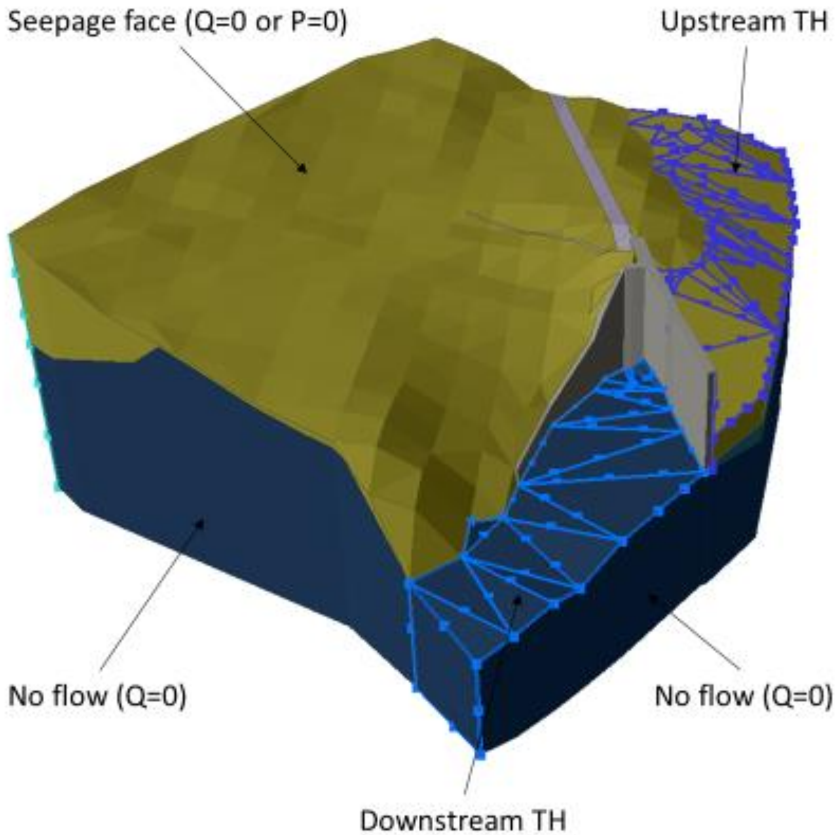

Figure 33. Applied boundary conditions looking north.

6.5 Modelling Stages

The finite element seepage modelling involved the following stages.

1. Calibration simulations to achieve the best estimate for the groundwater table and hydraulic conductivity values.

2. Sensitivity analysis of the permeability values, varying the permeability for one material at a time, leaving the other materials fixed at the calibrated values from stage 1.

3. Sensitivity of the model output to the model boundary conditions.

6.6 Model Results and Discussion

6.6.1 Initial Modelling Stage

Modelling was conducted using the initial permeability estimates. Via a trial-and-error approach, a groundwater level of 604.5 m for the western boundary of the model was found to provide a satisfactory fit to the field data. The final modelled piezometric levels were within 0.9 m of the observed levels. Using the estimated groundwater level, hydraulic conductivities were varied over two orders of magnitude to replicate the observed piezometric levels and create a baseline model for use in the other stages of modelling. The final hydraulic conductivities in Table 5 were determined to fit measured piezometric levels well, with the model results shown in Table 6. Modelling outputs are shown in Appendix E.

Table 5. Initial and calibrated hydraulic conductivities.

Material	Initial Hydraulic Conductivity (m/s)	Final Hydraulic Conductivity (m/s)
Concrete	1×10^{-14}	1×10^{-14}
Bedrock	1×10^{-8}	1×10^{-8}
Fill	1×10^{-3}	3.0×10^{-4}
Trench	1×10^{-5}	4.0×10^{-5}
Fluvial	1×10^{-4}	9.0×10^{-4}
Till	1×10^{-5}	1.2×10^{-5}
Filter Sand	1×10^{-1}	1×10^{-1}

Table 6. Calibration results.

Piezometer	Measured Total Head (m)	Modelled Total Head (m)	Difference (m)
P1	601.85	601.88	+0.03
P2	600.76	600.75	-0.01
P3	598.33	598.33	0.00

6.6.2 Hydraulic Conductivity Sensitivity

The sensitivity of the seepage model results to the assigned hydraulic conductivities was assessed by varying permeability values one at a time. The boundary conditions for the model were also held constant during this procedure. Permeabilities were varied by half an order of magnitude in either direction, giving a range of 5 times higher and 5 times lower than the final calibrated values in Table 5. Sensitivity testing was not completed for the concrete or bedrock, as these materials are far less permeable than the abutment soils. The results of the sensitivity testing are presented in Figure 34. Graphs and tabular results from the sensitivity analysis are available in Appendix E.

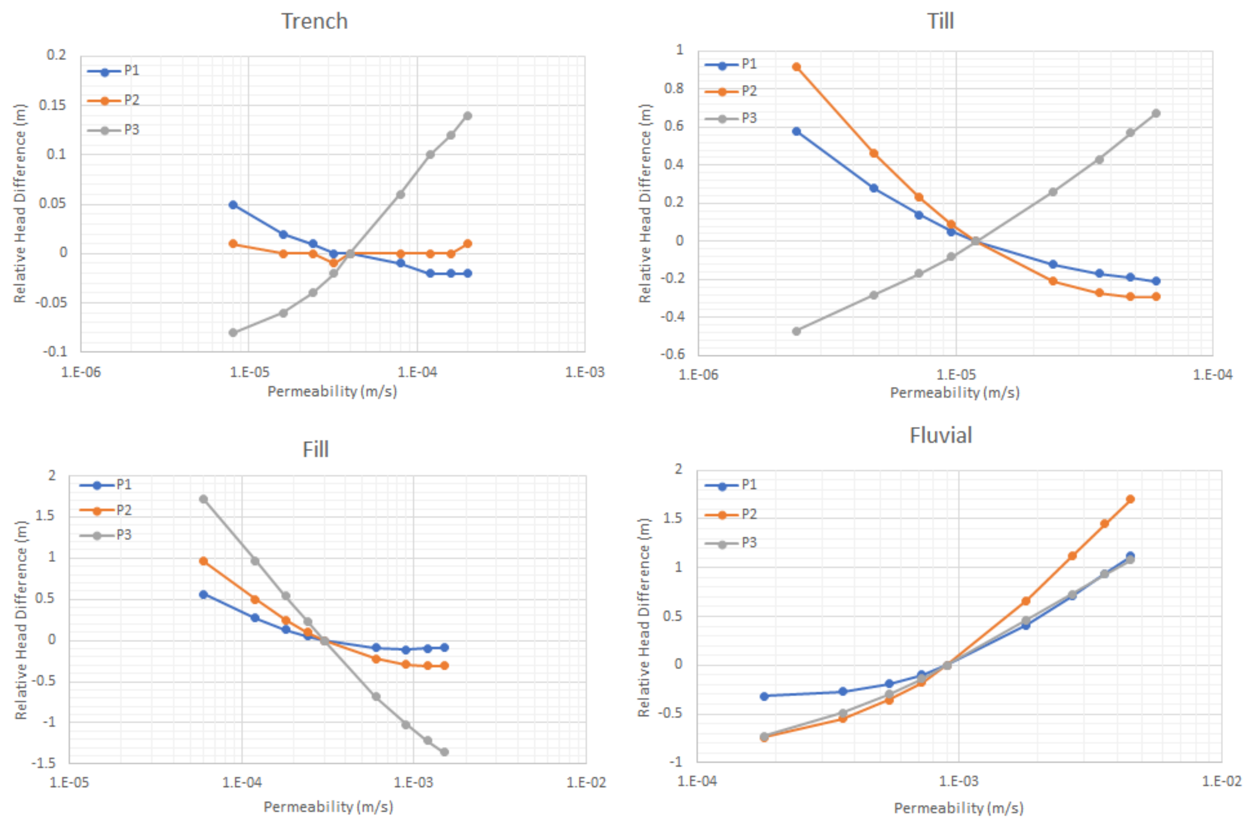

Figure 34. Model sensitivity to changes in material permeability.

Figure 34 demonstrates that the piezometers are relatively insensitive to the cut-off trench's permeability. The insensitivity at P2 is likely due to its longer distance from the reservoir, being double the distance compared to P1 and P3. P1 exhibits a negative correlation; as the permeability increases, the piezometric head drops. P3 exhibits the opposite relationship and is more sensitive to the trench permeability; as the trench permeability increases, the piezometric head rises.

Piezometric levels are only moderately sensitive to changes in the till permeability compared to changes in the fill and fluvial materials. The impact of heads at P3 moves inversely to P1 and P2. An increase in the till permeability causes the groundwater level to drop between the west side of the model and the reservoir or downstream water levels. This results in a lower head at P1 and P2. As the till permeability increases, a lower head drop occurs between the reservoir and P3, and the flow efficiency underneath the cut-off trench increases. These two factors increase the head at P3.

Within the fill, the sensitivity to permeability correlates with the fill thickness at each respective piezometer. P1 has the thinnest fill layer and is the least sensitive, while P3 has the thickest layer and is the most sensitive. As the fill permeability increases, a smaller head loss occurs between the piezometers and the reservoir and downstream boundary conditions. This, in turn, causes the piezometric levels to decrease to satisfy the increased flow efficiency. The converse is true for lower fill permeabilities.

The piezometric heads are sensitive to the permeability within the fluvial layer. However, the individual piezometers all respond in an opposite manner compared to the influence of permeability changes within the fill. Piezometric levels increase with increased fluvial layer permeability and decrease with decreased permeability. This is explained by the lens-shaped geometry of the fluvial layer. The regional groundwater boundary condition at the west side of the model has a more direct and efficient connection to the piezometers, resulting in less head loss between the boundary and the piezometers. The lower permeability till and fill layers that sandwich the fluvial layer facilitate this. The effect can be seen once the permeability of the fluvial layer drops less than that of the fill layer because the rate of change of piezometric level reduces.

Anisotropic Sensitivity

The sensitivity of the seepage model to the anisotropy of hydraulic conductivities was also assessed. This was completed by holding the horizontal permeability (K_h) values constant at the values in Table 5 and varying the vertical permeability (K_v). The boundary conditions for the model were also held constant during this procedure. The K_v/K_h ratio was varied from 1 to 0.1, representing a range of vertical permeabilities up to an order of magnitude lower than the horizontal permeabilities. Analysis of the model sensitivity was completed by varying the ratio for one material at a time. Additionally, the scenario where the anisotropic ratios of all the abutment soils were varied at the same time and rate was analyzed. A summary of results is shown in Figure 35, with the detailed outputs available in Appendix E.

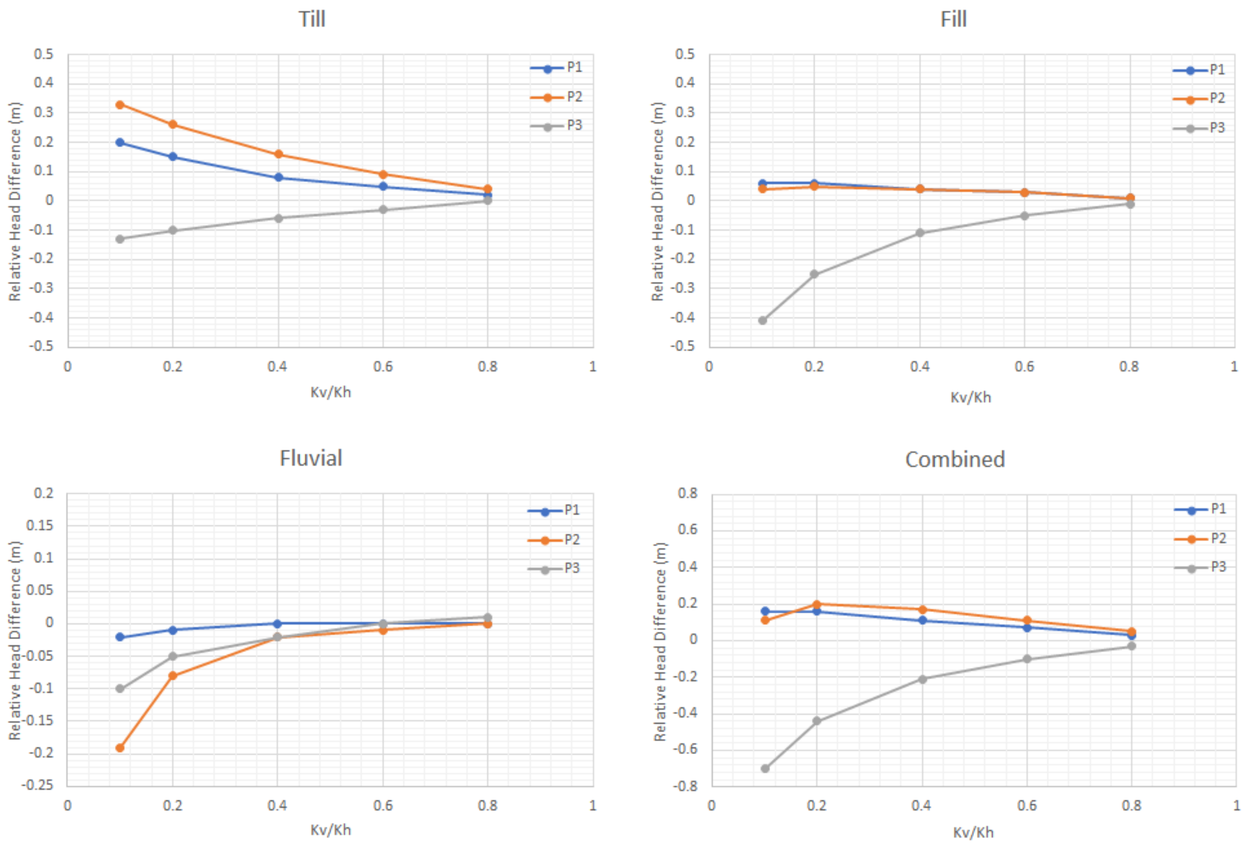

Figure 35. Sensitivity of seepage model to anisotropy of abutment soils.

As expected, P1 and P2 are more sensitive to the anisotropic ratio of the till material than P3. As with variation of the horizontal permeability, the direction of relative change is opposite when comparing P1 and P2 to P3. The sensitivity to the change in vertical permeability is likely due to the slight slope of the till layer and flow within the layer not being completely horizontal in nature. There is less flow in the till layer in the vicinity of P3 when compared to P1 and P2; this is likely why it is less sensitive to changes in the anisotropic ratio.

P1 and P2 are insensitive to the anisotropy of the fill material, while P3 is sensitive to lower anisotropic ratios. This is likely due to the fact that within the model, the majority of flow in the vicinity of P1 and P2 occurs beneath the fill layer. Additionally, the thickness of the fill layer is much larger in the vicinity of P3 compared to P1 and P2. The effect of lower vertical permeabilities is amplified in P3 because of the increased vertical flow in the area required to drive the phreatic surface to meet the downstream boundary condition.

P1 is least sensitive to the anisotropic ratio of the fluvial material, likely due to its location near the northern edge of this material and the presence of largely horizontal flow in this area. P2 is sensitive to low anisotropic ratios, likely due to the fact that the fluvial layer slopes upwards away from the dam axis, and therefore flow within the layer is not completely horizontal, amplifying the effect of the changes to vertical permeability. P3 is relatively sensitive due to its dependence on flow and head loss through the fluvial layer.

When looking at the combined effects of the varied anisotropy, the effects of the fluvial and till layers counteract each other while the effects of the fill layer are compounded. As a general statement, variation of vertical permeabilities has a much lower effect on the model than the variation of horizontal permeabilities. This is consistent with the model geometry and boundary conditions, which generally create horizontal flow across the model.

6.6.3 Boundary Condition Sensitivity

A sensitivity analysis of the seepage model to the boundary conditions was completed by varying the boundary conditions within a reasonable range, one boundary at a time. Other boundaries were fixed to the initially calibrated conditions, as were the permeability values. Tabular results are available in Appendix E. The sensitivity of the model outputs of heads at the piezometer locations to changes in the downstream water elevation, groundwater level, and reservoir level can be seen in Figure 36, Figure 37, and Figure 38, respectively.

Tailwater level

The model is relatively insensitive to the downstream boundary condition, likely due to the dominating effects of the regional groundwater level and the reservoir. P3 is the most sensitive to the downstream water level. P3 is closest to the downstream water and has a tip elevation 11 m away horizontally and 0.9 m lower than the median modelled downstream water elevation. The measurement tip at P3 is also directly connected to the fill layer, which has a higher permeability than the till.

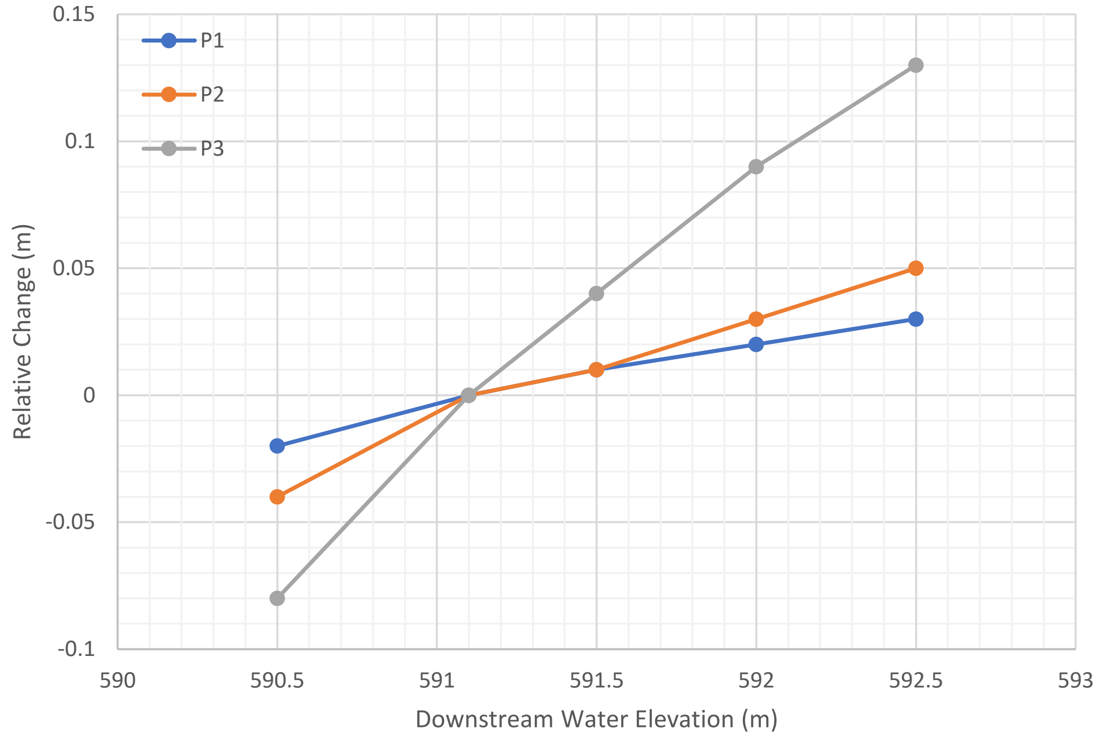

Figure 36. Sensitivity of seepage model to downstream water elevation.

Groundwater level

The predicted piezometric heads react in a linear fashion to changes in the groundwater water level. P1 and P2 react in an almost identical manner, whereas P3 is less sensitive, particularly to lower groundwater levels. This is assumed to be related to how close each piezometer is to the groundwater boundary condition. P3 is farthest from the groundwater boundary.

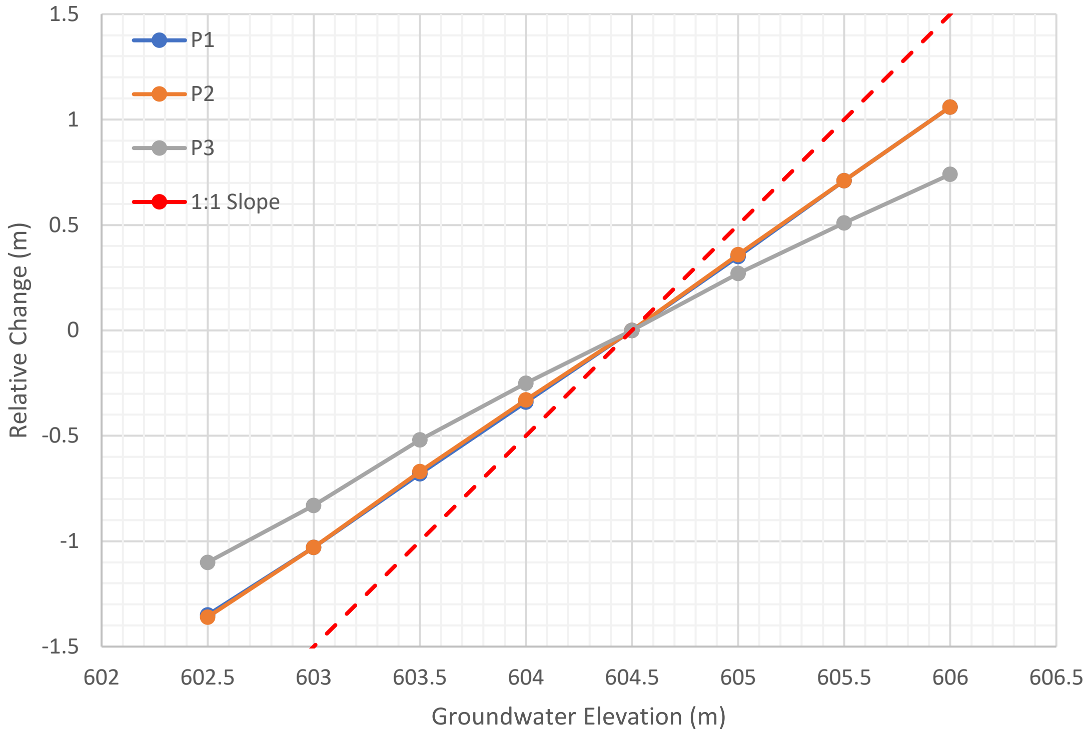

Figure 37. Sensitivity of seepage model to groundwater level.

Reservoir level

Modelling the reservoir at different elevations produced changes in piezometer levels similar to those seen during the seasonal operation of the reservoir. At lower reservoir levels, P1 and P2 move in unison, with little change to piezometric levels occurring when the reservoir is below 599 m. Above a reservoir level of 599 m, P1 and P2 are more sensitive to changes in the reservoir level, with the sensitivity increasing as the reservoir level increases. P3 reacts to changes in the reservoir in a similar fashion, although relative to P1 and P2 it is more sensitive to the reservoir level. This relative sensitivity occurs both above and below a reservoir level of 599 m which is about the elevation of the top of the till layer in the vicinity of the reservoir shoreline.

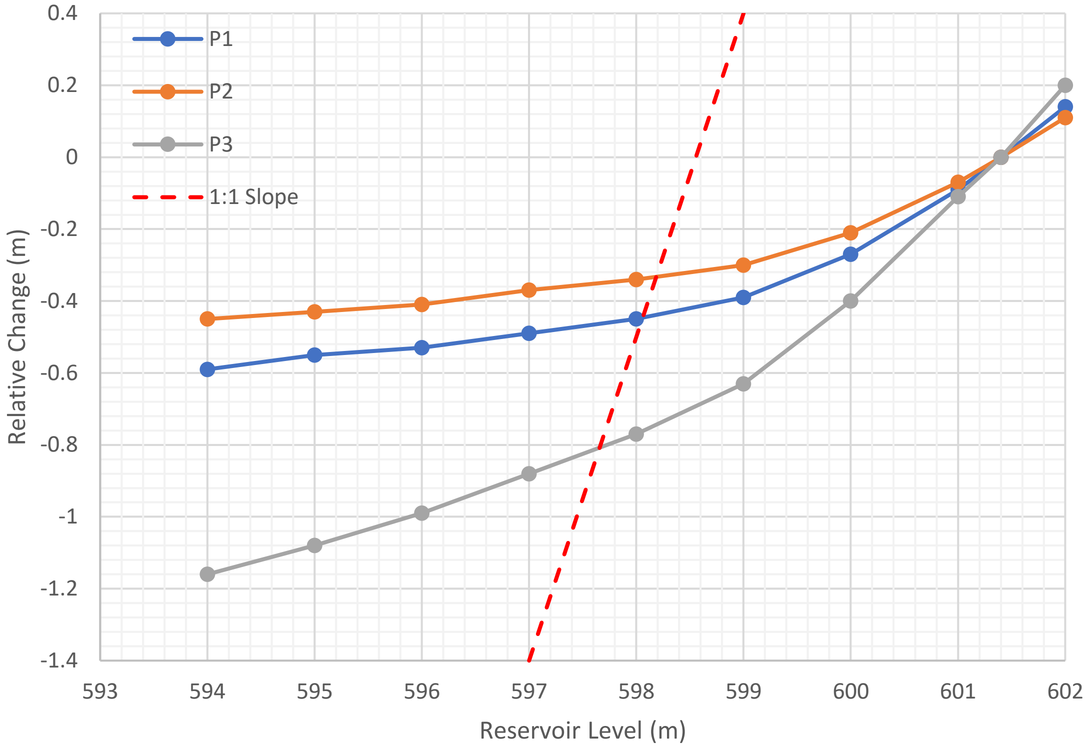

Figure 38. Sensitivity of seepage model to reservoir level.

Further investigation of the sensitivity to the reservoir reveals an interaction between the reservoir level and the groundwater level boundary conditions. As the reservoir level is a known input (boundary condition) for the model with a high level of confidence, and the downstream boundary condition of the model was found to have little impact on piezometer readings, any difference between measured and modelled piezometric head must be accounted for by the groundwater level at the west boundary. Table 7 shows the range of head values measured at the piezometers and head range predicted by the seepage modelling using the operating range of Sugar Lake dam's reservoir level (594.6 – 601.9 m). Based on the sensitivity analysis of the groundwater boundary, the groundwater level at the west side of the seepage model is restricted to ranges from approximately 603.5 to 605.0 m. These results are contingent on the assumed permeabilities and geometry of the right abutment area.

Table 7. Range of modelling results for operating range of the reservoir.

Piezometer	Measured Range	Modelled Range	Unaccounted Difference (m)
P1	1.31	0.69	0.62
P2	1.15	0.53	0.62
P3	2.08	1.30	0.78

The findings from the sensitivity analysis of boundary conditions are consistent with the correlation and cross-correlation analysis presented in Appendix D, demonstrating that the groundwater of the region of the right abutment drives the elevated piezometric levels. This is most prominently seen at P1 and P2. P3 has the most efficient hydraulic connection to the reservoir, as demonstrated by the statistical analysis in Appendix D and the seepage modelling presented above. During periods of low reservoir levels, piezometric levels remain elevated and fluctuate in response to the groundwater inflow from the adjacent mountainside. Once the reservoir level is high enough, it begins to exert greater influence on the fluctuations of the piezometric level. The transition point appears to occur at a reservoir elevation of approximately 599 m.

7 Conclusion

Relationships between piezometer measurements, reservoir levels, climate data, and time of year were investigated using statistical analysis and finite element modelling. Cross-correlation analysis revealed that the reservoir levels and the water levels in the piezometers are significantly correlated when the reservoir is high. The cross-correlation analysis also revealed that the reservoir level is generally not significantly correlated with the piezometer levels when the reservoir levels are less than approximately 597.5 m. This is relatively consistent with the results from the sensitivity analysis of the 3D seepage model; at reservoir elevations below 599 m, the piezometers are less sensitive to the reservoir level change than when the reservoir is above 599 m.

Review and interpretation of the construction history and borehole logging form the basis of the 3D finite element model construction. Based on all available information, 599 m is the approximate interface between the top of the till material and the bottom of the fill material. It was found that when the reservoir is above this elevation, the hydraulic connection between the piezometers and the reservoir is more efficient due to the higher permeability of the fill material. When the reservoir drops below this elevation, the lower permeability till material reduces the influence of the reservoir on the piezometers. The reservoir generally operates above a 599 m level, having a median elevation of 600.0 m. This explains why a visual interpretation of the piezometer and reservoir level graph shows a correlation between the two parameters.

The piezometers levels are often above the reservoir level because they are driven by the regional groundwater level, which is always higher than the reservoir level. Based on the sensitivity analysis of the boundary conditions, the groundwater level at the location of the groundwater boundary condition is likely restricted to a total head range of 603.5 to 605.0 m. This locates the phreatic surface in this area within the fill layer, approximately 5 m below the ground surface. This range was determined by comparing the modelled and measured piezometer levels at the high and low operating levels of the reservoir. As the reservoir elevation is accurately known, and the model is insensitive to the downstream boundary condition, the unaccounted elevation differences between the measured and modelled piezometer levels must come from variations in the regional groundwater level. The sensitivity analysis of the western groundwater boundary condition (total head) indicates that a range of 603.5 to 605.0 m best matches the observed piezometer levels.

The dominating influence of the groundwater level on P1 and P2 is facilitated by the presence of a lens of material with a relatively high permeability sandwiched between lower permeability till layers that join together near P3. The influence of this lens was validated by the permeability sensitivity analysis and the statistical analysis. It can be deduced from the cross-correlation analysis that the lens of higher permeability material is not connected to the reservoir due to the lack of significant correlation at reservoir levels around 597.5 m. The lens is located in the 596 to 598 m range, and if the lens extended to the reservoir, a high correlation between the reservoir and piezometer levels would occur. The low correlation at a reservoir level of 597.5 m level validates the adopted lens geometry in the seepage model.

In addition to being sensitive to the boundary conditions, the seepage model is also sensitive to the permeabilities of the materials and their anisotropy. The seepage model was most sensitive to increases in the permeability of the fluvial layer and decreases in the fill permeability. The model was insensitive to the permeability of the cut-off trench material. This is likely due to the small width (3 m) of the trench and its permeability being higher than till. The piezometer levels were found to be somewhat sensitive to the permeability anisotropy within the material surrounding each piezometer screen. The general lack of sensitivity to anisotropic permeability ratios was due to the layered nature of the different soil types and the boundary conditions that drive the seepage flow in a predominantly horizontal direction through the dam abutment.

There are limitations to the analyses presented in this thesis. Assumptions were required about the stratigraphy and abutment geology. The geometry of the seepage model and the extents of the soil and bedrock locations are subject to interpretation. Uncertainty also exists in the interpretation of the borehole logging. Material testing included no hydrometer testing, and sieve samples were taken at the interfaces of recorded soil layers. This, in addition to the general errors common to field logging notes, leaves room for error in the actual classification of soils in the abutment. Therefore, there is uncertainty in the hydraulic conductivities within the model. The measured piezometer/reservoir levels combinations were used to constrain likely permeabilities for different materials in the dam abutment.

However, even with the limitations mentioned above, recommendations to complement the Sugar Lake Dam safety program can be made. It is recommended that BC Hydro complete falling head tests within each piezometer to validate the hydraulic conductivities used in the seepage analyses. It also recommended that the trend of the data sets is analyzed regularly; a shift in the trend in piezometric data can be an indicator of changes in subsurface conditions.

While there has been a trend of -1.34×10^{-4} m/day identified at P3, it is unlikely to be a current concern due to the lack of evidence of erosion issues.

The hydraulic gradients within the right abutment should be analyzed as a next step. This analysis will identify areas of potential concern for internal erosion. The area surrounding P3 is likely to be the most susceptible area due to its granular nature and the larger amount of vertical flow relative to P1 and P2. Additionally, changes in gradient with time between the piezometers and the reservoir should be monitored. As a simplified monitoring method, the linear distance from the reservoir to the piezometers could be used as the flow path, allowing for essentially real-time monitoring. While not completely accurate, this could prove to be sufficient to detect critical values or outliers from typical values, indicating the possible formation of safety concerns.

References

Acworth, R.I., Rau, G.C., McCallum, M., Anderson, M.S., and Cuthbert, M.O. ‘Understanding connected surface-water/groundwater systems using Fourier analysis of daily and sub-daily head fluctuations’, *Journal of Hydrogeology,* 2015, 23, 143–159.

Aflatooni, M. and Mardaneh, M. (2011) ‘Time series analysis of ground water table fluctuations due to temperature and rainfall change in Shiraz plain’, *International Journal of Water Resources and Environmental Engineering,* 3(9):176–188

Akaike, H. (1974). ‘A new look at the statistical model identification’, *IEEE Transactions on Automatic Control*, 19(6), 716– 723. https://doi.org/10.1109/TAC.1974.1100705.

Andreo, B., Jiménez, P., Durán, J.J., Carrasco, F., Vadillo, I., and Mangin, A. (2005) ‘Climatic and hydrological variations during the last 117–166 years in the south of the Iberian Peninsula, from spectral and correlation analyses and continuous wavelet analyses’, *Journal of Hydrology*, 324, 24–39.

Armstrong, J. E ., Crandell D. R., Easterbrook D. J., and Noble J. B. (1965). Late Pleistocene stratigraphy and chronology in southwestern British Columbia and northwestern Washington: Geological Society of America Bulletin, v. 76, pp. 321-330.

Bailly-Comte, V., Jourde, H., Roesch, A., Pistre, S., and Batiot-Guilhe, C. (2008). ‘Time series analyses for karst/river interactions assessment: case of the Coulazou River (southern France)’, *Journal of Hydrology,* 349(1-2): 98–114.

Bandini, P., & Sathiskumar, S. (2009). ‘Effects of silt content and void ratio on the saturated hydraulic conductivity and compressibility of sand-silt mixtures’. *Journal of Geotechnical and Geoenvironmental Engineering*, 135(12).

Bayazit, M., and Önöz, B. (2007). ‘To prewhiten or not to prewhiten in trend analysis?’, *Hydrological Sciences Journal*, 52(4), 611–624. https://doi.org/10.1623/hysj.52.4.611

BC Hydro. (1984). ‘Preliminary Report on Geological Mapping and Foundation Conditions’, Burnaby: BC Hydro.

BC Hydro. (1985). ‘Sugar Lake Project 1985 Rehabilitation – Memorandum on Construction’, Burnaby: BC Hydro.

BC Hydro. (1996). ‘Sugar Lake Dam Comprehensive Inspection and Review’, Burnaby: BC Hydro.

BC Hydro. (2001). ‘Sugar Lake Dam 1999 Deficiency Investigation’, Burnaby: BC Hydro.

BC Hydro. (2005). ‘Shuswap River Water Use Plan (Shuswap Falls & Sugar Lake Project)’, Burnaby: BC Hydro.

BC Hydro. (2014). ‘Sugar Lake Dam Abutments Seepage Monitoring and Instrumentation Upgrades Construction Report’, Burnaby: BC Hydro.

Birch, J.S. (2006). Using 3DM Analyst mine mapping suite for rock face characterization, in F. Tonon and J. Kottenstette (eds.), Laser and Photogrammetric Methods for Rock Face Characterization, Proc. 41st U.S. Rock Mechanics Symp., Golden.

Bisgaard, S., and Kulahci, M. (2012) Time Series Analysis and Forecasting by Example. Hoboken, New Jersey: John Wiley and Sons.

Box, G., and Jenkins, G. (1976). Time Series Analysis: Forecasting and Control, Revised Edition, San Fransisco: Holden Day.

Bras, R. L., and I. Rodriguez-Iturbe (1985). Random Functions and Hydrology. New York: Dover Publications.

Brooks, R. and Corey, A. (1964). ‘Hydraulic properties of porous media.’ Hydrology Paper No. 3, Colorado State University.

Cai, Z., and Ofterdinger, U. (2016). ‘Analysis of groundwater-level response to rainfall and estimation of annual recharge in fractured hard rock aquifers, NW Ireland’, *Journal of Hydrology*, 535, 71–84. https://doi.org/10.1016/j.jhydrol.2016.01.066

Carr, S. D. (1989). Implications of Early Eocene Ladybird granite in the Thor-Odin--Pinnacles area, southern British Columbia. In *Geological Survey of Canada Paper 89-1E* (pp. 69–77). Ottawa: Ministry of Energy, Mines and Resources Canada.

Carslaw, D.C. (2005) ‘On the changing seasonal cycles and trends of ozone at Mace Head, Ireland.’, *Journal of Atmospheric Chemistry and Physics,* 5(12), 3441–3450

Chen, Z., Grasby, S., and Osadetz, K.G. (2004). ‘Relation between climate variability and groundwater level in the upper carbonate aquifer, south Manitoba, Canada’, *Journal of Hydrology*, 290, 43–62.

Chapuis, R. (2004). ‘Predicting the saturated hydraulic conductivity of sand and gravel using effective diameter and void ratio.’ *Canadian Geotechnical Journal*, 41: 787-795.

Chapuis, R. (2012). ‘Predicting the saturated hydraulic conductivity of soils: a review.’ *Bulletin of Engineering Geology and the Environment*, 71(3): 401-434.

Chapuis, R., Gill, D., and Baass, K. (1989). ‘Laboratory permeability tests on sand: influence of the compaction method on anisotropy’ *Canadian Geotechnical Journal,* 26: 614-622.

Chiaudani, A., Di Curzio, D., Palmucci, W., Pasculli, A., Polemio, M., and Rusi, S. (2017). ‘Statistical and fractal approaches on long time-series to surface-water/groundwater relationship assessment: A central Italy alluvial plain case study’ *Water,* 9(11), 850. https://doi.org/10.3390/w9110850

Choubin, B., Khalighi-Sigaroodi, S., Malekian, A., Ahmad, S., and Attarod, P. (2014) ‘Drought forecasting in a semi-arid watershed using climate signals: a neuro-fuzzy modeling approach’ *Journal of Mountain Science,* 11(6), 1593–1605. doi:10.1007/s11629-014-3020-6

Choubin, B., Malekian, A., and Golshan, M. (2016) ‘Application of several data-driven techniques to predict a standardized precipitation index’, *Atmosfera,* 29(2):121–128. doi:10.20937/ATM.2016.29. 02.02

Cleveland, R., Cleveland, W., McRae, J., and Terpenning, I. (1990) ‘STL: a seasonal-trend decomposition procedure based on loess’, *Journal of Official Statistics,* 6(1), 3–73.

Cleveland, W. (1979) ‘Robust locally weighted regression and smoothing scatterplots’, *Journal of the American Statistical Association* 74, 829–836. doi:10.1080/01621459. 1979.10481038

Cleveland, W. and Devlin, S. (1988) ‘Locally weighted regression: an approach to regression analysis by local fitting’, *Journal of the American Statistical Association,* 83, 596–610. doi:10.1080/01621459.1988.10478639

Cryer, J. and Chan, K. (2008). Time Series Analysis With Applications in R (Second edition). New York: Springer. https://doi.org/10.1016/0377-2217(85)90052-9

Cui, Y., Miller, D., Schiarizza, P., and Diakow, L.J.(2017) ‘British Columbia digital geology'. British Columbia Ministry of Energy, Mines and Petroleum Resources, British Columbia Geological Survey Open File 2017-8, 9p. Data version 2019-12-19.

Culshaw, M., Cripps, J., Bell, F., and Moon, C. (1991) ‘Engineering geology of Quaternary soils: I. Processes and properties’ *Geological Society, London, Engineering Geology Special Publications*, 7: 3-38.

Delbart, C., Valdes, D., Barbecot, F., Tognelli, A., Richon, P., Couchoux, L. (2013) ‘Temporal variability of karst aquifer response time established by the sliding-windows cross-correlation method’ *Journal of Hydrology,*511, 580–588.

Demarchi, D. A. (2011). An introduction to the Ecoregions of British Columbia. Victoria: BC Ministry of Environment

Dickey, D. and Fuller, W (1979). ‘Distribution of the estimates for autoregressive time series with a unit root’, *Journal of American Statistical Association*, 74, 427–431.

Draeyer, B. and C. Strecha. White paper: how accurate are UAV surveying methods? Pix4D, 2014. Available from: https://support.pix4d.com/entries/40219303-How-accurate-are-UAV-surveying-methods

Duvert, C., Jourde, H., Raiber, M., and Cox, M. (2015) ‘Correlation and spectral analyses to assess the response of a shallow aquifer to low and high frequency rainfall fluctuations’, *Journal of Hydrology*, 527(August), 894–907. https://doi.org/10.1016/j.jhydrol.2015.05.054

EBA Engineering Consultants LTD. (1998). Detailed Terrain Stability Mapping, East Sugar Lake, Vernon Forest District, British Columbia. Vancouver: EBA Engineering Consultants LTD.

EBA Engineering Consultants LTD. (1999). Detailed and Reconnaissance Terrain Mapping West Sugar Lake and Gates Creek Areas, B.C. Vancouver: EBA Engineering Consultants LTD.

Esterby, S. (1993) ‘Trend analysis methods for environmental data’, *Environmetrics* 4:459–481. doi:10.1002/env.3170040407

Fazeli, H., Samadzadegan, F., and Dadrasjavan, F. (2016) ‘Evaluating the potential of RTK-UAV for automatic point cloud generation in 3D rapid mapping’, *International Archives of the Photogrammetry, Remote Sensing and Spatial Information Sciences,* 41, 221–226. https://doi.org/10.5194/isprsarchives-XLI-B6-221-2016

Fiorillo, F. and Doglioni, A. (2010) ‘The relation between karst spring discharge and rainfall by cross-correlation analysis (Campania, southern Italy)’, *Journal of Hydrogeology*, 18, 1881

Forlani, G., Asta, E., Diotri, F., Morra, U., Id, R., and Santise, M. (2018) ‘Quality assessment of DSMs produced from UAV flights georeferenced with on-Board RTK positioning’, *Remote Sensing*, 10(2), 311 https://doi.org/10.3390/rs10020311

Fredlund, D.G. and Xing, A. (1994). ‘Equations for the soil-water characteristic curve.’ *Canadian Geotechnical Journal,* 31, 521-532.

Freeze, A., & Cherry, J. (1979). *Groundwater.* Englewood Cliffs, NJ: Prentice-Hall Inc.

Gardner, W. (1956). ‘Mathematics of isothermal water conduction in unsaturated soils.’ Highway Research Board Special Report 40 International Symposium on Physico-Chemical Phenomenon in Soils, Washington D.C. pp. 78-87.

Gárfias-Soliz J, Llanos-Acebo H, Martel R. 2010. Time series and stochastic analyses to study the hydrodynamic characteristics of karstic aquifers. *Hydrological Processes* 24: 300–316. DOI: 10.1002/ hyp.7487.

Grolemund, G. and Wickham, H. (2011) ‘Dates and times made easy with lubridate’, *Journal of Statistical Software*, 40(3), 1-25. URL http://www.jstatsoft.org/v40/i03/.

Gibrilla, A., Anornu, G., and Adomako, D. (2018) ‘Trend analysis and ARIMA modelling of recent groundwater levels in the White Volta River basin of Ghana’ *Groundwater for Sustainable Development*, 6, 150–163. https://doi.org/10.1016/j.gsd.2017.12.006

Gill, L., Naughton, O., Johnston, P, Basu, B., and Ghosh, B. (2013) ‘Characterisation of hydrogeological connections in a lowland karst network using time series analysis of water levels in ephemeral groundwater-fed lakes (turloughs)', *Journal of Hydrology,* 499, 289–302.

Golder Associates Ltd. (2012). *Technical Assessment of the Shuswap River Watershed*. Vancouver: Golder Associates Ltd.

Hamed, K. (2009) 'Enhancing the effectiveness of prewhitening in trend analysis of hydrologic data', *Journal of Hydrology*, 368(1–4), 143–155. https://doi.org/10.1016/j.jhydrol.2009.01.040

Hamed, K. and Rao, A. (1996), 'A modified Mann-Kendall trend test for autocorrelated data', *Journal of Hydrology*, 204, 182–196. https://doi.org/10.1200/jco.2018.36.15_suppl.522

Hameed, S. (1984), 'Fourier analysis of Nile flood levels', *Geophysical Research Letters*, 1(9), 843–845.

HDR Corporation. (2013). *Sugar Lake Dam: 2013 Dam Safety Review.* Toronto: HDR Corporation.

Holland, S. (1964) ' Landforms of British Columbia, a Physiographic Outline', British Columbia Department of Mines and Petroleum. Res. Bull. 48, 138 pp.

Höy, T., Church, B., Legun, A., Glover, K., Gibson, G., Grant, B., Wheeler, J., Dunne, K., Cunningham, J., and Desjardins, P. (1994) *Kootenay Area (82E, F, G, J, K, L, M, N, O; 83C, D),* Ministry of Energy, Mines and Petroleum Resources, British Columbia Geological Survey Open File 1994-8.

Hseih., P., Bredehoeft, J., and Farr, J. (1987) 'Determination of aquifer transmissivity from earth tide analysis', *Water Resources Research,* 23(10), 1824–1832

Hurvich, C. and Tsai, C. (1989) 'Regression and time series model selection in small samples', *Biometrika*, 76(2), 297–307

Hyndman, R. and Athanasopoulos, G. (2018) Forecasting: Principles and Practice, 2nd edition, OTexts: Melbourne, Australia. OTexts.com/fpp2

Hyndman, R., Athanasopoulos, G., Bergmeir, C., Caceres, G., Chhay, L., O'Hara-Wild, M., Petropoulos, F., Razbash, S., Wang, E., and Yasmeen, F. (2020) 'forecast: forecasting functions for time series and linear models', R package version 8.12, <URL: http://pkg.robjhyndman.com/forecast>.

Hyndman, R. and Khandakar, Y. (2008) 'Automatic time series forecasting: the forecast package for R', *Journal of Statistical Software*, 26(3), 1-22. <URL: http://www.jstatsoft.org/article/view/v027i03>.

Hyndman, R. (2020). fpp2: Data for "Forecasting: Principles and Practice" (2nd Edition). R package version 2.4. https://CRAN.R-project.org/package=fpp2

Hyndman, R., Kang, Y., Montero-Manso, P., Talagala, T., Wang, E., Yang, Y., and O'Hara-Wild, M. (2020). tsfeatures: Time Series Feature Extraction. R package version 1.0.2. https://CRAN.R-project.org/package=tsfeatures

Imagawa, C., Takeuchi, J., Kawachi, T., Chono, S., and Ishida, K. (2013) 'Statistical analyses and modeling approaches to hydrodynamic characteristics in alluvial aquifer', *Hydrological Processes*, 26, 4017–4027. https://doi.org/10.1002/hyp.9538

Jahanbakhsh, S.and Babapour Basseri, E. (2003) 'Studying and forecasting of the mean monthly temperature of Tabriz, using ARIMA model', *Journal of Geographical Research,*15 (3), 34–46.

Jenkins, G. and Watts, D.(1968) Spectral Analysis and Its Applications. San Francisco: Holden Day

Jukić, D. and Denić-Jukić, V. (2004) 'A frequency domain approach to groundwater recharge estimation in karst', *Journal of Hydrology*, 289(1–4), 95–110. https://doi.org/10.1016/j.jhydrol.2003.11.005

Jun, I., Berges, M., Garrett, J., and Kelly, C. (2013) "Interpreting the dynamics of embankment dams through a time-series analysis of piezometer data using a non-parametric spectral estimation method', *Computing in Civil Engineering*, 25–32. https://doi.org/10.1017/CBO9781107415324.004

Karamouz, M. and Zahraie, B. (2004) 'Seasonal stream flow forecasting using snow budget and El Nino Southern Oscillation climate signals: application to the salt River Basin in Arizona', *Journal of Hydrological Engineering,*9 (6), 523–533.

Kendall, A. and Hyndman, D.(2007) ‘Examining watershed processes using spectral analysis methods including the scaled-windowed Fourier Transform’ *Subsurface Hydrology: Data Integration for Properties and Processes*, 183–200. https://doi.org/10.1029/171GM14

Kendall, M.G., (1975) Rank correlation methods. London: Griffin.

Kim, J. and Lee, J. (2017) ‘Time series analysis for evaluating hydrological responses of pore-water pressure to rainfall in a slope’, *Hydrological Sciences Journal*, *62*(9), 1412–1421. https://doi.org/10.1080/02626667.2017.1328105

Kim, T., Lee, K., Ho, K., and Chang, H. (2000) ‘Groundwater flow system inferred from hydraulic stresses and heads at an underground LPG storage cavern’, *Journal of Hydrology,* 236, 165–184.

Kwiatkowski, D., Phillips, P., Schmidt, P., and Shin, Y. (1992) ‘Testing the null hypothesis of stationarity against the alternative of a unit root: how sure are we that economic time series have a unit root?’, *Journal of Econometrics*, 54, 159–178.

Lafare, A., Peach, D., and Hughes, A. (2016). ‘Use of seasonal trend decomposition to understand groundwater behaviour in the Permo-Triassic Sandstone aquifer, Eden Valley, UK. *Hydrogeology Journal*, 24(1), 141–158. https://doi.org/10.1007/s10040-015-1309-3

Larocque, M., Mangin, A., Razack, M., and Banton, O. (1998) ‘Contribution of correlation and spectral analyses to the regional study of a large karst aquifer (Charente, France)’ *Journal of Hydrology,* 205(3-4), 217–231. DOI: 10.1016/S0022-1694(97)00155-8.

Lee, J. and Lee, K. (2000) ‘Use of hydrologic time series data for identification of recharge mechanism in a fractured bedrock aquifer system’, *Journal of Hydrology,* 229(3-4), 190–201. DOI: 10.1016/S0022-1694(00)00158-X.

Lee, S., Lee, S., and Hamm, S., (2009) ‘A model for groundwater time series from the well field of riverbank filtration’ *Journal of Korea Water Resour Association,* 42, 673–680

Ljung, G. and Box, G. (1978) ‘On a measure of lack of fit in time series models’, *Biometrika*, 65, 297-303.

Lomb, N. (1976) ‘Least-squares frequency analysis of unequally spaced data’, *Journal of Astrophysics and Space Science,* 39, 447–462.

Lu, W., Zhao, Y., Chu, H., and Yang, L. (2013) ‘The analysis of groundwater levels influenced by dual factors in western Jilin Province by using time series analysis method’, *Journal of Applied Water Science,* 4(3), 251–260

Madawalagama, S., Munasinghe, N., Dampegama, S., and Samarakoon, L. (2015) ‘Low cost aerial mapping with consumer grade drones’, *37th Asian Conference on Remote Sensing*.

Mann, H. (1945) ‘Nonparametric tests against trend’, Econometrica, 13, 245–259. doi:10.2307/1907187

Martínez-Espejo Zaragoza, I., Caroti, G., Piemonte, A., Riedel, B., Tengen, D., and Niemeier, W. (2017) ‘Structure from motion (SfM) processing of UAV images and combination with terrestrial laser scanning, applied for a 3D-documentation in a hazardous situation’ *Geomatics, Natural Hazards and Risk*, *8*(2), 1492–1504. https://doi.org/10.1080/19475705.2017.1345796

Matalas, N. and Sankarasubramanian, A. (2003) ‘Effect of persistence on trend detection via regression’, *Journal of Water Resources Research*, 39(12). https://doi.org/10.1029/2003WR002292

Merritt, L. (2004) ‘Estimating hydraulic properties of the Floridan Aquifer System by analysis of earth-tide, ocean-tide, and barometric effects, Collier and Hendry counties, Florida’, *US Geological Survey Water Resource Investigation Report 03–4267*

Metcalfe, A., Cowpertwait, P. (2009) Introductory time series with R. New York: Springer

Mills, S. and McLeod, P. (2013) ‘Global seamline networks for orthomosaic generation via local search’ *ISPRS Journal of Photogrammetry and Remote Sensing*, *75*, 101–111. https://doi.org/10.1016/j.isprsjprs.2012.11.003

Narayanan, P., Basistha, A., Sarkar, S., and Kamna, S. (2013) ‘Trend analysis and ARIMA modelling of pre-monsoon rainfall data for western India’, *Comptes Rendus Geoscience,* 345(1), 22–27

Nury, A., Hasan, K., and Alam, M. (2017) ‘Comparative study of wavelet-ARIMA and wavelet-ANN models for temperature time series data in northeastern Bangladesh, *Journal of King Saud University - Science*, 29(1), 47–61.https://doi.org/10.1016/j.jksus.2015.12.002

Okulitch, A. V. (1989). Revised stratigraphy and structure in the Thompson-Shuswap-Okanagan map area, southern British Columbia. In *Geological Survey of Canada Paper 89-1E* (pp. 51–60). Ottawa: Ministry of Energy, Mines and Resources Canada.

Padilla, A. and Pulido-Bosch, A. (1995) ‘Study of hydrographs of karstic aquifers by means of correlation and cross-spectral analysis’ *Journal of Hydrology*, 168, 73–89.

Panagopoulos, G. and Lambrakis, N. (2006) ‘The contribution of time series analysis to the study of the hydrodynamic characteristics of the karst systems: Application on two typical karst aquifers of Greece (Trifilia, Almyros Crete)’, *Journal of Hydrology,* 329, 368–376.

Panda, D., Mishra, A., and Kumar, A. (2012) ‘Quantification of trends in groundwater levels of Gujarat in western India’, *Hydrological Sciences Journal*, 57(7), 1325–1336. doi:10.1080/02626667.2012.705845

Percival, D. and Walden, A. (1993) Spectral Analysis for Physical Applications: Multitaper and Conventional Univariate Techniques. Cambridge: Cambridge University Press

Pohlert, T. (2020). trend: Non-Parametric Trend Tests and Change-Point Detection. R package version 1.1.3. https://CRAN.R-project.org/package=trend

Press, W., and Rybicki, G. (1989) ‘Fast algorithm for spectral analysis of unevenly sampled data’, *Journal of Astrophysics,* 338, 277–280.

Press W., Teukolsky, S., Vetterling, S., and Flannery, B. (1994) Numerical recipes in C: the art of scientific computing 2nd edition. Cambridge: Cambridge University Press

R Core Team (2020). R: A language and environment for statistical computing. R Foundation for Statistical Computing, Vienna, Austria. URL https://www.R-project.org/.

Ribeiro,L., Kretschmer, N., Nascimento, J., Buxo, A., Rötting, T., Soto, G., Señoret, M., Oyarzún, J., Maturana, H., and Oyarzún, R. (2015) ‘Evaluating piezometric trends using the Mann-Kendall test on the alluvial aquifers of the Elqui River basin, Chile’, *Hydrological Sciences Journal*, 60(10), 1840-1852, DOI: 10.1080/02626667.2014.945936

Rivard, C. (2009) ‘Groundwater recharge trends in Canada’, Canadian Journal of Earth Science, 46, 841–854.

Ross, S. (2017). Discrete Random Variables. In Introductory Statistics. https://doi.org/10.1016/b978-0-12-804317-2.00005-9

Ruf, T. (1999) ‘The Lomb-Scargle Periodogram in biological rhythm research: analysis of incomplete and unequally spaced time-series’, *Biological Rhythm Research,*30, 178-201

Patakamuri, S. and O'Brien, N. (2020). modifiedmk: Modified Versions of Mann Kendall and Spearman's Rho Trend Tests. R package version 1.5.0. https://CRAN.R-project.org/package=modifiedmk

Sanz-Ablanedo, E., Chandler, J. H., Rodríguez-Pérez, J. R., and Ordóñez, C. (2018) ‘Accuracy of unmanned aerial vehicle (UAV) and SfM photogrammetry survey as a function of the number and location of ground control points used’ *Remote Sensing*, *10*(10). https://doi.org/10.3390/rs10101606

Scargle, J. (1982) ‘Statistical aspects of spectral analysis of unevenly spaced data’, *Astrophysical Journal*, 263, 835–853. https://doi.org/10.1086/160554

Scheliga, B., Tetzlaff, D., Nuetzmann, G., and Soulsby, C. (2018) ‘Groundwater dynamics at the hillslope–riparian interface in a year with extreme winter rainfall’, *Journal of Hydrology*, 564, 509–528. https://doi.org/10.1016/j.jhydrol.2018.06.082

Schiarizza, P. and Church., N. (1996) *The Geology of the Thompson - Okanagan Mineral Assessment Region*. British Columbia Ministry of Energy, Mines and Petroleum Resources, British Columbia Geological Survey Open File 1996-20.

Schloerke, B., Cook, D., Larmarange, J., Briatte, F., Marbach, M., Thoen, E., Elberg, A., and Crowley, J. (2020). ‘GGally: Extension to 'ggplot2'.’ R package version 2.0.0. https://CRAN.R-project.org/package=GGally

Schwarz, G. (1978) ‘Estimating the dimension of a model’, *The Annals of Statistics*, 6(2), 461–464.

Sen, P.K. (1968), ‘Estimates of the regression coefficient based on Kendall’s tau’, *Journal of the American Statistical Association*, 63, 1379–1389. doi:10.1080/01621459.1968.10480934

Shamsnia, S., Shahidi, N., Liaghat, A., Sarraf, A., and Vahdat, S.F. (2011) ‘Modeling of weather parameters using stochastic methods (ARIMA Model) Case Study: Abadeh Region, Iran’, *International Conference on Environment and Industrial Innovation IPCBEE*, 12, 282–285

Shamsudduha, M. (2011). Groundwater dynamics and arsenic mobilisation in Bangladesh: a national- scale characterisation. University College London

Shamsudduha, M., Chandler, R., Taylor, R., and Ahmed, K. (2009) ‘Recent trends in groundwater levels in a highly seasonal hydrological system: The Ganges-Brahmaputra-Meghna Delta’, *Hydrology and Earth System Sciences*, 13(12), 2373–2385. https://doi.org/10.5194/hess-13-2373-2009

Sherard, J., Dunnigan, L., & Talbot, J. (1984). Basic properties of sand and gravel filters. *Journal of Geotechnical Engineering ASCE*, 110(6): 684-700.

Sigaroodi, S., Chen, Q., Ebrahimi, S., Nazari, A., and Choobin, B. (2014) ‘Long-term precipitation forecast for drought relief using atmospheric circulation factors: a study on the Maharloo Basin in Iran’, *Hydrology and Earth Systems Sciences*, 18(5):1995–2006. doi:10.5194/hess- 18-1995-2014

Smith, G. W. (1969). Surficial Geology of the Shuswap River Drainage, British Columbia. Ohio State University.

Tabari, H., Nikbakht, J., and Shifteh Some’e, B. (2012) ‘Investigation of groundwater level fluctuations in the north of Iran’, *Environmental Earth Sciences*, 66 (1), 231–243. doi:10.1007/s12665-011-1229-z

Tan, S., Shuy, E., Chua, L., and Yee, W. (2007) ‘Studies on groundwater recharge characteristics at a reclaimed land site with an equatorial climate using time-series and spectral analyses’, *Hydrological Processes*, 21, 939–948. https://doi.org/10.1002/hyp

Tannant, D. (2015) ‘Review of photogrammetry-based techniques for characterization and hazard assessment of rock faces’, *International Journal of Geohazards and Environment*, *1*, 76–87. https://doi.org/10.15273/ijge.2015.02.009

Taylor, C.and Alley, W. (2002) Ground-water-level monitoring and the importance of long-term water-level data. US Geological Survey, Reston, UK

Thanh Tam, V., De Smedt, F., Batelaan, O., and Dassargues, A. (2004) ‘Characterization of a cavern conduit system in Vietnam by time series correlation, cross-spectrum and wavelet analyses’, *Journal of Hydrological Sciences*, 49, 879–900.

Theil, H. (1950) “A rank-invariant method of linear and polynomial regression analysis, Part 3’, *Proceedings of Koninklijke Nederlandse Academie van Wetenschappen A*, 53, 1397–1412.

Trapletti, A. and Hornik, K. (2019). ‘tseries: Time Series Analysis and Computational Finance’, R package version 0.10-47.

Turner, D., Lucieer, A., and Watson, C. (2012) ‘An automated technique for generating georectified mosaics’, *International Journal of Remote Sensing*, 4(5), 1392-1410 https://doi.org/10.3390/rs4051392

van Genuchten, M. Th. (1980). ‘A closed form equation for predicting the hydraulic conductivity of unsaturated soils.’ *Soil Science Society of America Journal,* 44, 892-898.

Wickham, H. (2019) ‘Welcome to the tidyverse’, *Journal of Open Source Software*, 4(43), 1686, https://doi.org/10.21105/joss.01686

Wickham, H. (2016) ggplot2: Elegant Graphics for Data Analysis. New York; Springer-Verlag.

Wickham, H. (2007). ‘Reshaping data with the reshape package’, *Journal of Statistical Software*, 21(12), 1-20. URL http://www.jstatsoft.org/v21/i12/.

Wickham, H., François, R., Henry, L., and Müller, K. (2020) ‘dplyr: A Grammar of Data Manipulation. R package version 1.0.2. https://CRAN.R-project.org/package=dplyr

Woodward, W., Gray, H., and Elliott, A. (2011). Applied time series analysis. Boca Raton: CRC Press

Xia, J., Wu, X., Zhan, C., Qiao, Y., Hong, S., Yang, P., and Zou, L. (2019) ‘Evaluating the dynamics of groundwater depletion for an arid land in the Tarim Basin, China’, *Water*, 11(2). https://doi.org/10.3390/w11020186

Wang, X., Smith, K., and Hyndman, R. (2006) ‘Characteristic-based clustering for time series data’, *Data Mining and Knowledge Discovery,* 13(3), 335-364

Yu, J., Ng, M., and Huang, J. (2001) ‘Patterns discovery based on time-series decomposition’, *PAKKD 2001:Knowledge Discovery and Data Mining,* 336- 347.

Yue, S., Pilon, P., Phinney, B., and Cavadias, G. (2002) ‘The influence of autocorrelation on the ability to detect trend in hydrological series’, *Hydrological Processes*, 16(9), 1807–1829. https://doi.org/10.1002/hyp.1095

Yue, S., and Wang, C. (2002) ‘Applicability of prewhitening to eliminate the influence of serial correlation on the Mann-Kendall test’, *Water Resources Research*, 38(6), 4-1-4–7. https://doi.org/10.1029/2001wr000861

Zhang, P., Du, K., Tannant, D., Zhu, H., and Zheng, W. (2018) ‘Automated method for extracting and analysing the rock discontinuities from point clouds based on digital surface model of rock mass’, *Engineering Geology*, *239*, 109–118. https://doi.org/10.1016/j.enggeo.2018.03.020

Zhang Y., and Schilling K. (2004) ‘Temporal scaling of hydraulic head and river base flow and its implication for groundwater recharge’, *Water Resources Research* 40(3), DOI: 10.1029/ 2003WR002094.

Zeileis, A. and Grothendieck, G. (2005). ‘zoo: S3 infrastructure for regular and irregular time series’, *Journal of Statistical Software*, 14(6), 1-27. doi:10.18637/jss.v014.i06

Appendices

APPENDIX A - Material Testing Results

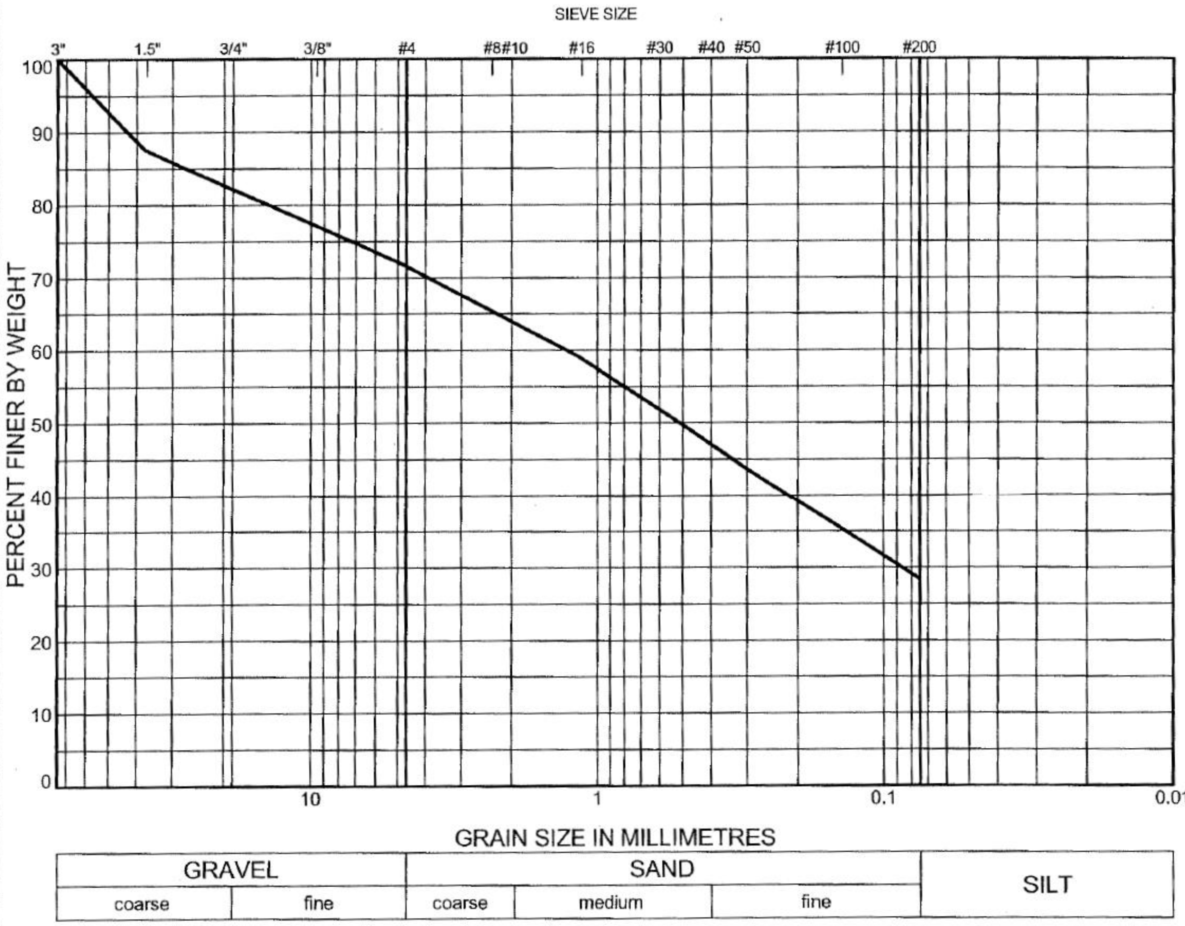

Sample Location: **DH13-1**
Sample: 4
Sample Depth: 3.8 m
Date Sampled: April 2, 2013
Sampled By: MCB
Date Received: April 10, 2013
Date Tested: April 15, 2013
Tested By: KBS
Test Method: ASTM C136 and C117
Specification:

Gravel	**28.2%**
Sand	**43.3%**
Fines	**28.4%**
Moisture Content	%

D10	
D30	**0.086**
D60	**1.28**
Cu	
Cc	

Sieve Size		Percent Passing
inches	mm	
3	75	**100.0**
1.5	37.5	**87.6**
0.75	19	**82.2**
0.375	9.5	**77.1**
#4	4.75	**71.8**
#8	2.36	**65.4**
#16	1.18	**59.3**
#30	0.6	**51.9**
#50	0.3	**43.7**
#100	0.15	**36.1**
#200	0.075	**28.4**

Description: Grey-brown, gravelly, silty SAND (SM)
Comments:

The results are for the sole use of the designated client only. This report constitutes a testing service only and does not represent any interpretation or opinion regarding the specification compliance or material suitability. Engineering interpretation will be provided by Thurber upon request.

THURBER
Thurber Engineering Ltd.
#900 - 1281 West Georgia Street
Vancouver, BC V6E 3J7
Telephone: (604) 684-4384
Fax: (604) 684-5124

GRAIN SIZE DISTRIBUTION

CLIENT: BC Hydro
PROJECT: Sugar Lake Dam Instrumentation
FILE NO.: 15-2-274

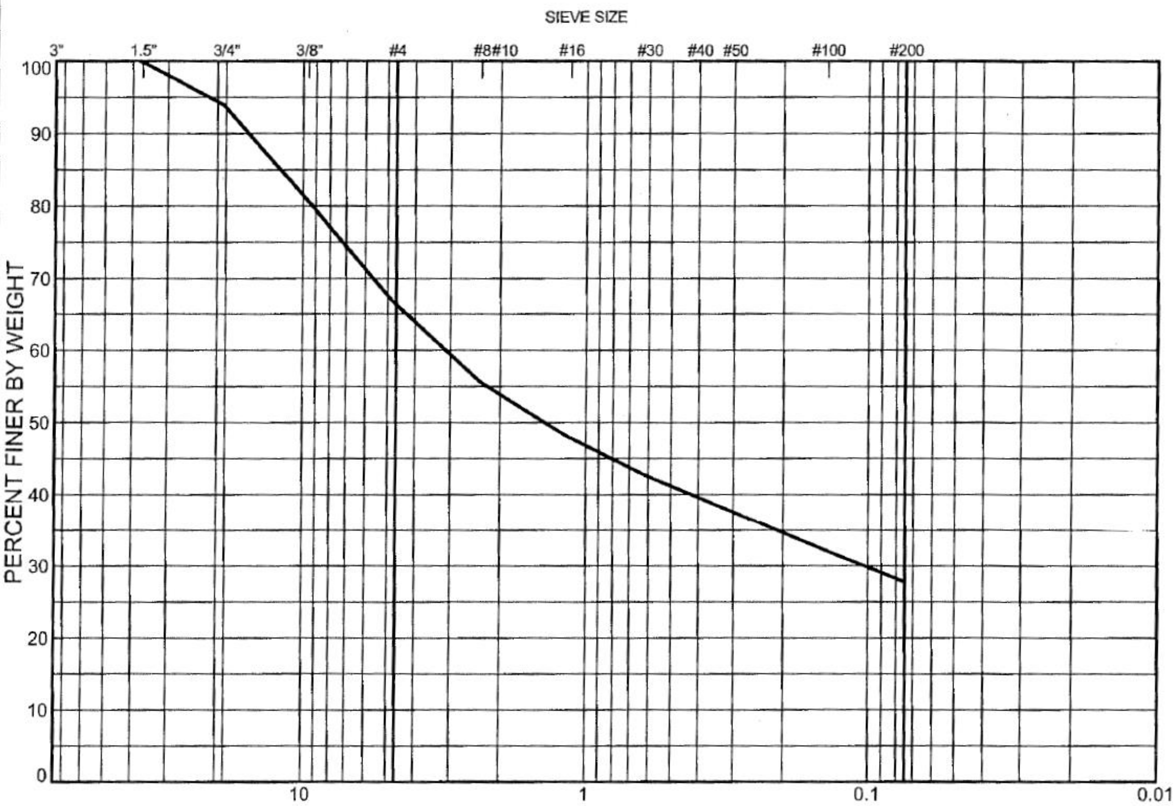

GRAIN SIZE IN MILLIMETRES

GRAVEL		SAND			SILT
coarse	fine	coarse	medium	fine	

Sample Location:	**DH13-1**
Sample:	10
Sample Depth:	8.5 m
Date Sampled:	April 2, 2013
Sampled By:	MCB
Date Received:	April 10, 2013
Date Tested:	April 15, 2013
Tested By:	KBS
Test Method:	ASTM C136 and C117
Specification:	

Gravel	**33.4%**
Sand	**38.9%**
Fines	**27.8%**
Moisture Content	**9.2%**

D10	
D30	**0.103**
D60	**3.104**
Cu	
Cc	

Sieve Size		Percent Passing
inches	mm	
3	75	
1.5	37.5	**100.0**
0.75	19	**93.9**
0.375	9.5	**80.5**
#4	4.75	**66.6**
#8	2.36	**55.7**
#16	1.18	**48.2**
#30	0.6	**42.5**
#50	0.3	**37.6**
#100	0.15	**32.7**
#200	0.075	**27.8**

Description: Grey, silty, gravelly SAND (SM)

Comments:

THURBER
Thurber Engineering Ltd.
#900 - 1281 West Georgia Street
Vancouver, BC V6E 3J7
Telephone: (604) 684-4384
Fax: (604) 684-5124

GRAIN SIZE DISTRIBUTION

CLIENT: BC Hydro
PROJECT: Sugar Lake Dam Instrumentation
FILE NO.: 15-2-274

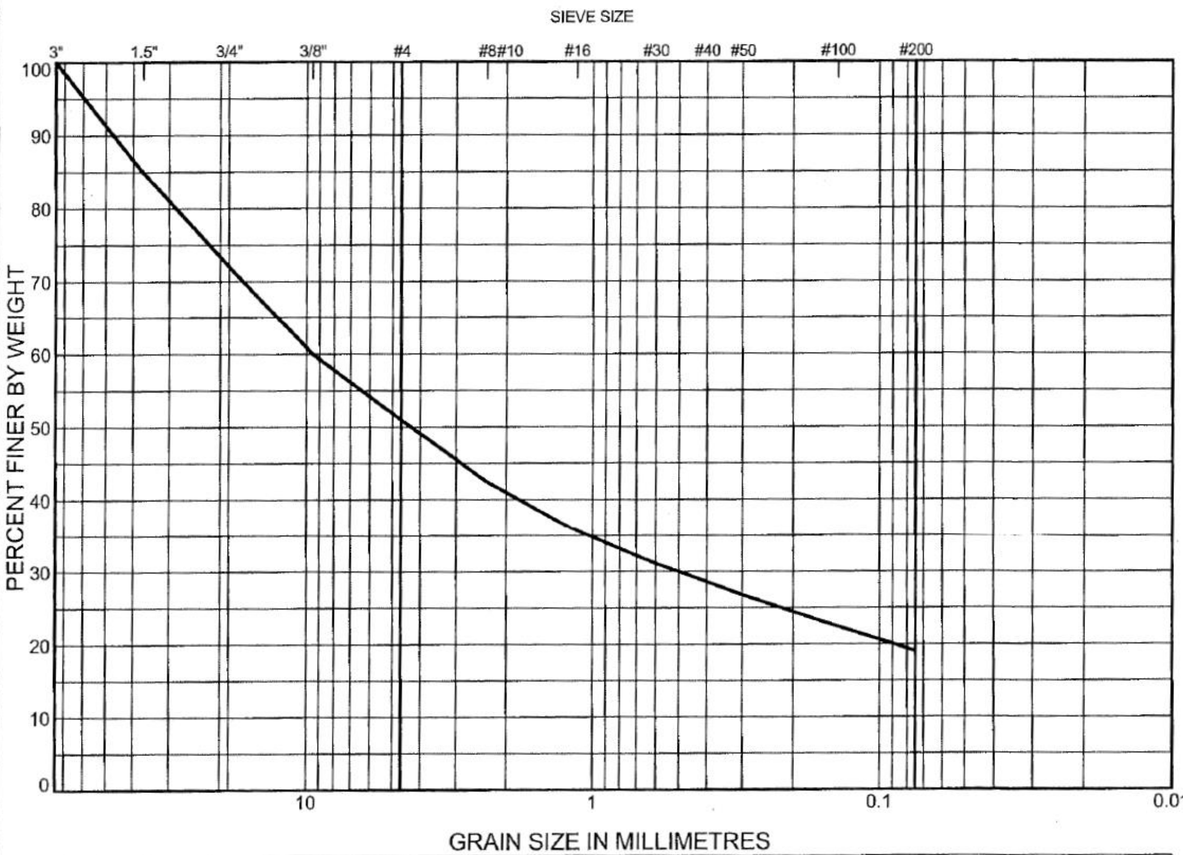

GRAVEL		SAND			SILT
coarse	fine	coarse	medium	fine	

Sample Location: **DH13-2**
Sample: 33
Sample Depth: 6.4 m
Date Sampled: April 3, 2013
Sampled By: MCB
Date Received: April 10, 2013
Date Tested: April 15, 2013
Tested By: KBS
Test Method: ASTM C136 and C117
Specification:

Gravel	**48.8%**
Sand	**32.2%**
Fines	**19.1%**
Moisture Content	%
D10	
D30	**0.5**
D60	**9.491**
Cu	
Cc	

Sieve Size inches	Sieve Size mm	Percent Passing
3	75	**100.0**
1.5	37.5	**85.2**
0.75	19	**72.4**
0.375	9.5	**60.0**
#4	4.75	**51.2**
#8	2.36	**42.6**
#16	1.18	**36.0**
#30	0.6	**31.1**
#50	0.3	**26.8**
#100	0.15	**22.8**
#200	0.075	**19.1**

Description: Grey, sandy GRAVEL, some silt (GM)
Comments:

The results are for the sole use of the designated client only. This report constitutes a testing service only and does not represent any interpretation or opinion regarding the specification compliance or material suitability. Engineering interpretation will be provided by Thurber upon request.

THURBER
Thurber Engineering Ltd.
#900 - 1281 West Georgia Street
Vancouver, BC V6E 3J7
Telephone: (604) 684-4384
Fax: (604) 684-5124

GRAIN SIZE DISTRIBUTION

CLIENT: BC Hydro
PROJECT: Sugar Lake Dam Instrumentation
FILE NO.: 15-2-274

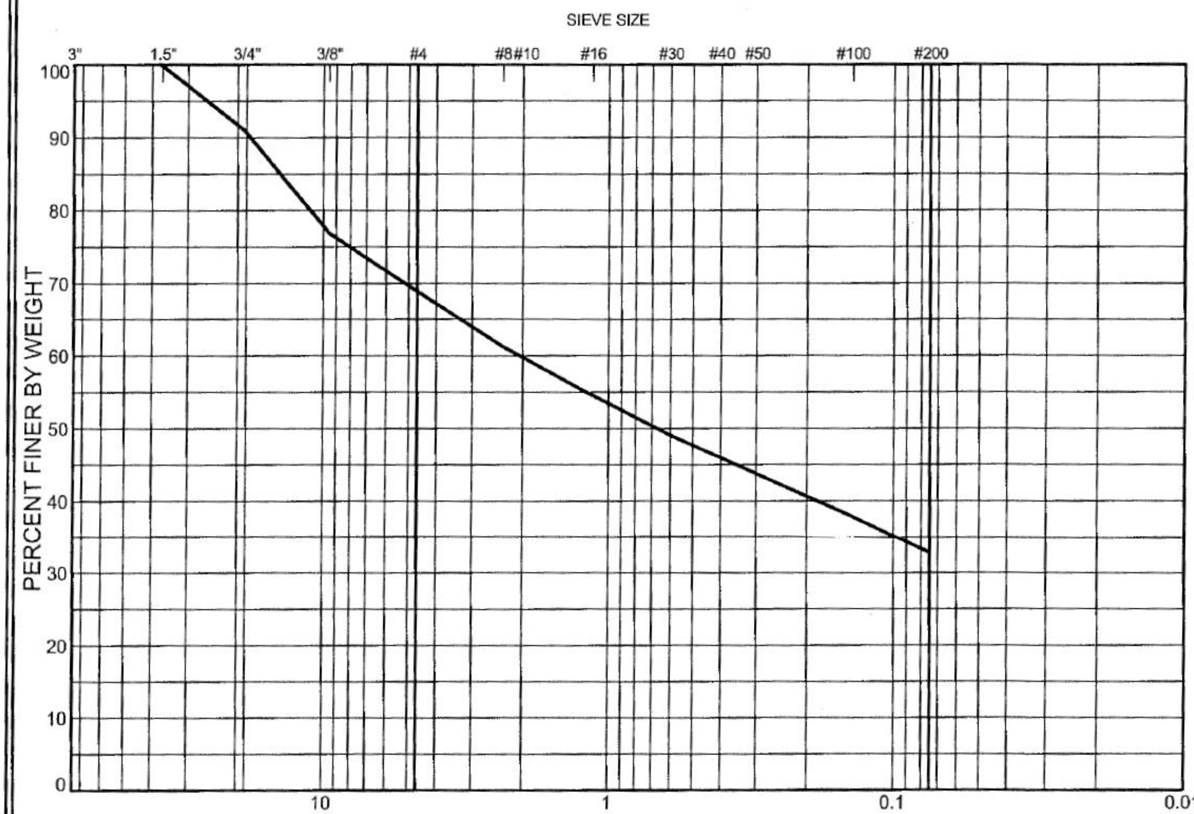

GRAVEL		SAND			SILT
coarse	fine	coarse	medium	fine	

Sample Location: **DH13-2**
Sample: 36
Sample Depth: 8.8 m
Date Sampled: April 3, 2013
Sampled By: MCB
Date Received: April 10, 2013
Date Tested: April 15, 2013
Tested By: KBS
Test Method: ASTM C136 and C117
Specification:

Gravel	**30.9%**
Sand	**36.3%**
Fines	**32.8%**
Moisture Content	**%**
D10	
D30	
D60	**2.042**
Cu	
Cc	

Sieve Size inches	Sieve Size mm	Percent Passing
3	75	
1.5	37.5	**100.0**
0.75	19	**91.0**
0.375	9.5	**76.8**
#4	4.75	**69.1**
#8	2.36	**61.3**
#16	1.18	**54.9**
#30	0.6	**49.1**
#50	0.3	**43.8**
#100	0.15	**38.5**
#200	0.075	**32.8**

Description: Grey, gravelly, silty SAND (SM)
Comments:

THURBER
Thurber Engineering Ltd.
#900 - 1281 West Georgia Street
Vancouver, BC V6E 3J7
Telephone: (604) 684-4384
Fax: (604) 684-5124

GRAIN SIZE DISTRIBUTION

CLIENT: BC Hydro
PROJECT: Sugar Lake Dam Instrumentation
FILE NO.: 15-2-274

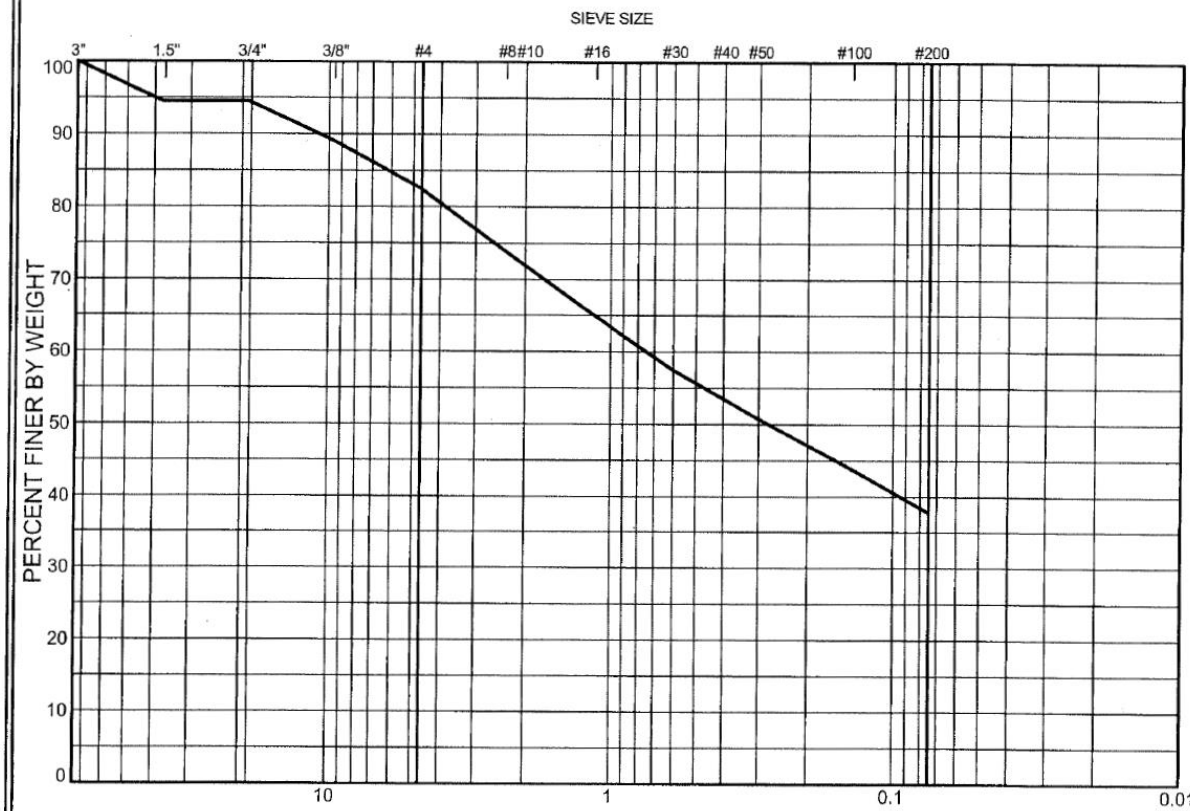

GRAVEL		SAND			SILT
coarse	fine	coarse	medium	fine	

Sample Location:	**DH13-3**
Sample:	21
Sample Depth:	6.4 m
Date Sampled:	April 3, 2013
Sampled By:	MCB
Date Received:	April 10, 2013
Date Tested:	April 15, 2013
Tested By:	KBS
Test Method:	ASTM C136 and C117
Specification:	

Gravel	**17.4%**
Sand	**44.7%**
Fines	**37.9%**
Moisture Content	**13.6%**
D10	
D30	
D60	**0.742**
Cu	
Cc	

Sieve Size		Percent Passing
inches	mm	
3	75	**100.0**
1.5	37.5	**94.5**
0.75	19	**94.5**
0.375	9.5	**89.0**
#4	4.75	**82.6**
#8	2.36	**73.9**
#16	1.18	**65.4**
#30	0.6	**57.5**
#50	0.3	**50.8**
#100	0.15	**44.6**
#200	0.075	**37.9**

Description: Grey-brown, SILT and SAND, some gravel (ML/SM)

Comments:

The results are for the sole use of the designated client only. This report constitutes a testing service only and does not represent any interpretation or opinion regarding the specification compliance or material suitability. Engineering interpretation will be provided by Thurber upon request.

THURBER
Thurber Engineering Ltd.
#900 - 1281 West Georgia Street
Vancouver, BC V6E 3J7
Telephone: (604) 684-4384
Fax: (604) 684-5124

GRAIN SIZE DISTRIBUTION

CLIENT: BC Hydro
PROJECT: Sugar Lake Dam Instrumentation
FILE NO.: 15-2-274

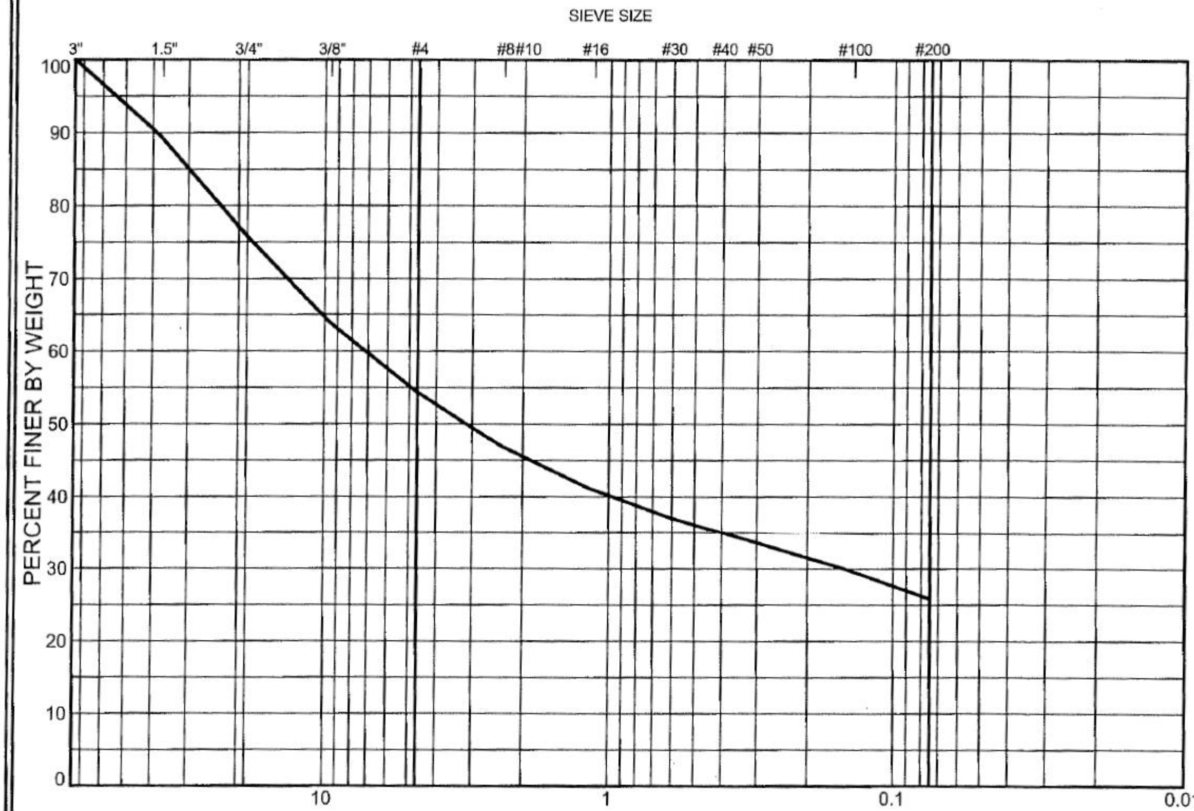

GRAVEL		SAND			SILT
coarse	fine	coarse	medium	fine	

Sample Location: **DH13-3**
Sample: 26
Sample Depth: 9.3 m
Date Sampled: April 3, 2013
Sampled By: MCB
Date Received: April 10, 2013
Date Tested: April 12, 2013
Tested By: JW/KM
Test Method: ASTM C136 and C117
Specification:

Gravel	**45.4%**
Sand	**28.7%**
Fines	**25.9%**
Moisture Content	**7.0%**

D10	
D30	**0.148**
D60	**7.141**
Cu	
Cc	

Sieve Size inches	Sieve Size mm	Percent Passing
3	75	**100.0**
1.5	37.5	**89.5**
0.75	19	**76.1**
0.375	9.5	**63.8**
#4	4.75	**54.6**
#8	2.36	**46.9**
#16	1.18	**41.2**
#30	0.6	**37.1**
#50	0.3	**33.6**
#100	0.15	**30.1**
#200	0.075	**25.9**

Description: Grey, silty, sandy GRAVEL (GM)
Comments:

The results are for the sole use of the designated client only. This report constitutes a testing service only and does not represent any interpretation or opinion regarding the specification compliance or material suitability. Engineering interpretation will be provided by Thurber upon request.

THURBER
Thurber Engineering Ltd.
#900 - 1281 West Georgia Street
Vancouver, BC V6E 3J7
Telephone: (604) 684-4384
Fax: (604) 684-5124

GRAIN SIZE DISTRIBUTION

CLIENT: BC Hydro
PROJECT: Sugar Lake Dam Instrumentation
FILE NO.: 15-2-274

APPENDIX B - Instrumentation Calibration Records

Sugar Lake Vis #1

Calibration Record

200 - 2050 Hartley Ave., Coquitlam, British Columbia, Canada V3K 6W5
Tel: 604.540.1100 • Fax: 604.540.1005 • Toll Free: 1.800.665.5599 (North America only)
e-mail: info@rstinstruments.com • Website: www.rstinstruments.com

STRAIN GAUGE PIEZOMETER

Customer: B.C. Hydro Revelstroke
Date: 31-Mar-11
Serial Number: 45949
Model Number: ELSPG510VA-015
Cable Length: 60 ft
Cable Type: Vented

Pressure Range: 15 PSIG
Supply: 10-28 Vdc
Output: 4-20 mA
Thermistor: 3 kΩ
W.O. Number: Q019523

Applied Test Pressure PSIG	Transducer Output mA	Calculated Output PSIG	Full Scale Error %
0.00	4.000	0.00	0.00
3.00	7.199	3.00	0.00
6.00	10.399	6.00	-0.01
9.00	13.601	9.00	0.01
12.00	16.800	12.00	0.00
15.00	20.001	15.00	0.00

Cal Factor = 0.93742
Regression Zero = 3.9993

Output Pressure = Cal Factor * (Output - Regression Zero) PSIG

Electrical Termination:
Red: Supply +
Black: Supply -
Blue Thermistor
White: Thermistor
Shield: Shield

Shipped Readings:

Output mA	Temperature °C	Barometric Pressure(kPa)	Date:
4.010	21.7	101.89	31-Mar-11

Applied Science Technologists and Technicians of British Columbia
22724
A.C.
AL CULLEY
AScT

Document Number.: ELL0186A

Sugar Lake Pis #2

Calibration Record

200 - 2050 Hartley Ave., Coquitlam, British Columbia, Canada V3K 6W5
Tel: 604.540.1100 • Fax: 604.540.1005 • Toll Free: 1.800.665.5599 (North America only)
e-mail: info@rstinstruments.com • Website: www.rstinstruments.com

STRAIN GAUGE PIEZOMETER

Customer:	B.C. Hydro Revelstroke
Date:	31-Mar-11
Serial Number:	45956
Model Number:	ELSPG510VA-015
Cable Length:	60 ft
Cable Type:	Vented
Pressure Range:	15 PSIG
Supply:	10-28 Vdc
Output:	4-20 mA
Thermistor:	3 kΩ
W.O. Number:	Q019523

Applied Test Pressure PSIG	Transducer Output mA	Calculated Output PSIG	Full Scale Error %
0.00	4.001	0.00	0.00
3.00	7.200	3.00	-0.01
6.00	10.402	6.00	0.00
9.00	13.603	9.00	0.01
12.00	16.803	12.00	0.00
15.00	20.002	15.00	-0.01

Cal Factor = 0.93737
Regression Zero = 4.0008

Output Pressure = Cal Factor * (Output - Regression Zero) PSIG

Electrical Termination:
Red: Supply +
Black: Supply -
Blue Thermistor
White: Thermistor
Shield: Shield

Shipped Readings:

Output mA	Temperature °C	Barometric Pressure(kPa)	Date
4.010	23.4	101.89	31-Mar-11

Applied Science Technologists and Technicians of British Columbia
22724
A.C.
AL CULLEY
AScT

Document Number.: ELL0184A

innovation in geotechnical instrumentation

Calibration Record

RST Instruments Ltd., 11545 Kingston St., Maple Ridge, British Columbia, Canada V2X 0Z5
Tel: 604 540 1100 • Fax: 604 540 1005 • Toll Free: 1 800 665 5599 (North America only)
e-mail: info@rstinstruments.com • Website: www.rstinstruments.com

STRAIN GAUGE PIEZOMETER

SGR_RA

Customer:	B.C. HYDRO	**Customer ID:**	PS13-1
Date:	4-Mar-13	**Pressure Range:**	35 PSI
Serial Number:	47669	**Supply:**	10-28 Vdc
Model Number:	ELSGP510SA	**Output:**	4-20 mA
Cable Length:	19 m	**Thermistor:**	3 kΩ
Cable Type:	EL380004	**W.O. Number:**	Q023940

Applied Test Pressure PSI	Transducer Output mA	Calculated Output PSI	Full Scale Error %
0.000	3.998	0.00	0.001
7.000	7.198	7.00	0.000
14.000	10.398	14.00	-0.001
21.000	13.598	21.00	-0.003
28.000	16.799	28.00	0.002
35.000	19.999	35.00	0.001

Cal Factor = 2.1873
Regression Zero = 3.9978

Output Pressure = Cal Factor * (Output - Regression Zero) PSI

Electrical Termination:
Red: Supply +
Black: Supply -
Green: Therm+
White: Therm-
Shield: Shield

Shipped Readings:

Output mA	Temperature °C	Barometric Pressure(kPa)	Date:
4.080	21.3	101.16	05-Mar-13

Applied Science Technologists and Technicians of British Columbia
22724
AC
AL CULLEY
AScT

Document Number.: ELL0184A

innovation in geotechnical instrumentation

Calibration Record

RST Instruments Ltd., 11545 Kingston St., Maple Ridge, British Columbia, Canada V2X 0Z5
Tel: 604 540 1100 • Fax: 604 540 1005 • Toll Free: 1 800 665 5599 (North America only)
e-mail: info@rstinstruments.com • Website: www.rstinstruments.com

STRAIN GAUGE PIEZOMETER

Customer:	B.C. HYDRO	**Customer ID:**	SGR_RA PS13-2
Date:	4-Mar-13	**Pressure Range:**	35 PSI
Serial Number:	47652	**Supply:**	10-28 Vdc
Model Number:	ELSGP510SA	**Output:**	4-20 mA
Cable Length:	19 m	**Thermistor:**	3 kΩ
Cable Type:	EL380004	**W.O. Number:**	Q023940

Applied Test Pressure PSI	Transducer Output mA	Calculated Output PSI	Full Scale Error %
0.000	4.000	0.00	0.001
7.000	7.200	7.00	0.001
14.000	10.400	14.00	0.001
21.000	13.599	21.00	-0.005
28.000	16.800	28.00	0.001
35.000	20.000	35.00	0.001

Cal Factor = 2.1875
Regression Zero = 3.9999

Output Pressure = Cal Factor * (Output - Regression Zero) PSI

Electrical Termination:
Red: Supply +
Black: Supply -
Green: Therm+
White: Therm-
Shield: Shield

Shipped Readings:

Output mA	Temperature °C	Barometric Pressure(kPa)	Date:
4.080	21.3	101.16	05-Mar-13

Applied Science Technologists and Technicians of British Columbia
22724
A.C
AL CULLEY
AScT

Document Number.: ELL0184A

innovation in geotechnical instrumentation

Calibration Record

RST Instruments Ltd., 11545 Kingston St., Maple Ridge, British Columbia, Canada V2X 0Z5
Tel: 604 540 1100 • Fax: 604 540 1005 • Toll Free: 1 800 665 5599 (North America only)
e-mail: info@rstinstruments.com • Website: www.rstinstruments.com

STRAIN GAUGE PIEZOMETER

SGR-RA

Customer:	B.C. HYDRO	**Customer ID:**	PS13-3
Date:	4-Mar-13	**Pressure Range:**	35 PSI
Serial Number:	47668	**Supply:**	10-28 Vdc
Model Number:	ELSGP510SA	**Output:**	4-20 mA
Cable Length:	14 m	**Thermistor:**	3 kΩ
Cable Type:	EL380004	**W.O. Number:**	Q023940

Applied Test Pressure PSI	Transducer Output mA	Calculated Output PSI	Full Scale Error %
0.000	3.994	0.00	0.002
7.000	7.195	7.00	-0.001
14.000	10.396	14.00	-0.004
21.000	13.598	21.00	0.000
28.000	16.800	28.00	0.003
35.000	20.001	35.00	0.000

Cal Factor = 2.1865
Regression Zero = 3.9936

Output Pressure = Cal Factor * (Output - Regression Zero) PSI

Electrical Termination:

Red: Supply +
Black: Supply -
Green: Therm+
White: Therm-
Shield: Shield

Shipped Readings:

Output mA	Temperature °C	Barometric Pressure(kPa)	Date:
4.070	21.4	101.16	05-Mar-13

Applied Science Technologists and Technicians of British Columbia
22724
A.C
AL CULLEY
AScT

Document Number.: ELL0184A

APPENDIX C - Photogrammetric Modelling

Background

Photogrammetry is a measurement technique using light rays captured within two photographs to determine 3D data (Birch, 2006). These two overlapping photographs are known as a stereopair. The technique's premise is that the photographs, taken from different camera locations, have sample points within each photograph that match. Rays are extended from these points through the camera's perspective center to find the location where they intersect. Using multiple matching points for a greater level of accuracy, the 3D positions of the pixels can be determined, and measurements can be made.

Initially developed for use in computer vision applications, structure from motion (SFM) is a photogrammetric image processing technique (Turner et al., 2012). Software use multiple overlapping images to determine the adjusted coordinates of all points, the generation of sparse point clouds, and the determination of the camera pose parameters. To determine this information, multiple points that match within the two photos are used in an algorithm called a least-squares bundle block adjustment (Birch, 2006). Software will automatically detect these points. After determining the camera locations, further processing the images utilizing multiple stereo view (MSV) can be completed to create a dense point cloud (Tannant, 2015).

The densified point cloud created by the SFM/MVS processing is a valuable mapping tool that allows the software user to view areas of interest from multiple angles and magnifications that would not be possible in the field. Additionally, it allows a virtual revisitation of a job site to pick up uncollected or forgotten details. Each point within the cloud is assigned the colour attribute initially associated with the pixel it was derived from, aiding in differentiating between site features (Tannant, 2015). The densified point cloud is not the final software output; the densified point cloud is used to create digital surface models (DSM) or digital terrain models (DTM) through the construction of a triangular irregular network (TIN). Upon completion of the DTM, orthophotos and an orthomosaic can be created. Together these outputs provide the basis of interpretation, measurement, and mapping.

The first step in creating the DSM is the formation of a triangular irregular network (TIN). This is done through the use of a Delaunay triangulated net-work growth algorithm (TNGA). The automated creation of a triangulation mesh unit relies on three spatial points being chosen in sets, such that they have the shortest distance among them (Zhang et al., 2018). The key to the

TNGA is choosing the third point; the algorithm uses the Delaunay triangle discriminant rules. These rules are that each Delaunay triangle's circumcircle cannot contain any other point, and the smallest angle of a Delaunay triangle must be maximized.

Rock discontinuities are identified and classified by the use of a double-nested mean-shift cluster algorithm (MCA). Relative positions of triangular mesh units are classified by the inner MCA loop based on their relative positions. Triangular mesh units with near-identical normal vectors, classified based on normal vectors, are identified and classified by the MCA outer loop. The uneven shape of discontinuity surfaces causes pseudo discontinuity surfaces to occur in the extracted results (Zhang et al., 2018). It is crucial that, for the improvement of the quality of geological mapping, these be removed.

Another useful mapping output produced from SFM/MVS techniques is the orthophoto. An orthophoto is an aerial photograph taken vertically that has been corrected for lens distortions and elevation differences. These planimetric corrections create a uniform scale within the orthophoto, allowing measurements to be made, similar to how a traditional map would be used. These planimetric corrections are based on the created DTM; raw photographs are projected onto the DTM to correctly orientate the image's pixels (Mills & McLeod, 2013). From the individual orthophotos, an orthomosaic is created by stitching the photos together. This is completed in a manner that minimizes the visual transition between the images. In most cases, this cannot be seen at all.

Throughout the integration of UAV based photogrammetry as a standard practice in industry, there has been a concern with the accuracy of using these techniques compared to more traditional methods (Tannant, 2015). Presently, UAV-based photogrammetry is widely accepted and common practice within the geotechnical community. One of the highlights of using these techniques is the ability to customize the degree of accuracy to one’s specific project. There are two main focuses regarding photogrammetry’s accuracy, the accuracy of the matched pixels and the spatial accuracy of the model outputs.

Accuracy of the models generated by SFM/MVS point matching and by association, the spatial accuracy of the models is dependent on data collection/photo acquisition. Many factors play a role in affecting the captured photos, such as image quality, lighting conditions, and sharp edges, which can cause a problem with software’s feature detection (Martínez-Espejo Zaragoza et al., 2017). There are two main accuracy types within the image matching software; both are expressed in terms of ground pixel size. Ground pixel size is a function of the camera's distance, the focal length, and the pixel size of the camera’s sensor. A higher-quality camera will produce a more accurate model.

The two software accuracy categories are planimetric accuracy and depth accuracy. As the names imply, they are the accuracy of the pixel’s location in the plane perpendicular to the rays captured by the camera and the distance from the camera location, respectively. Planimetric accuracy depends on the software's ability to locate reference points; the reference points' quality is a function of the photos’ quality, encompassed by the factors mentioned above. Depth accuracy is a function of both the distance between cameras to the distance from the camera to a pixel and the planimetric accuracy. The depth accuracy is linearly proportional to the planimetric accuracy (Birch, 2006). Typical values of planimetric accuracy are 0.3 to 0.5 pixels, while typical values of depth accuracy 0.1 to 0.2 pixels (Birch, 2006), which for characterization of rock faces is more than sufficient (Tannant, 2015).

The absolute spatial accuracy of a correctly georeferenced model is also of a high standard. In comparison to creating DSM’s by traditional global navigation satellite system (GNSS) surveying, results can coincide within 2% of each other (Draeyer & Strecha, 2014). This is the relative accuracy; differences between the two methods are often due to the number of points used to create the surface model. GNSS surveys are completed akin to a traditional rod and total station type set up, and the number of points able to be collected is limited, in contrast to the created photogrammetric point cloud where point numbers above 1,000,000 are quite common (Zhang et al., 2018). In comparison to terrestrial light detection and ranging (LiDAR) techniques, the relative difference between constructed DSM’s is negatable, being reported at a similarity of 1.1% (Fazeli et al., 2016) and with lows of 0.1% (Draeyer & Strecha, 2014). The key to this process is to have high-quality ground control points.

UAV’s are generally equipped with low-grade GPS receivers that are not particularly accurate. Due to this, ground control is required to geospatially locate the generated software outputs. Absolute spatial accuracy can be approximately six times more accurate with ground control points compared to using relative only points (Turner et al., 2012). Ground control points also help the software locate pixels relative to each other during the application of the SFM/MSV algorithms; in cases where ground control points were applied, the accuracy of both drones increased, with an approximate increase of 10 times seen in the planimetric accuracy while the vertical accuracy increased by roughly 60 times (Madawalagama et al., 2015).

In theory, only 3 points are required to rotate and shift the model into the correct geospatial location after relative-only point matching has occurred. While this may be the case, it is best practice to obtain multiple ground control points to ensure redundancy. Alternatively, ground control points can also be obtained post-flight after the software has completed a relative-only bundle adjustment (Martínez-Espejo Zaragoza et al., 2017). This allows for the opportunity to assess the best ground control points to use based on the relative-only model. It has been found, though, that the number of ground control points increases the accuracy of the model logarithmically; there is a significant diminishing return on accuracy after using more than 2.5 ground control points per 100 photos (Sanz-Ablanedo et al., 2018). While it may be a diminishing return, obtaining and utilizing more ground control is always better.

An alternative to using ground control points as inputs to geo-reference the photogrammetric model is to use known camera locations; however, acquiring this information can be quite tricky. It is possible, though and can be completed using UAVs with real-time kinetic (RTK) sensors. Looking at the three different scenarios (using GNSS surveyed ground control only, using RTK receivers only, and using both GNSS and RTK data), the outcome is that using only GNSS ground control points had the best results. It has been shown that the use of the camera locations can decrease the accuracy by 0.4 pixels while removing the ground control points, and relying only upon the RTK, can decrease the accuracy by an additional 2.2 pixels. (Forlani et al., 2018).

Survey Tie in Points

A downside to the DJI Phantom 4 is the inaccuracy of the built-in GPS. Based on previous flight and photogrammetric modelling experience, the UAV’s GPS's accuracy can result in lateral inaccuracies in the range of ± 5 m and vertical inaccuracies in the range of ± 50 m. If relying solely on the UAV’s GPS, the modelled point cloud can become warped, tilted, and rotated. Because of this, ground control points are necessary.

To ensure the correct spatial location, ground control points were chosen based on BC Hydro’s 2013 survey data. Piezometer housings were chosen as control points due to their availability as pre-surveyed structures and their prominent visibility in the captured photographs. Additionally, the chosen points had enough spatial variability to ensure the model would not tilt or warp. Eleven control points were chosen in total; instruments R1 and R2, SP13-1 to SP13-3, SP13-5, DH97-1 to DH97-4, and L1 were the chosen ground control.

To make use of the survey data provided by BC Hydro, adjustments had to be made to the coordinates representing instrumentation DH97-1 to DH97-4, SP13-1 to SP13-3, and SP13-5. The 2013 survey was completed using traditional survey equipment, and as such, survey shots were taken at the lid welds location; conversely, the images captured pixels located on the top of the lid surface. As such, the elevations of the surveyed points were increased by 0.3048 m to coincide with the housing lid's elevation, as shown in Figure 39. Survey data for instrumentation R1, R2, and L1 were used with no adjustments as the survey measurements were taken from the housings' top. With these corrected ground control points and the acquired photos, a photogrammetric model was created.

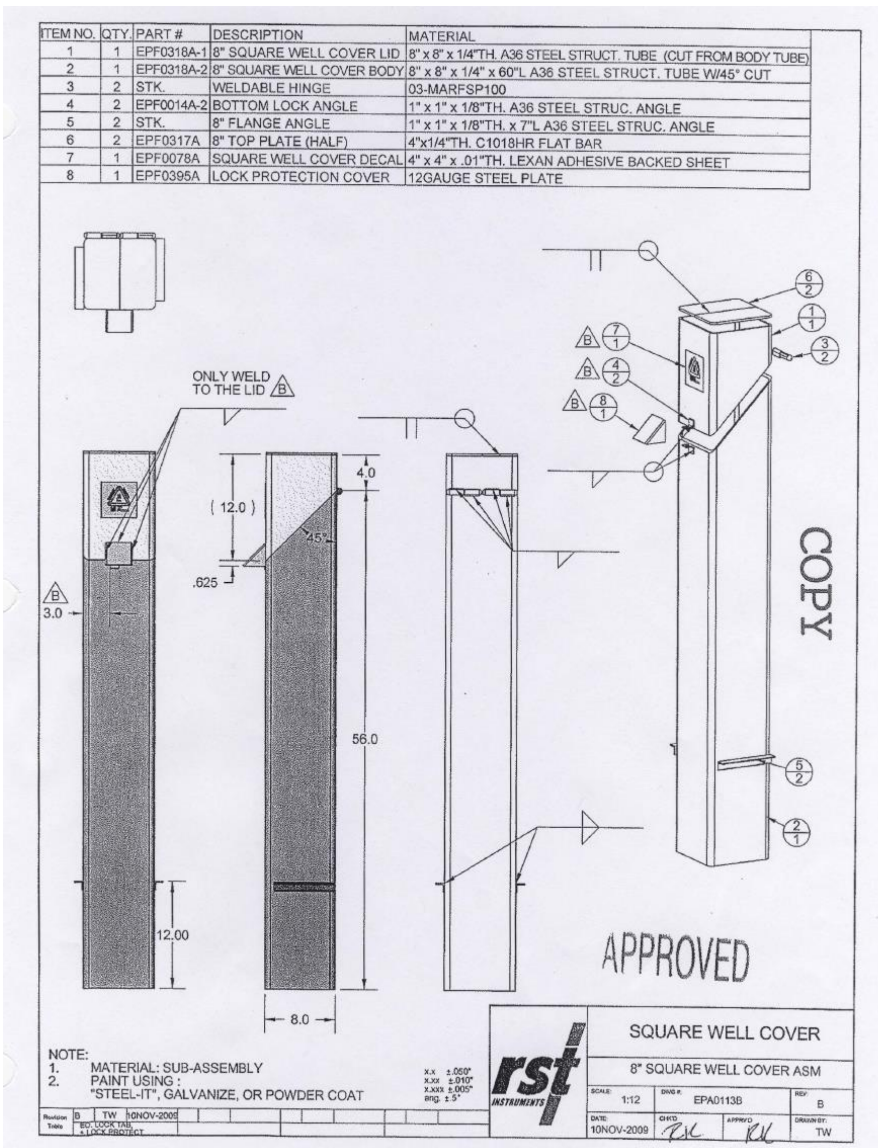

ITEM NO.	QTY.	PART #	DESCRIPTION	MATERIAL
1	1	EPF0318A-1	8" SQUARE WELL COVER LID	8" x 8" x 1/4"TH. A36 STEEL STRUCT. TUBE (CUT FROM BODY TUBE)
2	1	EPF0318A-2	8" SQUARE WELL COVER BODY	8" x 8" x 1/4" x 60"L A36 STEEL STRUCT. TUBE W/45° CUT
3	2	STK.	WELDABLE HINGE	03-MARFSP100
4	2	EPF0014A-2	BOTTOM LOCK ANGLE	1" x 1" x 1/8"TH. A36 STEEL STRUC. ANGLE
5	2	STK.	8" FLANGE ANGLE	1" x 1" x 1/8"TH. x 7"L A36 STEEL STRUC. ANGLE
6	2	EPF0317A	8" TOP PLATE (HALF)	4"x1/4"TH. C1018HR FLAT BAR
7	1	EPF0078A	SQUARE WELL COVER DECAL	4" x 4" x .01"TH. LEXAN ADHESIVE BACKED SHEET
8	1	EPF0395A	LOCK PROTECTION COVER	12GAUGE STEEL PLATE

Figure 39. Well cover drawing (BC Hydro, 2013).

Modelling and Results

Two different software suites were chosen for photogrammetric analysis, each with a different purpose in mind. The two chosen software packages were Pix4DMapper and ADAM 3DM Analyst Mine Mapping Suite. The software suites have more or less the same functionality in terms of computational analysis but differ in the available outputs. Pix4D excels in handling a large number of images and the creation of densified point clouds, DEM's, and orthomosaics. The program, unfortunately, cannot map joint properties. ADAM 3DM excels in this area and, as such, was used for this portion of the analysis.

Pix4DMapper was used to create a densified point cloud, DEM, and an orthomosaic from the first flight's images. Pix4DMapper is a single software application with an easy and intuitive setup; the user simply uploads the photos of interest and the location of ground control points (GCP), followed by choosing the GCP's in a handful of photos. From there, the software calibrates the camera characteristics, runs the least squares bundle adjustment, generates the densified point cloud, and creates a DEM and orthomosaic. The run time of a typical 100-300 photo model is generally around 8 hours, from start to finish.

Pix4DMapper was used to generate outputs for flights 1 and 2, with all images being loaded into the software. The models required 11 and 10.5 hours to run for flights 1 and 2, respectively. The point matching's planimetric accuracy was 0.36 pixels, while the depth accuracy of the point matching was 0.29 pixels. This level of matching accuracy is more than sufficient for the needs of this project.

To verify the model's spatial accuracy, the reservoir shoreline was checked for levelness to ensure the generated model was not tilted or warped. Six points were checked against, and all were within a reasonable range of elevations, showing little variation in the water surface. The water level within the reservoir was also compared to the staff gauge's measured reservoir level for that day, confirming the correctness of the model's elevation. Additionally, within the model, the dam's deck was compared to the survey elevation provided by BC hydro. These checks verified the model to be accurate in a magnitude more than sufficient for this work.

ADAM 3DM Analyst Mine Mapping Suite was also used in the photogrammetric analysis. The benefit this software has over Pix4DMapper is the ability to complete joint mapping. To do this, the software suite requires two different programs to be used. Using the program 3DM CalibCam, photos are uploaded along with known camera parameters such as focal length, pixel size, and sensor size. 3DM CalibCam then runs a camera calibration using two overlapping photos (a stereopair) to determine the aforementioned camera values based on the photos taken. Once the camera has been calibrated, it is able to run a least squares bundle adjustment on all uploaded photos to generate a sparse point cloud and matching stereopairs between all possible photo combinations. These outputs are saved as .ori files, which can be further analyzed in 3DM Analyst.

Using the stereopairs generated by CalibCam, Analyst will generate a DTM and an orthophoto. Next, the user can draw polylines in the software that pick up spatial points on the DTM, generating a plane perpendicular to the line. This is the rock feature plane with the attitude and orientation of the plane describing the dip and dip direction. The downside to the ADAM software suite is its inability to generate a DSM and orthomosaic based on all photos from the area of interest.

Six different stereo pairs were used to cover the area of the foundation. The accuracy of the pixel matching between stereo pairs was approximately 0.3 pixels for both the planar and depth accuracy of all analyzed sets. To verify the model's spatial location, discernable features were picked and compared against the verified Pix4D model.

The completed joint mapping agrees with BC Hydro's joint mapping (BC Hydro, 1984). The report details primary bedding planes with a dip/dip direction of 28/35. Additionally, the shear planes mentioned in the report were identified. Over a hundred features were measured within 3DM Analyst and plotted on a stereonet, as shown in Figure 40. The majority of mapped were bedding planes, with a small number of joints identified. Joints were generally perpendicular to each other and more difficult to observe due to the elevation of the downstream water and the mist created by water spilling from the dam.

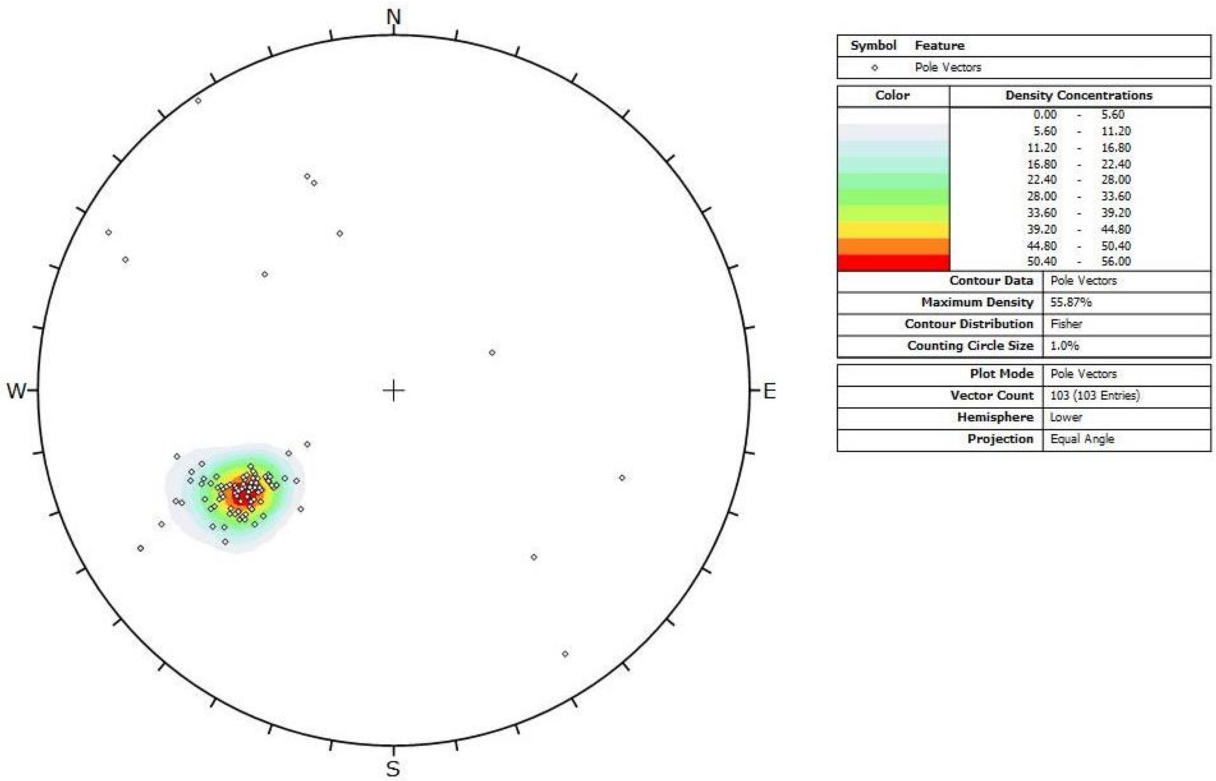

Figure 40. Stereonet of Sugar Lake Dam exposed foundation rock (2018).

APPENDIX D - Statistical Analysis

Linear Dependence of Data

The first useful tool in a time series analysis of an aquifer system is autocorrelation analysis (Imagawa et al., 2013), allowing for quantification of the linear dependence of successive values over time and the memory effect of the system (Tan et al., 2007). Autocorrelation analysis is useful for evaluating river-aquifer interactions (Bailly-Comte et al., 2008) and examining recharge processes in unconfined aquifers (Lee and Lee, 2000; Zhang and Schilling, 2004). An aquifer's memory effect has been primarily studied in karst aquifers (Imagawa et al., 2013) to categorize aquifers in different combinations of flow paths (Larocque et al., 1998; Gárfias-Soliz et al., 2010). It was shown in these studies that a short-term increase in water level had a long-term effect on subsequent water levels, i.e., a memory effect. In alluvial aquifers, the concept of memory effect has been less studied, with research in the area only being produced within the past ten years (Imagawa et al., 2013: Duvert et al., 2015; Chiaudani et al., 2017)

The autocorrelation of a data set is determined by calculating the data set's covariance with itself, lagged by successive values. The equations below show this, where n is data set length, k is the lag amount, x_t is the series observation at time t, and $\bar{x}$ is the series mean. If the data set is random, the autocorrelations will be significantly uncorrelated for all lags. If the data set is non-random, then one or more of the autocorrelations will be significantly non-zero. The significance level of autocorrelation plots is typically 5%.

Sample auto covariance:

$$c_k = \frac{1}{n}\sum_{t=1}^{n-k}(x_t - \bar{x})(x_{t+k} - \bar{x})$$

Sample autocorrelation:

$$r_k = \frac{c_k}{c_0} = Cor(x_t, x_{t+k})$$

Confidence interval:

$$95\% = -\frac{1}{n} \pm \frac{2}{\sqrt{n}}$$

The daily data's ACF plots are shown in Figure 41 and Figure 42 for lag values up to 1095 and 100. This is equivalent to lagging the time series by itself over 3 years and 100 days. It can be seen that there is a high level of seasonality in the data set from the sinusoidal pattern of the 3-

year lag plot. Large positive and negative correlations occur at near yearly intervals and are offset by approximately half a year. This coincides with seasonal patterns of both reservoir inflows and regional groundwater levels. The data sets lose memory and become insignificantly autocorrelated at lags of 85, 81, 87, and 83 days for P1, P2, P3, and the reservoir, respectively. The ACF plots of quarter daily data are shown in Figure 43. These are shown to lag values of 8, equivalent to 2 days. It can be seen that the correlation between quarter daily readings is near 1 for all lags. The data displays a large amount of linear dependence upon itself at small lags.

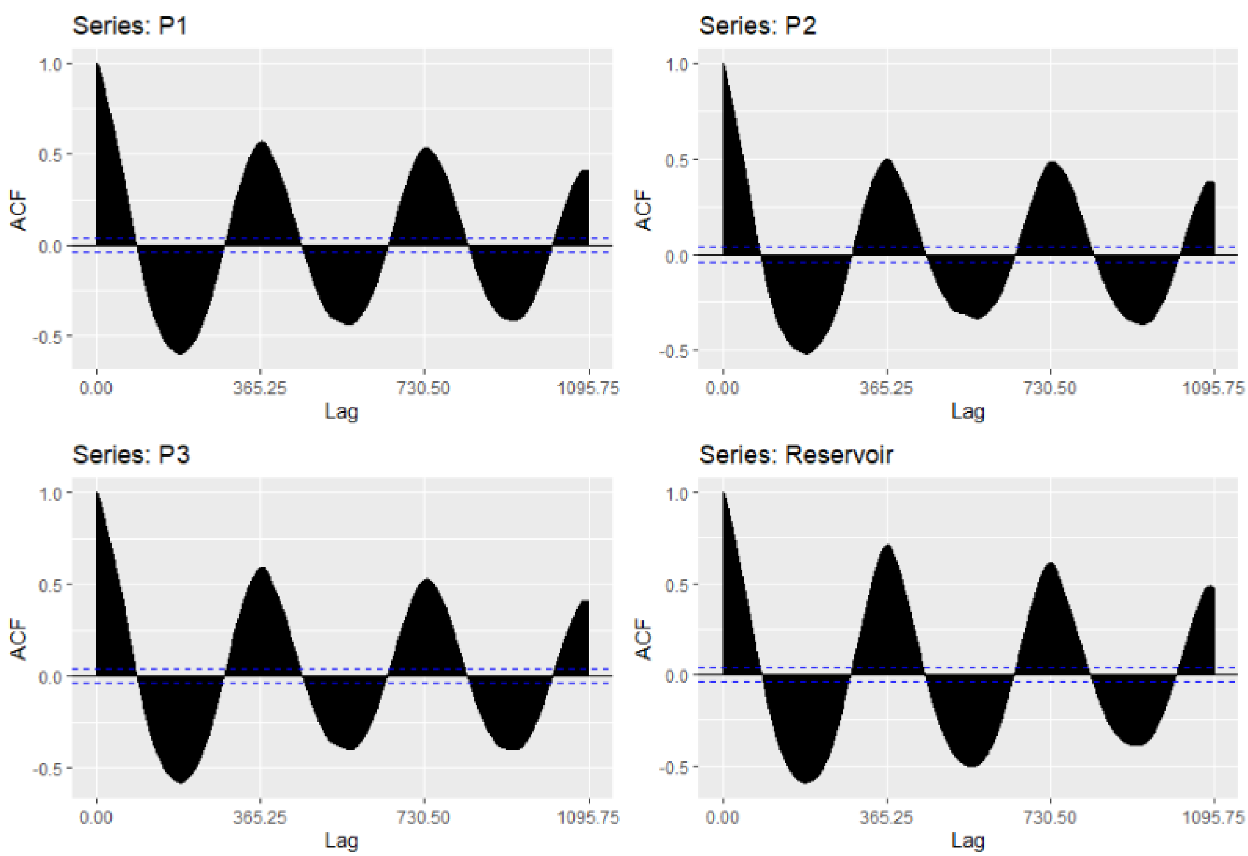

Figure 41. ACF plot to a lag of 3 years.

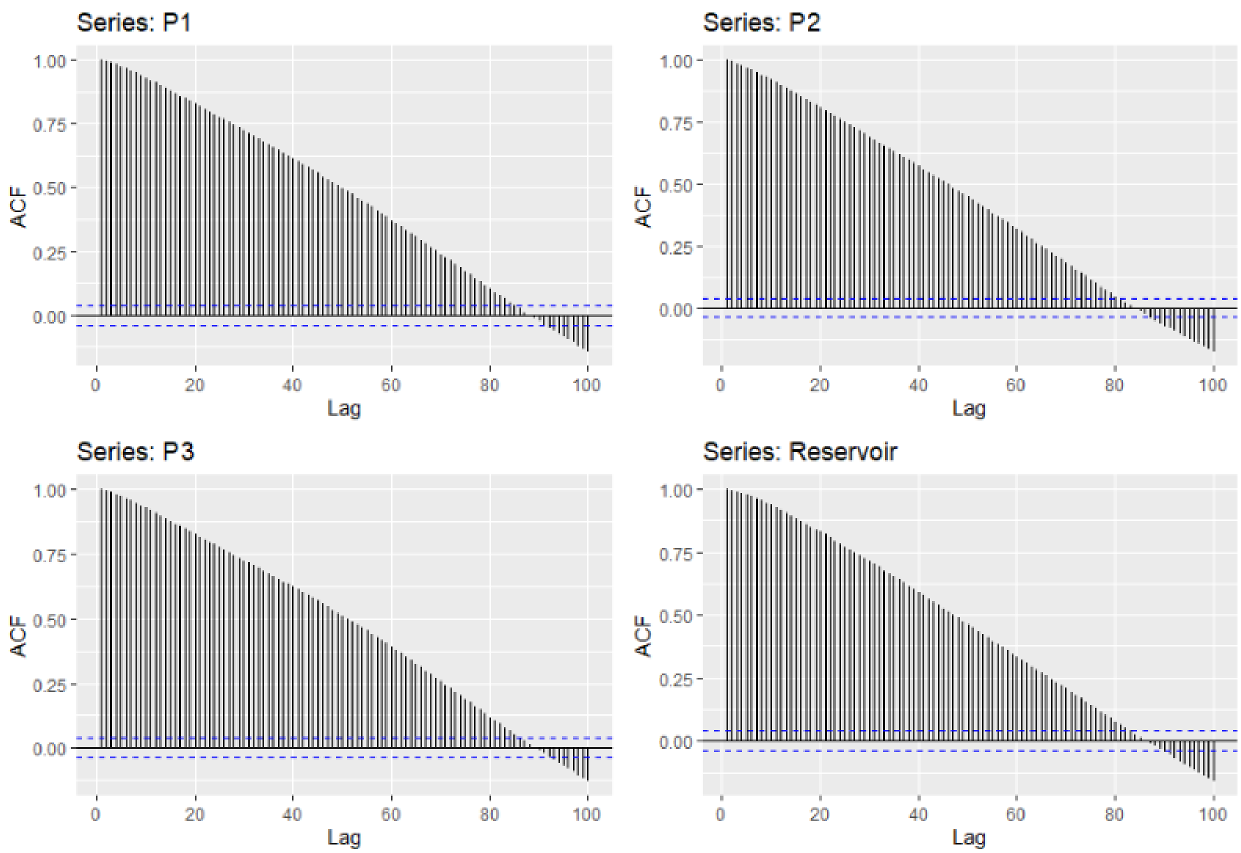

Figure 42. ACF plot to a lag of 100 days.

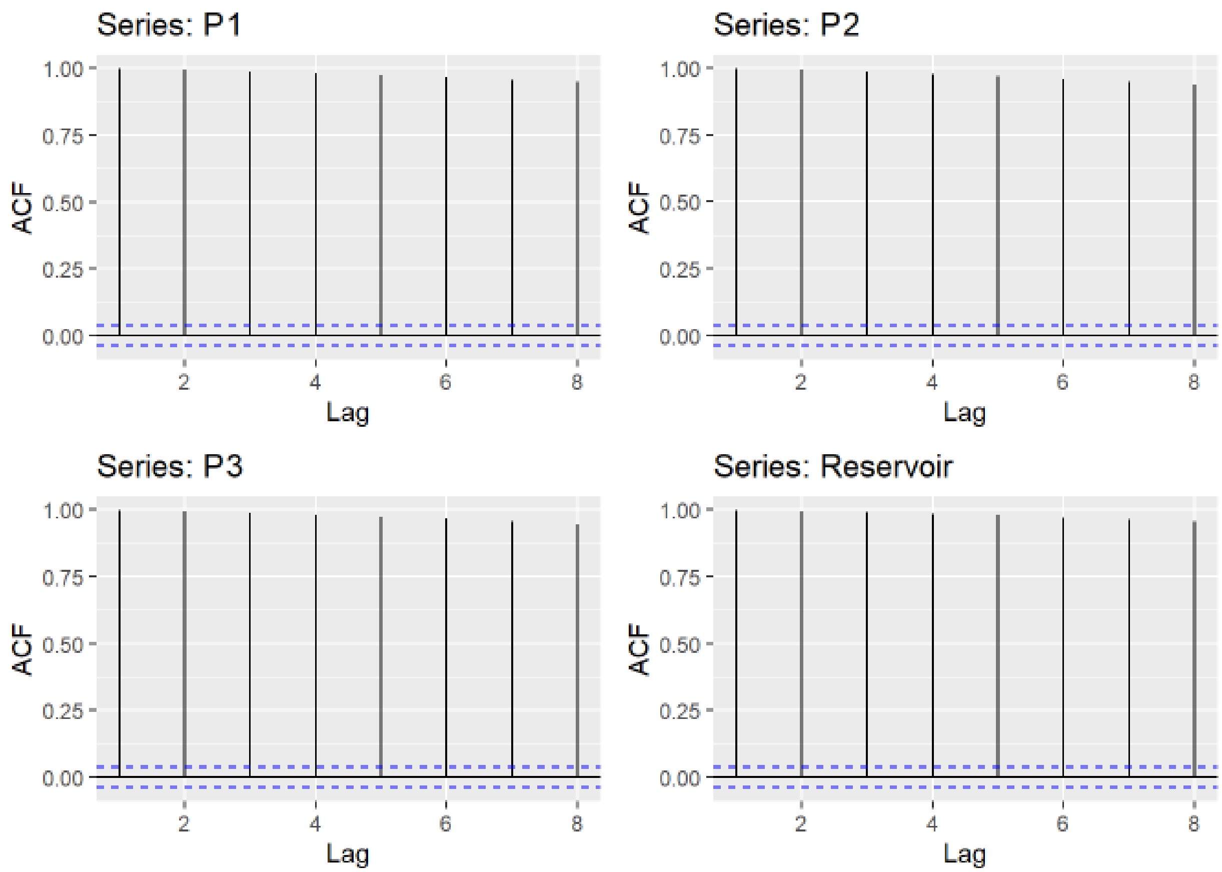

Figure 43. ACF plot to a lag of 2 days (1 lag= 6 hours).

Data Trends

The non-parametric Mann-Kendall test (Mann, 1945; Kendall, 1975) is widely used to evaluate statistically significant trends in hydrological time series (Ribeiro et al., 2015). The test has been used extensively in groundwater hydrology to detect trends in piezometric data (Rivard et al., 2009; Panda et al., 2012, Tabari et al., 2012). Chen et al. (2004) used trend analysis to show significant correlation between groundwater levels, precipitation, and temperature in a carbonate aquifer in Manitoba.

As the Mann-Kendall test only determines the presence of trend, the Sen method (Theil 1950, Sen 1968) is often used in conjunction as an unbiased estimator of trend slope and magnitude. The Sen method is not greatly affected by gross data errors, outliers, or missing data, unlike linear regression (Ribeiro et al., 2015). Compared to linear regression on highly skewed data, it has a higher precision, although this is the opposite case compared to a more normally distributed data set (Gibrilla et al., 2018).

The Mann-Kendall test was used to determine if there is a monotonic (consistently increasing or decreasing) trend of the piezometer and reservoir levels over the observation period. The Mann-Kendall test is a non-parametric statistical test for trend (randomness with time) and has been used extensively in the fields of climate science, hydrology, and groundwater science due to its freedom from statistical distribution. The Mann-Kendall test's null hypothesis is that the data comes from a population where the random variables are independent and identically distributed, i.e., there is no trend. The alternate hypothesis is that the data set has a monotonic trend. Based upon the determined S statistic and S's variance, the Z statistic of the normal distribution is determined. This is then compared to the critical Z values of ±1.96, coinciding with a confidence interval of 95%. Positive and negative Z scores represent positive and negative trends, respectively.

Mann-Kendall S Statistic:

$$S = \sum_{i=1}^{n-1} \sum_{j=i+1}^{n} sgn(x_j - x_i)$$

Mann-Kendall sign determination:

$$sgn(x_j - x_i) = \begin{cases} 1\ if\ (x_j - x_i) > 0 \\ 0\ if\ (x_j - x_i) = 0 \\ -1\ if\ (x_j - x_i) < 0 \end{cases}$$

The Sen’s Slope estimator test is commonly used in conjunction with the Mann-Kendall test. It is a procedure to estimate the magnitude of the actual change per unit of time and is insensitive to outliers. As with the Mann-Kendall test, Sen’s Slope is nonparametric. The test output is the slope of the data sets trend (Q_{med}) and the 95% confidence intervals of the slope. Positive and negative values of Q_{med} indicate increasing and decreasing trends, respectively.

Sen’s Slope Intermediate Slope Points:

$$Q_i = \frac{x_j - x_k}{j - k}\ for\ i = 1,2,\dots,N$$

Sen’s Slope:

$$Q_{med} \begin{cases} Q_{(N+1)/2} & if\ N\ is\ odd \\ \left(\frac{Q_{N/2} + Q_{(N+2)/2}}{2}\right) & if\ N\ is\ even \end{cases}$$

The p values of the raw data for P1, P2, and the reservoir indicate an insignificant monotonic trend at the 5% level. The Mann-Kendall test results in Table 3 show that P3 has a significant monotonic trend at the 5% level.

Table 8. Raw data trend testing results summary.

Data Set	Z score	p-value	Mann Kendal			Sens's slope		
			S	Var(S)	Tua	95% confidence limits		Sen's slope
P1	0.1806	0.8567	7.92×10^{3}	1.92×10^{9}	2.37×10^{-3}	-1.46×10^{-5}	1.77×10^{-5}	1.48×10^{-6}
P2	-1.5641	0.1178	-6.86×10^{4}	1.92×10^{9}	-2.05×10^{-2}	-2.20×10^{-5}	2.53×10^{-6}	-9.92×10^{-6}
P3	-10.34	$<2.2 \times 10^{-16}$	-4.54×10^{5}	1.92×10^{9}	-1.36×10^{-1}	-1.58×10^{-4}	-1.09×10^{-4}	-1.34×10^{-4}
Reservoir	-0.3076	0.7584	-1.35×10^{4}	1.92×10^{9}	-4.03×10^{-3}	-9.05×10^{-5}	6.36×10^{-5}	-1.21×10^{-5}

The literature presents conflicting ideologies on the impacts of a data set's linear dependence on the Mann-Kendall test results. A basic assumption of the Mann-Kendal trend test is that the data is randomly ordered. This is rarely the case for hydrological data, which tends to be serially correlated. It has been found that the Mann-Kendall test produces a type 1 error, meaning that trend is considered present when there is no trend, when applied to serially correlated data (Bayazit & Önöz, 2007). This is because as the magnitude of the autocorrelation increases, so does the magnitude of the Mann-Kendall test statistic's variance (Yue et al., 2002) and the variance of the trend slope estimate (Matalas & Sankarasubramanian 2003).

Prewhitening the data corrects for this; prewhitening is the transformation of an autocorrelated series into white noise, i.e. an uncorrelated series. This is completed, most commonly, by assuming a first-order autoregressive (AR1) model of the time series and applying the model's coefficients to correct the inflation of the variance (Hamed, 2009). Yu et al (2002) studied the effects of prewhitiening through an AR1 model using Monte Carlo simulations, finding that prewhitening through this method leads to potentially inaccurate assessment of the trend's significance. Hamed (2009) showed that failing to prewhiten data, prewhitening data without trend removal, and prewhitening with trend removal resulted in unacceptable rates of rejection of the null hypothesis of the Mann–Kendall test. It was found by Yue and Wang (2002) that when sample size and magnitude are large enough, autocorrelation does not significantly affect the Mann-Kendall test and prewhitening is discouraged.

As ambiguity is present on whether data should be prewhitened or not, prewhitening was applied to the data using the methodology of Hamed and Rao (1996), and the Mann-Kendall test was again performed. The Mann- Kendal test results using pre whitened data are the same as without using pre-whitened data. P1, P2 and the reservoir have p values greater than 0.05, and therefore the null hypothesis of no monotonic trend cannot be rejected. For P3, the null hypothesis of no monotonic trend is rejected, and the alternate hypothesis of the presence of monotonic trend is accepted. The results of the testing are shown below in Table 9.

Table 9. Pre-whitened trend testing results.

Data Set	**Z score**	**p-value**	**Var(S)**	**Tua**
P1	0.0599	0.9523	1.75×10^{10}	2.37×10^{-3}
P2	-0.5361	0.592	1.64×10^{10}	-0.0205
P3	-2.954	0.0031	2.36×10^{10}	-0.136
Reservoir	-0.0951	0.924	2.02×10^{10}	-4.03×10^{-3}

Seasonality

Seasonality is a characteristic of a time series in which the data experiences regular and predictable changes that recur every calendar year. Any predictable fluctuation or pattern that recurs or repeats over a one-year period is said to be seasonal. This is different from a cyclical effect as cyclical effects can span periods longer or shorter than a year. By visual inspection, all the data sets have a strong seasonal component; this is very common in hydrological data. Measurements are high in the spring months and low in the winter months. This pattern is most prominently seen in the reservoir level data, as shown below in Figure 44.

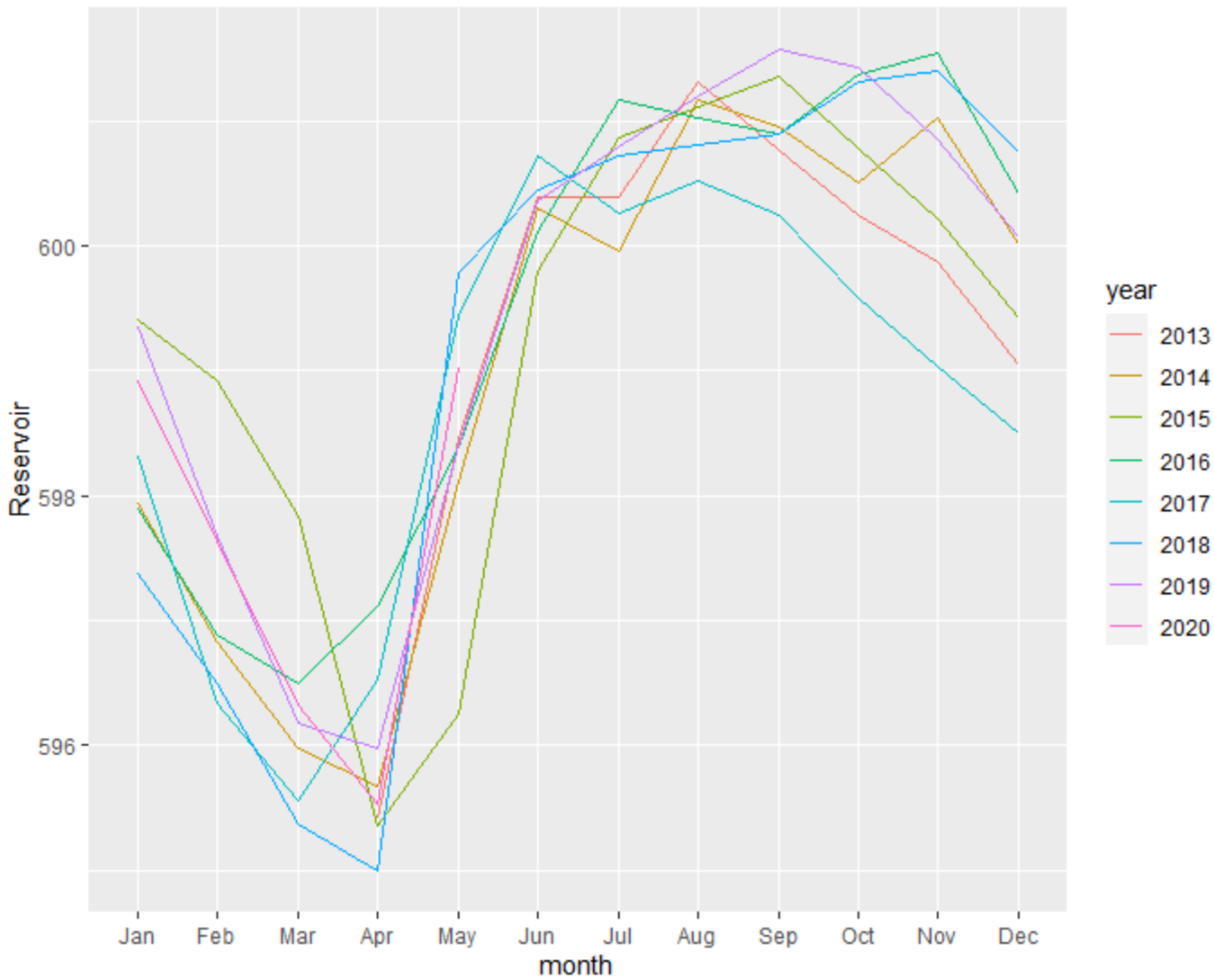

Figure 44. Seasonal reservoir fluctuation.

Data Set Decomposition

A hydrogeological time series can be regarded as an additive time series and, as such, can be decomposed into different components related to different processes acting in the generation of the time series (Gibrilla et al., 2018). A linear decomposition can help characterize recharge response and other impacts, allowing for the identification of similar and differing shape and variability components between boreholes (Taylor & Alley, 2002). An additive time series can be considered to be composed of three components, a seasonal component S_t, a trend component T_t, and a remainder, component R_t (Metcalfe & Cowpertwait, 2009). The series can be described in a linear fashion using these components, as

$$y_t = S_t + T_t + R_t$$

The trend component represents the long-term processes that take place over the length of the series, the seasonal (or cyclical) component represents the repeated cyclical process, and the remainder component is what is left after removing the trend and seasonal components from the raw data (Xia et al., 2019). A cyclical process taking place over periods longer than a year, ie the 7-year El Nino effect, that can occur in groundwater dynamics; however, because of the short length of the data sets in this study, these are more likely to be captured in the trend component of the decomposition. The remainder component is likely to represent any local process that causes variability between cycles. These are typically related to short-term events or impacts to the aquifer system; other variabilities, such as measurement issues or white noise, can be included in the remainder component but are likely to be less important for groundwater fluctuation compared to rainfall (Lafare et al., 2016).

In order to better describe and assess the features contained in the groundwater level responses, the STL (Seasonal and Trend decomposition using Loess) method of decomposition was employed (Cleveland et al. 1990). This method was first proposed by Cleveland (1979) and then later refined by Cleveland and Devlin (1988). The STL method is preferred over a linear regression as linear regressions do not provide an accurate assessment of nonlinear trends commonly present in groundwater levels (Shamsudduha, 2011). As the STL analysis is nonparametric in nature, structure otherwise undetectable through linear analysis is possible. Although generally considered an exploratory or descriptive technique (Taylor and Alley, 2002), STL decomposition has been used successfully to reveal data structure in the environmental field (Esterby, 1993; Shamsudduha et al., 2009; Lafare, 2016).

The STL procedure consists of a series of smoothing operations with different moving window widths to extract frequencies from the time series. The procedure uses an inner and outer loop (Yu et al., 2001), with the inner loop using several steps to separate trend and seasonal components from the raw data and the outer loop extracting residual components. Within the inner loop, a detrended series is computed by subtracting the trend from the original series, whereafter an initial seasonal component is formed by smoothing the detrended values. To filter out any remaining trend, a moving average is applied to the seasonal component.

The remainder component is then calculated in the outer loop as the difference between the raw series and the combined trend-seasonal components. This process is repeated several times to improve the accuracy of the estimations of the components. A detailed breakdown of the computational procedure is available in Yu et al. (2018). The removal of the trend and seasonal components remove the autocorrelation from the data set; the trend component is typically autocorrelated in granular aquifers due to the continuous nature of groundwater level change

(Lafare, 2016). The remainder component is, therefore, most likely representative of localized response to extreme hydrological events.

Smoothing parameters must be chosen to extract the trend and seasonal components; parameter choice determines the extent to which seasonal components vary year to year. Smoothing parameters were chosen as recommended by Cleveland et al. (1990), Carslaw (2005), and Shamsudduha et al. (2009). The data sets' decomposed components can be seen below in Figure 45, Figure 46, and Figure 47.

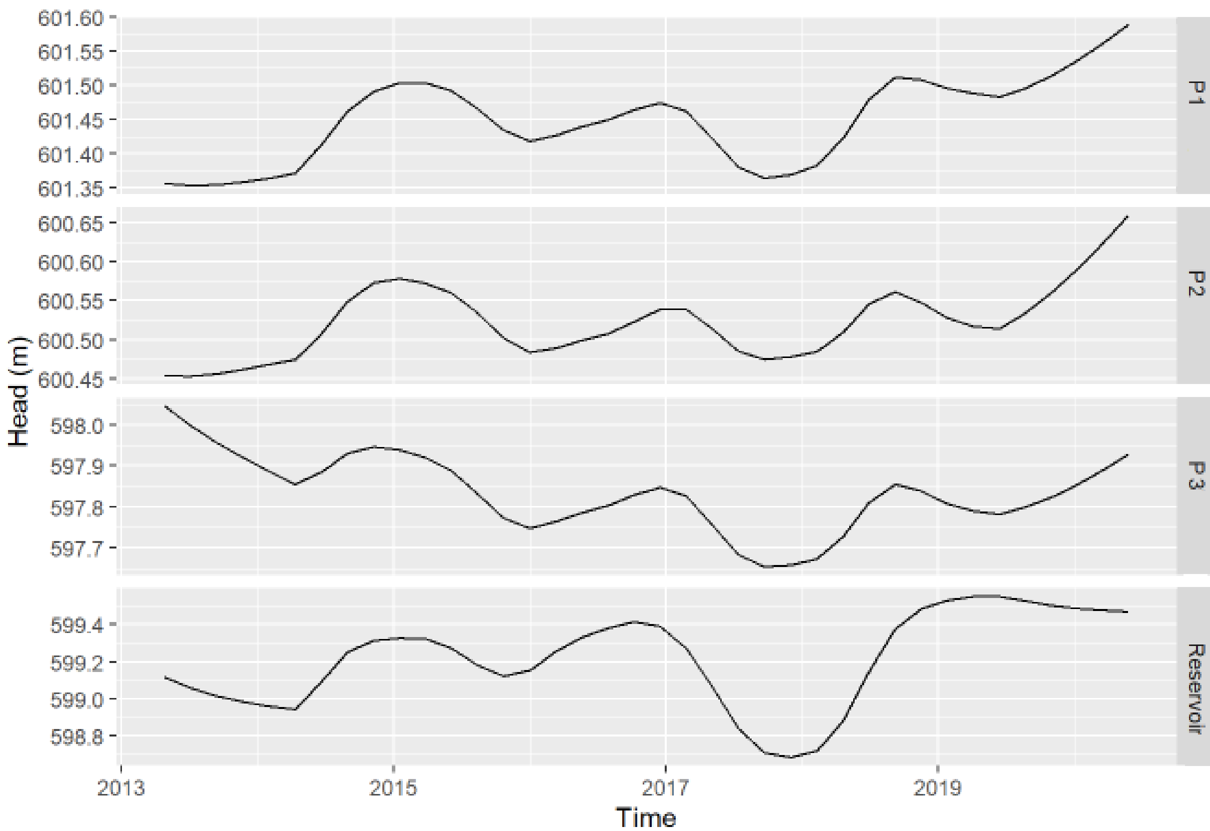

Figure 45. Trend components of STL decomposition.

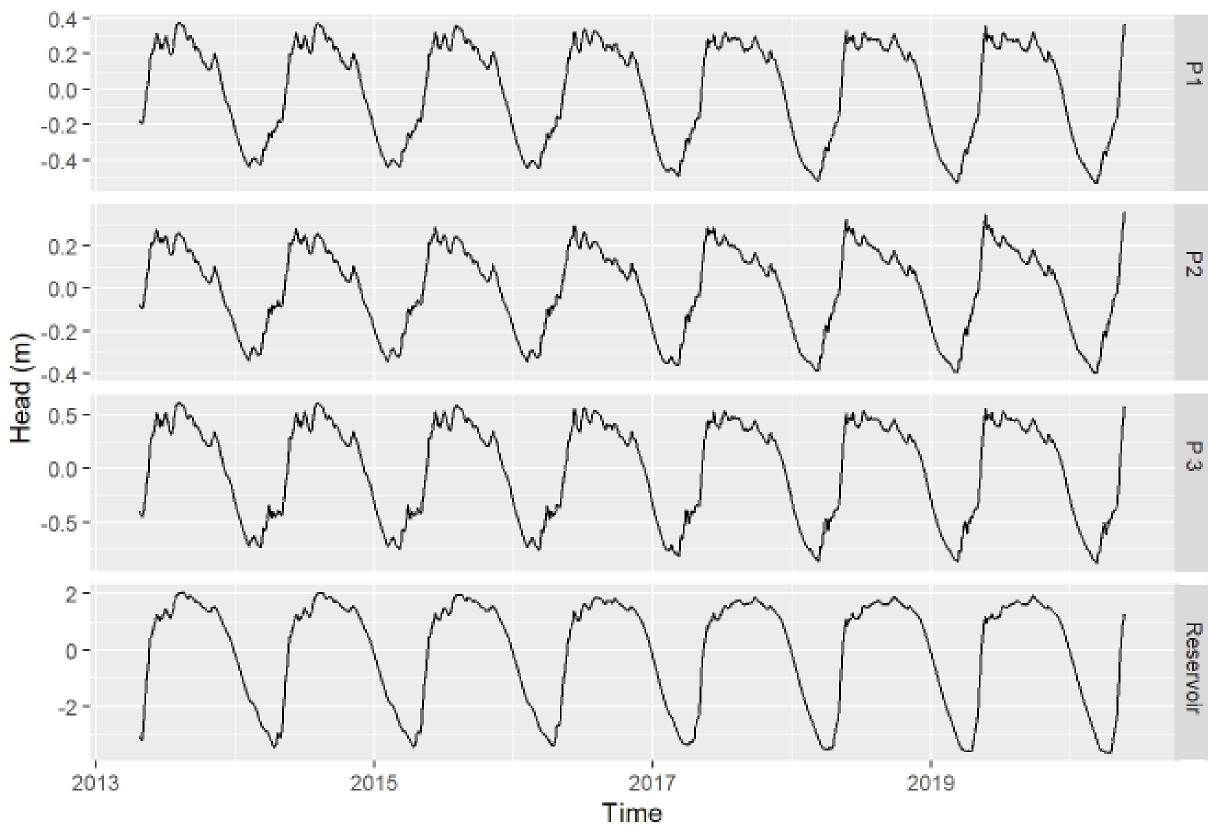

Figure 46. Seasonal components of STL decomposition.

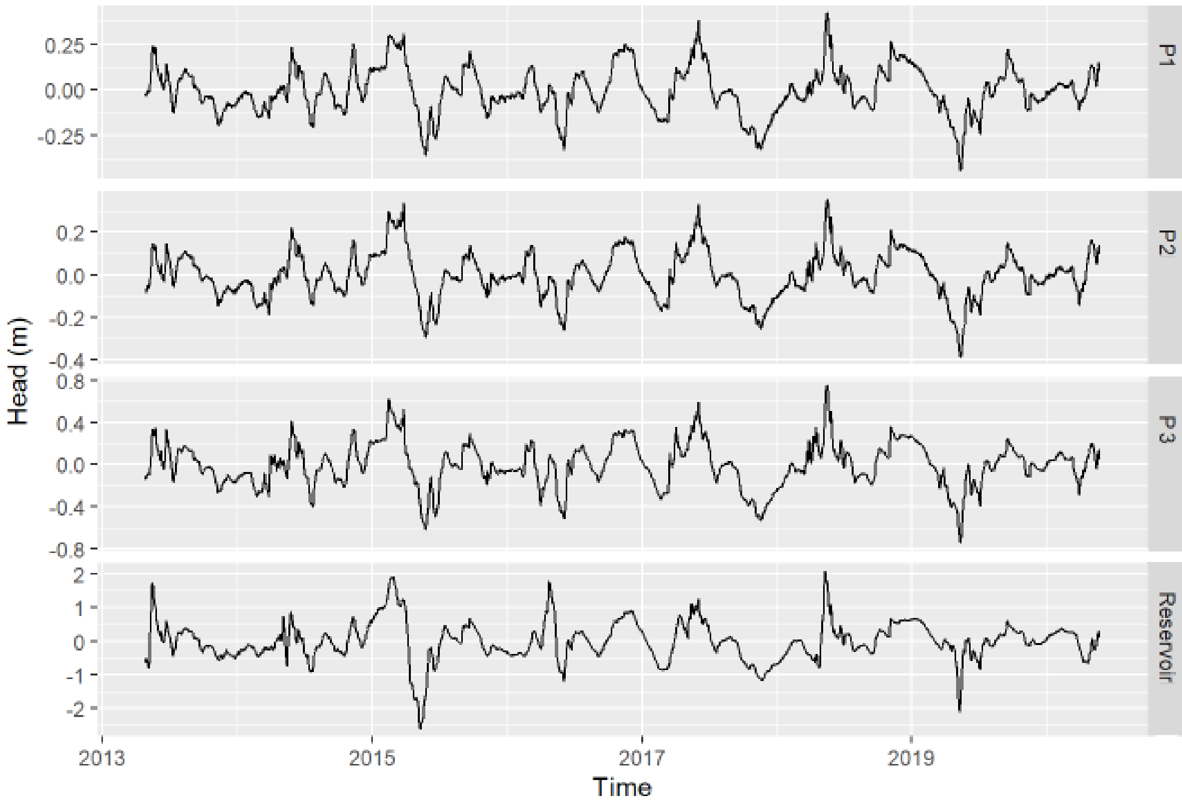

Figure 47. Remainder components of STL decomposition.

Visually, all the time series components are similar to each other, i.e. comparing trend to trend and seasonality to seasonality. All the trend components are relatively similar in shape. There is a distinction in the trends of P1 and P2 from P3 and the reservoir. P1 and P2 show an increase in trend from mid-2013 to early 2014, while P3 and the reservoir decrease during this period. From approximately 2014 to 2019, all series have the same trend shape. From early 2019 onward, the piezometers appear to be trending upward while the reservoir appears to be trending slightly downward.

The seasonality is very consistent for all data sets, with the reservoir being smoother than that of the piezometers. There is a slight change year to year for all data sets, but it is small, and the underlying signal is relatively consistent.

For all piezometers, the remainder component is indistinguishably the same, except for the data's spread. The reservoir closely matches the piezometers but with a smoother curve and a much larger spread in the data. The spreads, from largest to smallest, are the reservoir, P3, P1, and P2. This is likely due to an unaccounted data structure that was not removed by the decomposition process.

Distribution of Variance

A time series decomposition can be used to measure the strength of the trend (FT) and seasonality (FS) in a time series (Wang, Smith, & Hyndman, 2006; Hyndman & Athanasopoulos, 2018). For strongly trended data, the seasonally adjusted data should have much more variation than the remainder component. As such, the ratio of the variances should be relatively small. Data with little trend will have values of F_T close to 0. The strength of the trend can be defined as

Trend Strength:

$$F_T = max\left(0, 1 - \frac{Var(R_t)}{Var(T_t + R_t)}\right)$$

The strength of seasonality is defined similarly, but with respect to the detrended data rather than the seasonally adjusted data. Data with little seasonality will have F_S values close to 0. Based on the strength of the trend and seasonal components, the data sets' variance is mostly dominated by a seasonal component.

Seasonality Strength:

$$F_S = max\left(0, 1 - \frac{Var(R_t)}{Var(S_t + R_t)}\right)$$

Table 10. Trend and seasonality strength.

Data Set	**F_T**	**F_S**
PS1301	0.27	0.83
PS1302	0.24	0.78
PS1303	0.24	0.83
Reservoir	0.25	0.91

Similarly, each component's impact to the variance of the data set can be evaluated by comparing the ratio of the component variance to the total variance. Lafare (2016) showed it was possible to use these relationships to develop a relationship between hydrogeologic settings and investigate borehole hydrographs. The results of this calculation are shown in

Table 11 and the relative variances are plotted against each other in Figure 48. The red, black, and blue diamonds represent P1, P2, and P3, while the green diamonds represent the reservoir.

Table 11. Distribution of variance summary.

Data set	**Variance**	**Variance/Variance total**
P1 Trend	0.0035	0.0349
P1 Seasonal	0.0785	0.7926
P1 Remainder	0.0163	0.1650
P2 Trend	0.0018	0.0332
P2 Seasonal	0.0410	0.7365
P2 Remainder	0.0118	0.2121
P3 Trend	0.0075	0.0272
P3 Seasonal	0.2079	0.7590
P3 Remainder	0.0443	0.1617
Reservoir Trend	0.0604	0.0152
Reservoir Seasonal	3.4877	0.8772
Reservoir Remainder	0.3391	0.0853

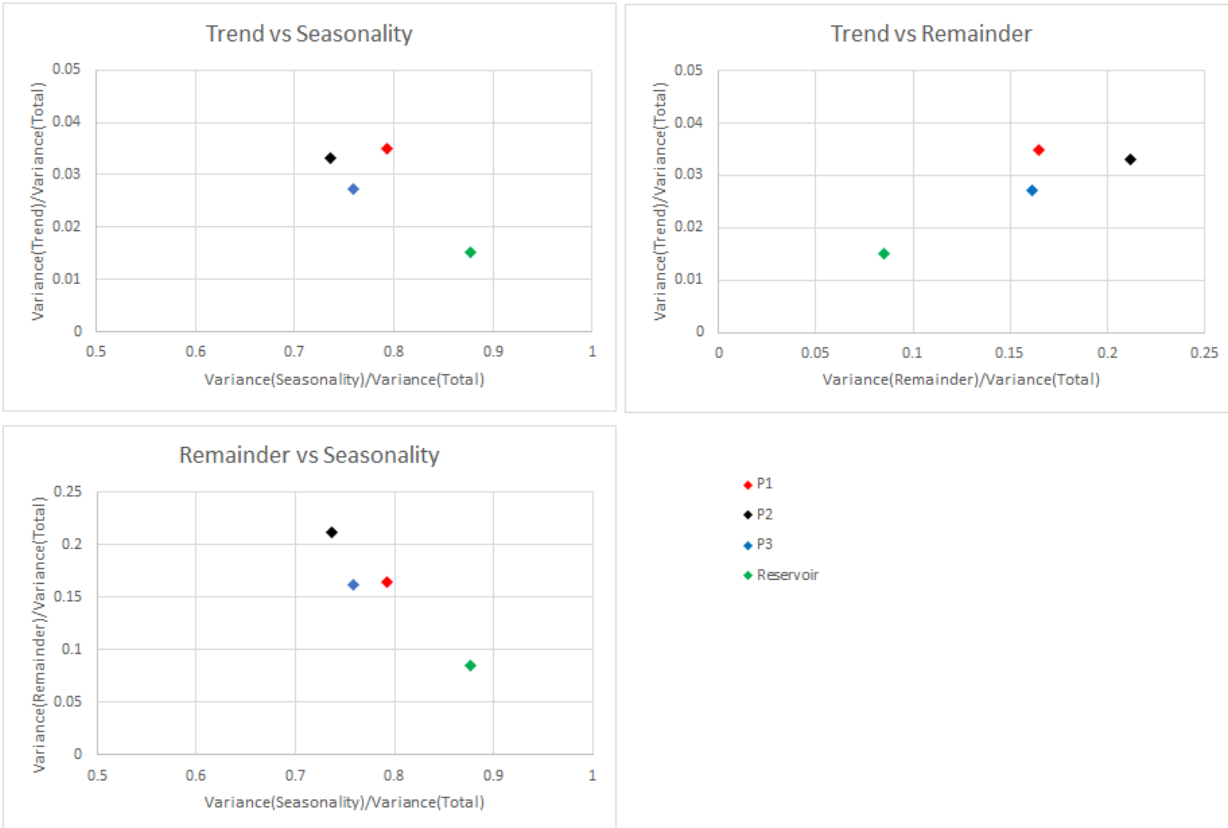

Figure 48. Graphical comparison of component ratio.

It can be seen that piezometers have a grouped aspect in comparison to the reservoir. Their variances are more influenced by a combination of seasonality and remainder components, whereas the reservoir is more dominantly seasonality-driven. The trend aspect of all data sets is practically negligible, ranging from contributing 1.5 to 3.5 % of each set's total variance. The stronger seasonal component in terms of the reservoir's variance can be explained by the direct influence of seasonal hydrological events such as freshet. For the piezometers, this is damped because the water has the additional restriction of flowing through the ground. When looking at the piezometers, P1 and P3 likely have stronger variance influence from seasonality because of their proximity to the reservoir. This is also likely the case with P2’s larger trend component; it is situated farthest from the reservoir and is most likely to be affected most by regional groundwater fluctuations. While it has been demonstrated that a higher variance of seasonality is correlated to lower hydraulic conductivities and porosities (Lafare, 2016), it is likely the case in this instance that the effects of the reservoir drown out any signals from this factor.

Remainder Autocorrelation

Autocorrelation was calculated for the remainder components of the time series, as seen in Figure 49. It was not calculated for the trend and seasonal components as, by definition, they are autocorrelated. As mentioned above, the remainder component should have no autocorrelation, indicating a structure to the data that is not explained by the trend or seasonality. All series have a relatively strong memory, taking an excess of 50 days to lose significant linear dependence, indicating a relatively homogenous system with significant storage. The ACF's overall slope is steeper for the reservoir due to a system with less of a storage effect than the piezometers. All time series have a decreasing slope at increasing lags. PS3 initially has the steepest slope of the piezometers but has an inflection point around 25 lags to become the shallowest slope.

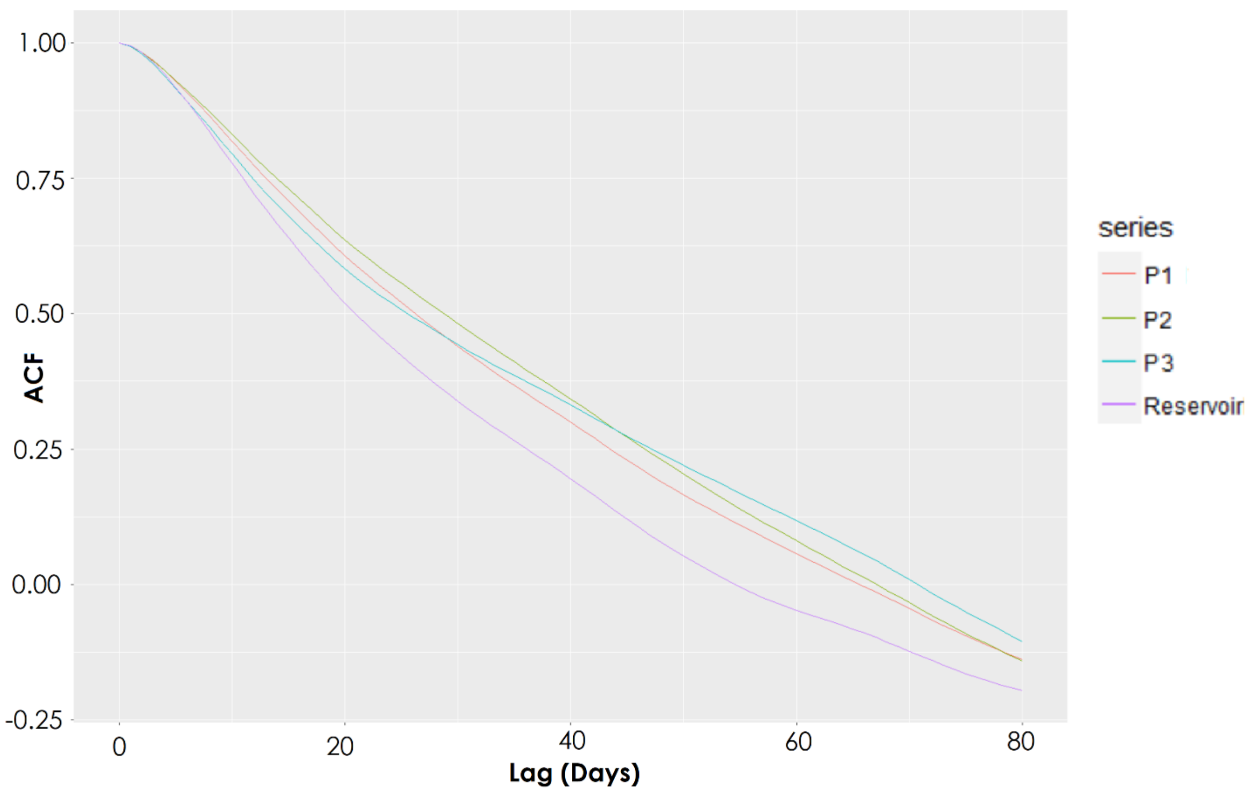

Figure 49. ACF plot of remainder components.

Spectral Analysis

Spectral analyses are complementary to correlation analyses, revealing characteristics that are often buried in noise and otherwise undiscernible (Box & Jenkins,1976; Percival & Walden, 1993). Analysis in the frequency domain allows for data manipulation and signal frequency extraction, providing a picture of the data that is unclear when analyzed in the time domain (Acworth et al., 2015). The key goal is to detect average periodicities in long time series to determine dominant oscillations and frequency bands of interest (Andreo et al., 200; Gill et al., 2013).

Spectral analysis has been applied within the hydrologic sciences field for decades, most commonly to estimate coefficients of regression models (e.g. Bras & Rodriguez, 1985; Hameed, 1984). However, there is little evidence of extensive use in hydrogeologic studies (Acworth et al., 2015). Spectral analysis has generally been limited to deep confined and unconfined aquifers (Hseih et al., 1987; Merritt, 2004) or shallow karst aquifers (Jukić & Denić-Jukić, 2004). Kendall and Hyndman (2007), Imagawa et al. (2013), and Duvert (2015) have all recently employed spectral methods in the analysis and characterization of shallow unconfined aquifers.

The spectrum of a time series is innately useful for describing the distribution of variance as a function of frequency, with the frequency spectrum of a time series and its autocovariance function being linked by the general Fourier expression (Jenkins & Watts,1968). It is complimentary to correlation analysis, with the power spectrum being the translation of the autocovariance of a time series to the frequency domain (Chiaudani et al., 2017). The autocovariance function is linked to the frequency domain by the general Fourier expression:

Power Spectrum Function:

$$ps(f) = \sum_{k=-N}^{N-1} c_x(k)\, e^{-2\pi i f k}$$

Where $ps(f)$ is the power spectrum of the time-series x, $c_x(k)$ is its autocovariance function, f is the frequency of the kth mode, and i is the imaginary unit. Because the autocovariance function is symmetrical about positive and negative lags, and the series of the piezometers and reservoir are real-valued (Duvert, 2015), the equation can be rewritten as:

Simplified Power Spectrum Function:

$$ps(f) = \sigma_x^2 + 2\sum_{k=-N}^{N-1} c_x(k) \cos{(2\pi f k)}$$

The power spectral density is most frequently estimated through the use of a periodogram. Frequencies with higher peaks imply that the signal has a dominant component with the same frequency. The Lomb-Scargle method of periodogram calculation was used as it is derived from the classical Fourier spectrum analysis and was developed to detect weak signals in noisy data (Lomb, 1976; Scargle, 1982). Additionally, it allows for the calculation of significance limits (Press et al., 1994). While the Lomb-Scargle algorithm is typically used for unequally sampled data, it is more than capable of handling and applicable to equally spaced data such as those present at the Sugar Lake site.

The Lomb-Scargle periodogram function returns normalized power as a function of angular frequency and normalized frequencies in the [0,0.5] range (Press, 1989). The normalized power is based upon the total variance and allows for the determination of statistical significance. This frequency range corresponds to the Nyquist frequency, i.e. half the sampling rate, and is the highest frequency that the sampled signal can unambiguously represent (Scargle, 1982). The dominant frequencies for all data sets were within the 0 to 0.05 range, and as such, only this portion has been plotted. The periodograms of the analyzed time-series data can be seen below in Figure 50. Periodograms were created from the raw data and the decomposed seasonal and remainder components of the piezometer and reservoir data sets.

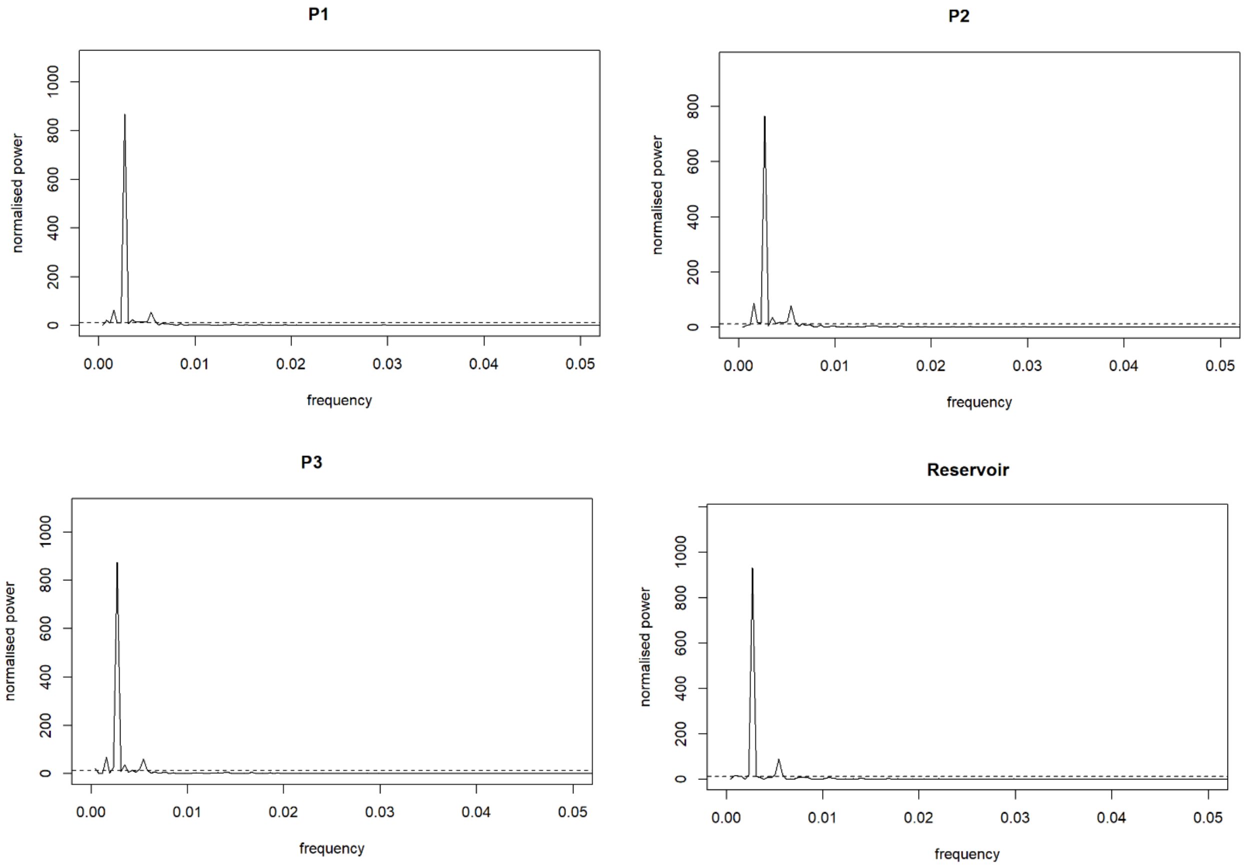

Figure 50. Periodograms of the raw data sets.

When analyzing the raw data, the periodograms show that the piezometers have three dominant signals while the reservoir only has two. The piezometers have matching dominant periods of 370, 649, and 185 days. These correspond to periods of approximately 1 year, 2 years, and half a year. The power of the yearly period signals is much stronger than that from the two-year and half-year periods, which have roughly the same spectral density. The reservoir has the same significant periods of a year and half a year, with the spectral density of a yearly signal far exceeding that of a half year. The reservoir does not have any recognizable signal from a 2-year period.

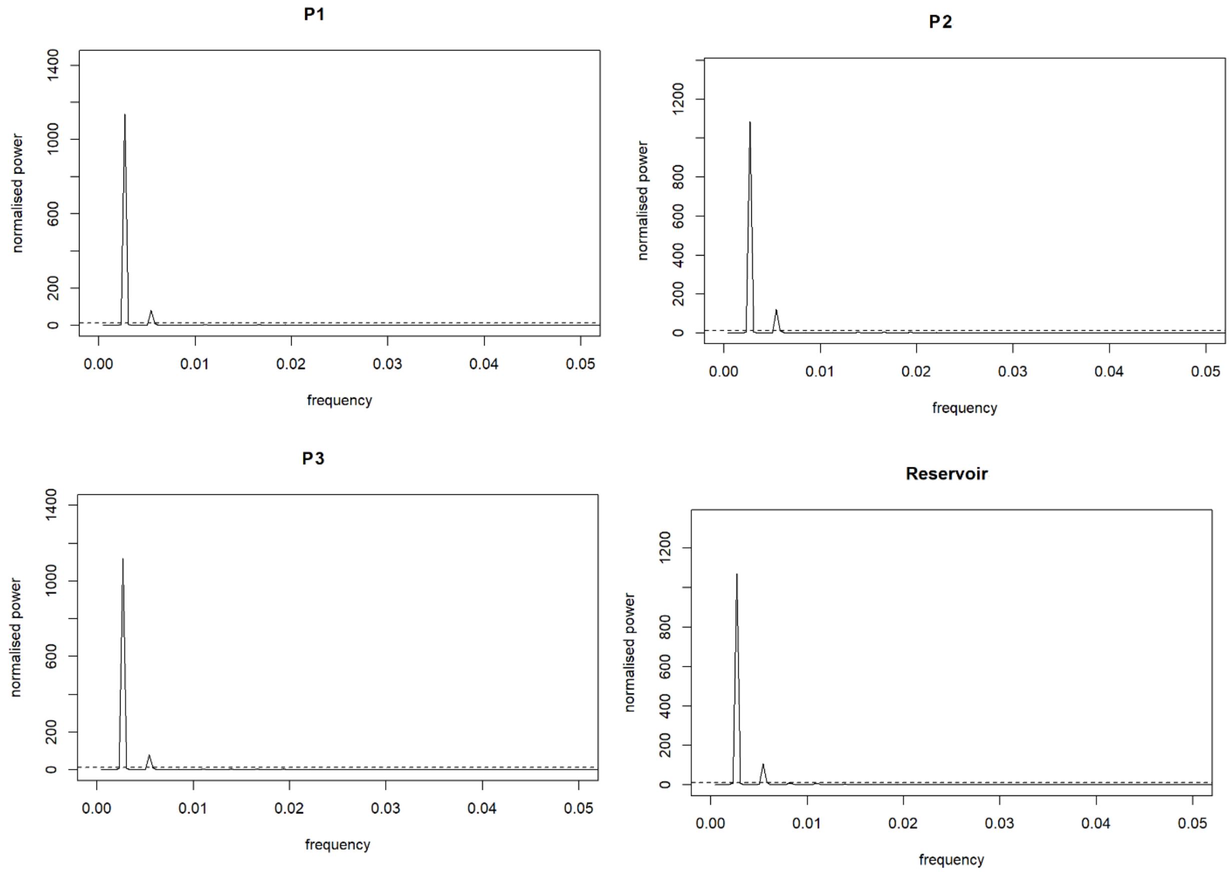

Figure 51. Periodograms of the seasonal components.

Applying the Lomb-Scargle algorithm to the seasonal component obtained from the STL decomposition yields the periodograms seen above in Figure 51. Two dominant seasonal signals can be seen in all data sets. The most dominant is at a period of approximately 1 year. The second much less powerful but still noticeable signal comes from a period of approximately half a year.

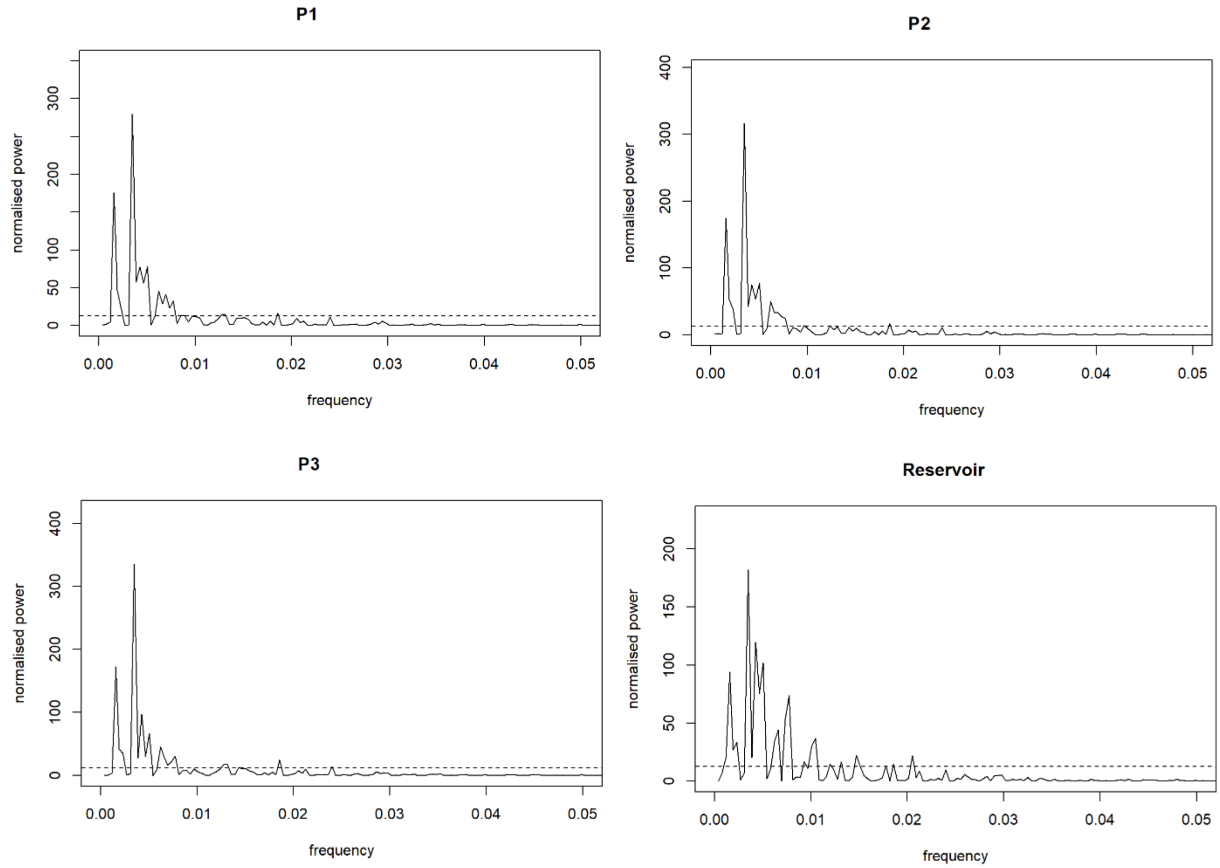

Figure 52. Periodograms of the remainder components.

The periodograms for the remainder components of the STL decomposition are shown above in Figure 52. The data sets all have multiple significant periods. The data sets share a maximum peak at 287 days, approximately ¾ of a year. The Piezometers data sets share a peak with the second highest strength of 646 days, while the reservoir's second strongest signal occurs at 235 days. A summary of the periodogram peaks is shown below in Table 12.

Table 12. Spectral analysis summary.

	P1		P2		P3		Reservoir	
	Spectral Density	**Period (days)**	**Spectral Density**	**Period (days)**	**Spectral Density**	**Period (days)**	**Spectral Density**	**Period (days)**
Raw Data	869.1	369.4	766.2	369.4	875.4	369.4	932.5	369.4
	63.6	648.5	86.9	648.5	68.2	648.5	90.2	184.7
	54.8	184.7	78.6	184.7	60	184.7	20.8	-
Seasonal Component	1138.5	369.4	1086	369.4	1119.6	369.4	1072.6	369.4
	80.6	184.7	121.9	184.7	80.1	184.7	108.3	184.7
Remainder Component	279.8	287.3	316.4	287.3	335.6	287.3	182.3	287.3
	175.3	646.5	174.5	646.5	172.6	646.5	119.7	235.1
	78.1	198.9	77.6	198.9	97.4	235.1	102	198.9
	77.1	235.1	75	235.1	66.5	198.9	94.4	646.5

Correlation Analysis

Covariance is a quantitative measure of how two different data sets vary together (Ross, 2017). The sign of the covariance indicates the tendency in the linear relationship between the two data sets. The magnitude of the covariance does not yield interpretable results unless normalized.

Covariance:

$$Cov(x,y) = \frac{\sum(y_i - \bar{y})(x_i - \bar{x})}{n}$$

Correlation is the covariance of the two variables, normalized by each variable's variance (Ross, 2017). The correlation measures the strength of the relationship between the two variables and ranges from -1 to 1, representing perfect negative and positive correlation, respectively.

Correlation coefficient

$$p(x,y) = \frac{Cov(x,y)}{\sqrt{Var(x)Var(y)}}$$

The covariance and correlation between data sets were calculated. This was completed for the raw data, the seasonal components, and the remainder components of all data sets. It was not completed on the trend component of the data due to the small influence of the trend component. Results of the correlation are visualized in the figures below. Scatterplots of each pair of numeric variables are drawn on the left part of the figure, the correlation coefficient is displayed on the right, and the data set distribution is available along the diagonal.

As shown by Table 13, the covariance of all relationships is positive, demonstrating that levels fluctuate up and down in unison. A hysteresis effect is identifiable in the raw data's scatterplots in Figure 53 when comparing the piezometers to the reservoir. A much more subtle hysteresis is seen in the scatterplots when comparing the raw piezometer data and arguably might not be present. When reservoir levels directly influence piezometer levels, scatter plots of the data should show a straight line (Jun et al., 2013). Based on factors such as stratigraphy, and the distance between the piezometers and the reservoir, slopes of the scatter plots will vary due to different response times. This is to say that hysteresis in the scatterplots is indicative of a lagged relationship between the data sets.

Correlation coefficients of the raw data are distinctly grouped; correlation is higher when comparing piezometer to piezometer, whereas when comparing piezometer to the reservoir, the correlation is weaker. Inspection of the individual correlation coefficients identifies the importance of proximity. The closer the data sets of interest are, the stronger the correlation. This could also indicate subsurface structure, i.e. the presence of cut-off walls and stratigraphy, and the effectiveness of these as a seepage barrier.

Table 13. Raw data covariance summary.

Covariance	**P1**	**P2**	**P3**	**Reservoir**
PS1301	0.099	-	-	-
PS1302	0.072	0.056	-	-
PS1303	0.159	0.116	0.274	-
Reservoir	0.545	0.357	0.917	3.976

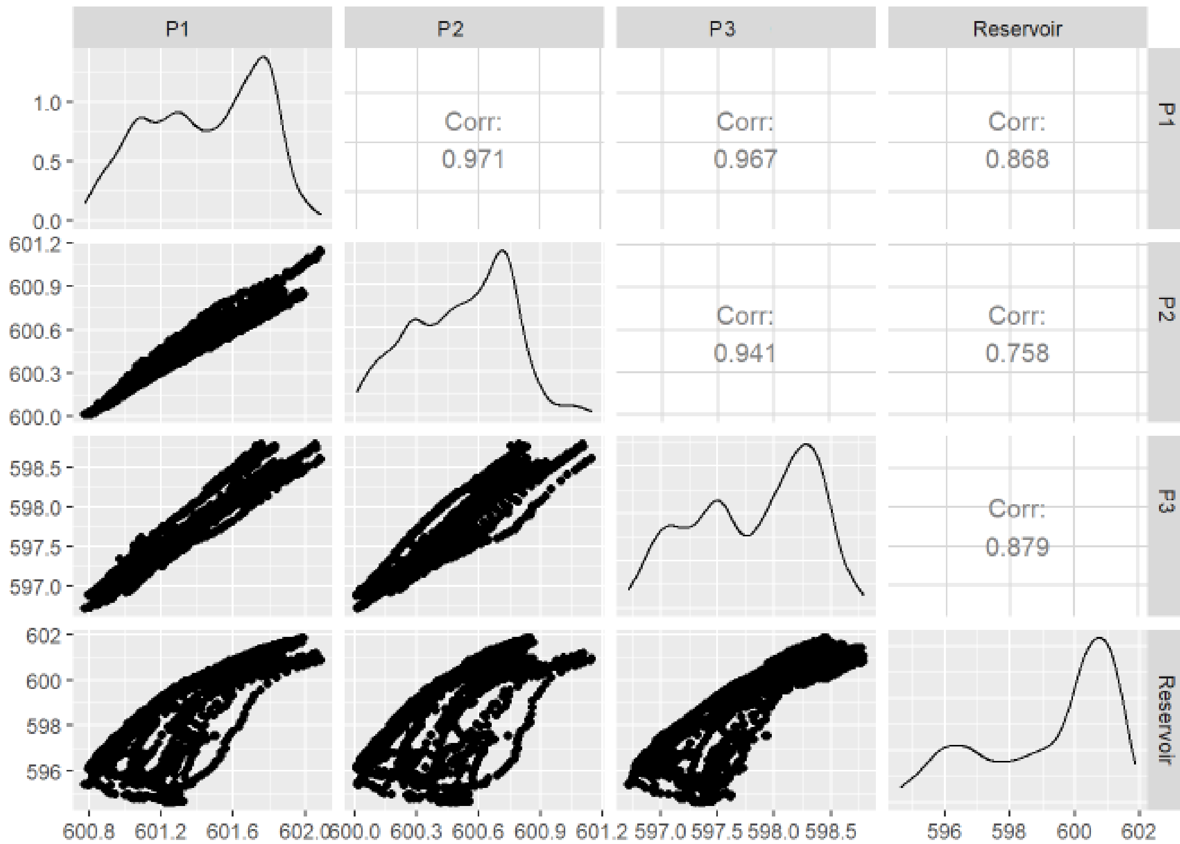

Figure 53. Scatterplots and correlation coefficients of raw data.

For the seasonality component, the covariance of all relationships is positive, showing that levels fluctuate up and down in unison. This is shown in Table 14. The hysteresis effect of all correlations is pronounced when inspecting the seasonal components, as seen in Figure 54. There is a large contrast between the hysteresis of the inter-piezometric correlation and the piezometers-reservoir correlation. This makes sense as the seasonal variance of the reservoir is much stronger. This is likely because of the contrast between surface water's effects on the reservoir level and the piezometer level.

Table 14. Seasonal component covariance summary.

Covariance	**P1**	**P2**	**P3**	**Reservoir**
P1	0.0785	-	-	-
P2	0.0553	0.0410	-	-
P3	0.127	0.0889	0.208	-
Reservoir	0.467	0.297	0.777	3.488

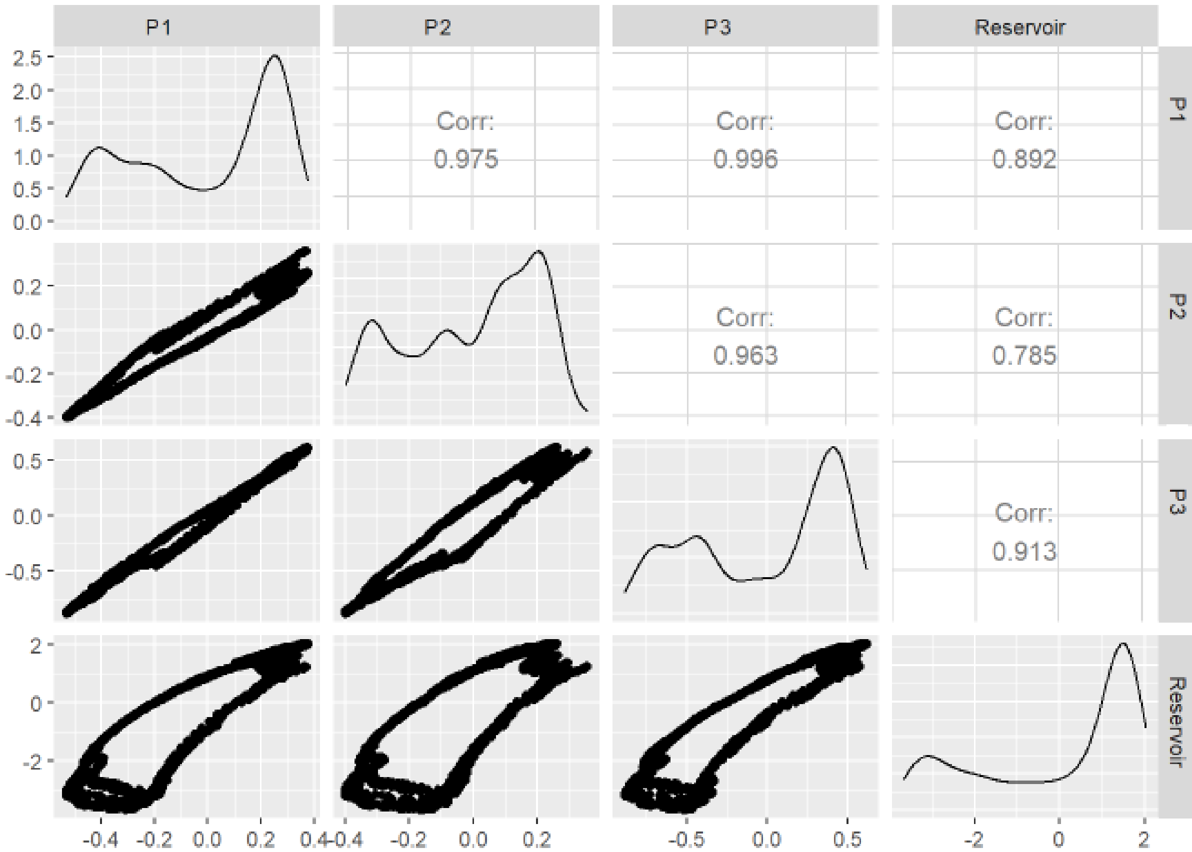

Figure 54. Scatterplots and correlation coefficients of seasonal components.

The covariance of all reminder component relationships is positive, seen in Table 15, showing that levels fluctuate up and down in unison. No hysteresis is evident in the scatterplots of the remainder components of the time series, depicted in Figure 55. There is a distinct difference between the two plot sets. The relationship of the remainder components of the piezometers are all more or less linear with high correlation coefficients. The relationship between the remainder component of the piezometers and reservoir levels is more sporadic, with little to no identifiable pattern.

Table 15. Remainder component covariance summary.

Covariance	**P1**	**P2**	**P3**	**Reservoir**
P1	0.0163	-	-	-
P2	0.0136	0.0118	-	-
P3	0.0263	0.0223	0.0443	-
Reservoir	0.0619	0.0500	0.103	0.339

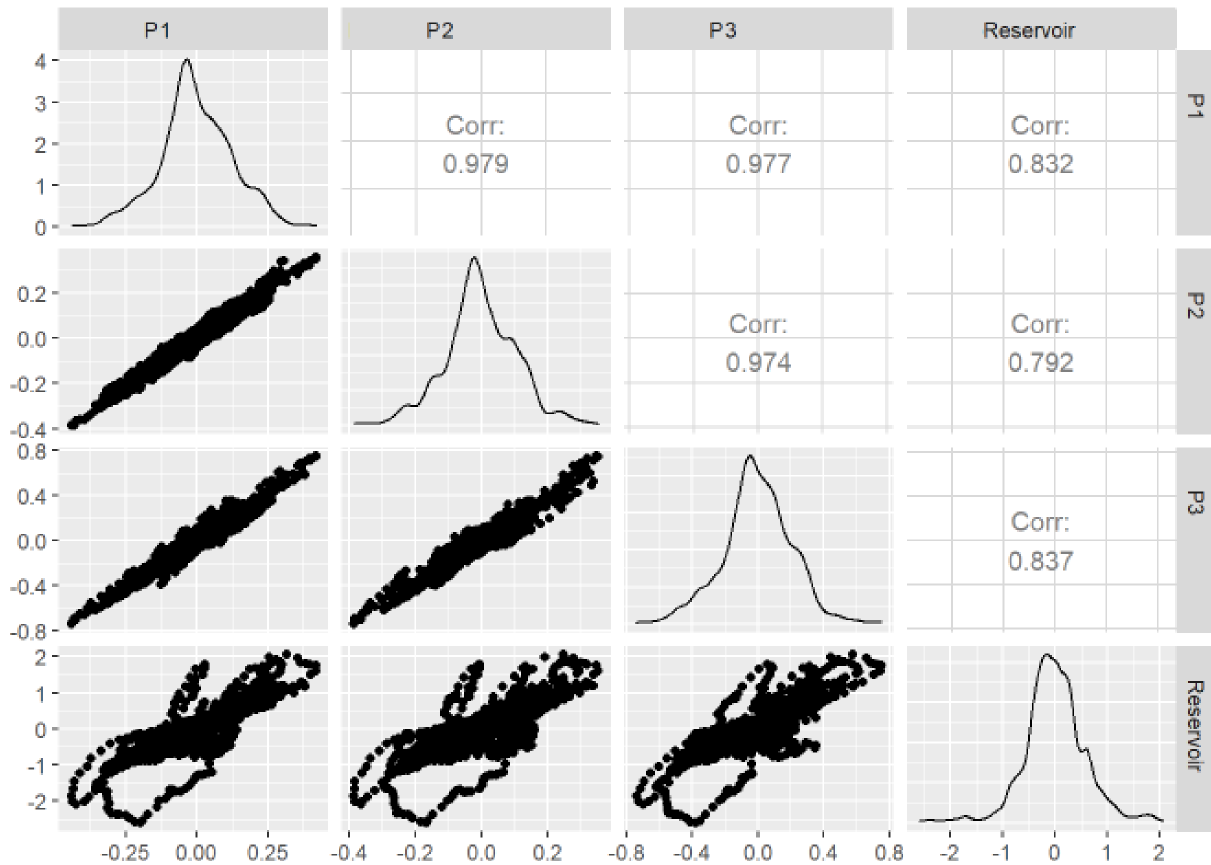

Figure 55. Scatterplots and correlation coefficients of remainder components.

Cross-Correlation Analysis

Another time series analysis method is cross-correlation analysis, where the cross-correlation function is an indicator of the interrelationship between the input time-series and the output time-series (Tan, 2007). When the input stress is random, the cross-correlation function is an impulse response function of the system to the input stress (Padilla and Pulido-Bosch, 1995; Larocque et al., 1998). The studied system is treated as a “black box” where the observed input and output time-series are the only inference on how the system works (Kim et al., 2000).

When the cross-correlation function is asymmetrical and has a maximum or minimum value for a positive lag, the input signal impacts the output signal. The response time is defined as the lag time corresponding to the minimum or maximum values. The slope of the function can characterize an aquifer in terms of infiltration rate, draining capacity, and storage (Chiaudani et al., 2017). The cross-correlation function is calculated in the same way as the correlation function by normalizing and comparing covariances but at lagged values. The cross-correlation function is defined as:

Cross covariance function:

$$g_k^{xy} = \frac{1}{n}\sum_{t=1}^{n-k}(y_t - \bar{y})(x_{t+k} - \bar{x})$$

Cross-correlation function:

$$r_k^{xy} = \frac{g_k^{xy}}{\sqrt{Var(x)Var(y)}}$$

Confidence interval:

$$95\% = -\frac{1}{n} \pm \frac{2}{\sqrt{n}}$$

Application of the cross-correlation function to raw data allows insight into both the causal and non-causal component relationships of input and output variables, as well as their importance (Tam et al., 2004; Chiaudani et al., 2017). When cross-correlation is applied to the remainder components, the function describes the relationship between the random components of the data, giving an idea about the system's response against a unitary impulse. Similar to autocorrelation, cross-correlation is rarely applied to raw groundwater data due to the memory effect of the system and the long time periods needed to see changes exhibited by the system (Lafare, 2016). In some cases of surface hydrology, the cross-correlogram has been used as the unit hydrograph (Tam et al., 2004). Delay of the piezometer response estimates the pressure pulse transfer times (the piezometric level increase due to hydrostatic pressure increase in the aquifer) and of the particle travel times through the aquifer (Panagopoulos and Lambrakis, 2006; Fiorillo and Doglioni, 2010).

Cross-correlation analysis of the raw data, the decomposed seasonal component, and the decomposed remainder component are shown below in Figure 56 and Figure 57. This was completed for the quarter daily data sets rather than the daily data sets. As such, any relationships shorter than 6 hours could not be detected.

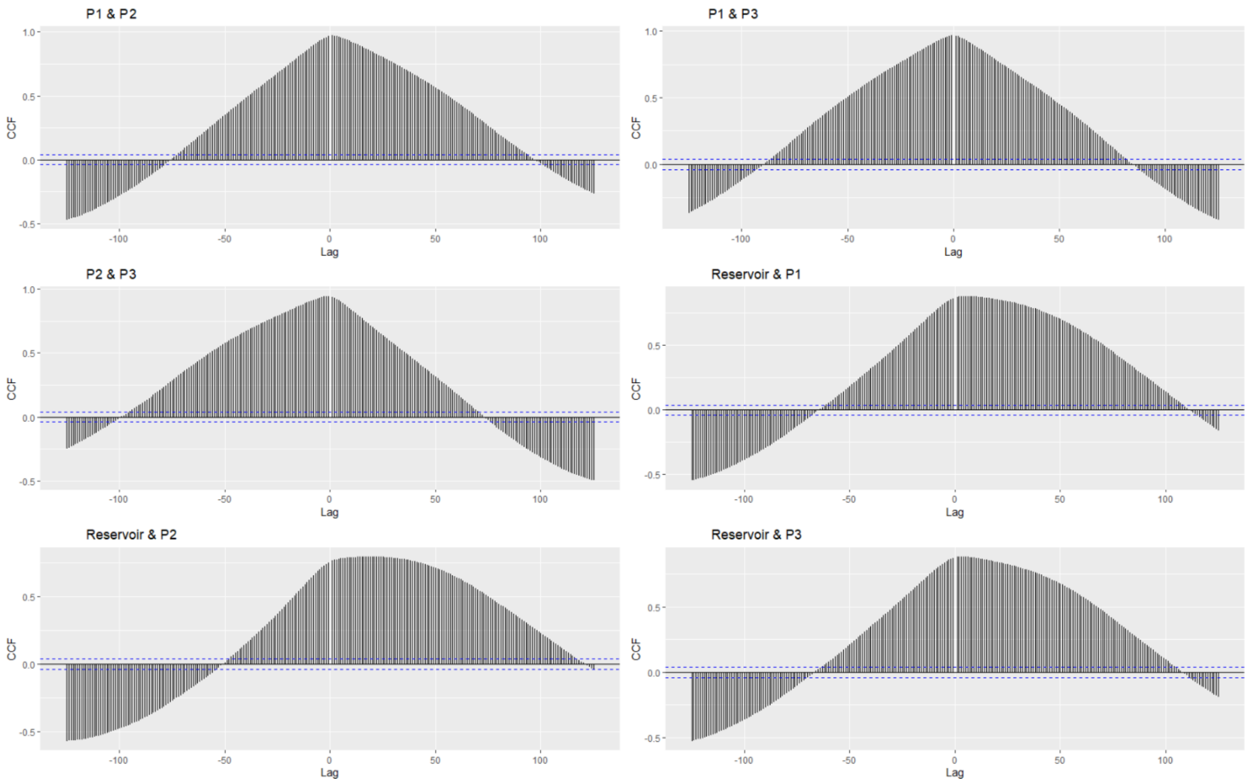

Figure 56. Cross correlation of raw data sets.

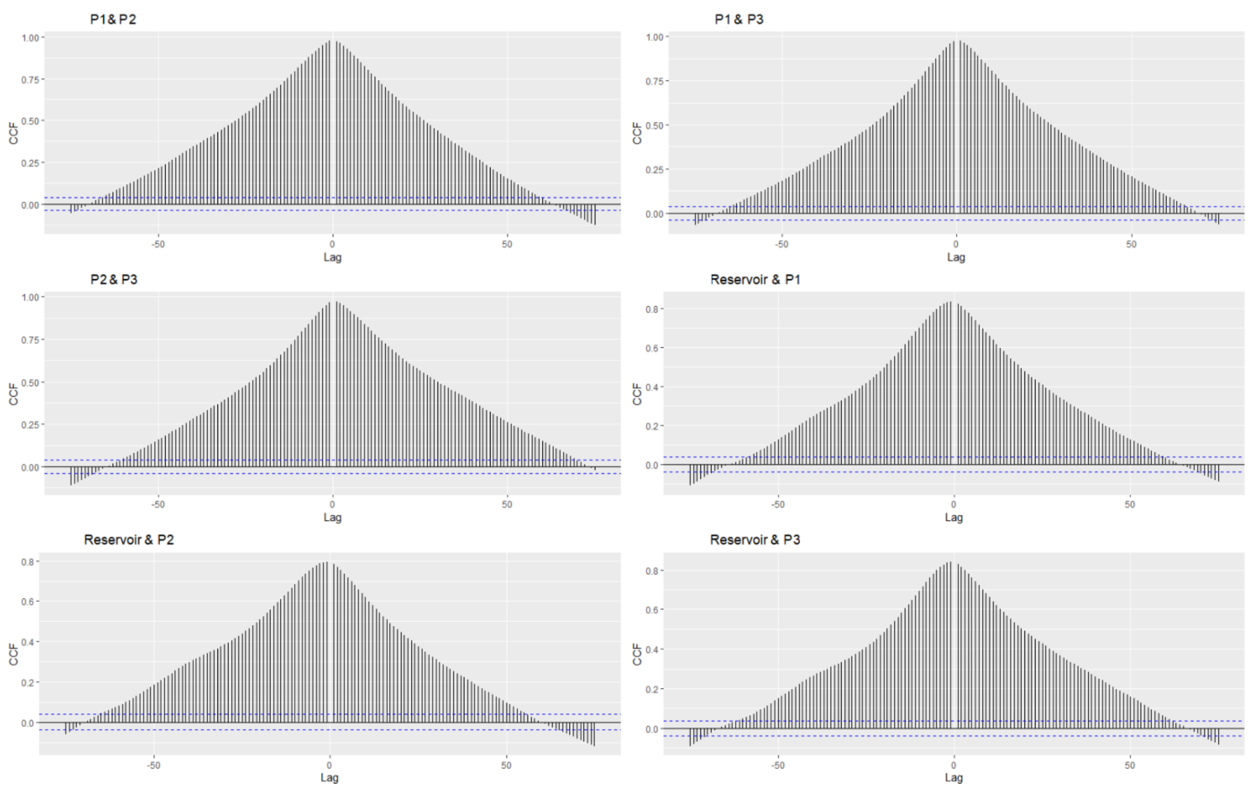

Figure 57. Cross-correlation of remainder components.

The nomenclature for the cross-correlation function is CCF (X, Y), where X is the predictor variable and Y is the response variable. The cross-correlation function estimates the correlation between Y and a time-shifted X, i.e. X_{t+k}. For example, using the raw data sets of the Reservoir and P2, CCF (Reservoir, P2) shows that the peak correlation occurs when the reservoir lags P2 by 20.25 days. This is to say that P2 experiences aquifer impulses 20.25 days ahead of the reservoir. A summary of all the analyzed cross-correlations is shown in Table 16 below.

For the raw data, there is little lag/lead time between piezometers. The correlograms show P1 lagging P2 by 6 hours and P2 leading P3 by 24 hours. P3 and P1 experience no lag between each other. The raw data correlograms show the Reservoir lagging all piezometers. The Reservoir lags P1, P2, and P3 by 5.25, 20.25, and 3.5 days, respectively. The correlation coefficients between all series at the maximum lags are highly significant.

There is less lag/lead time between piezometers than the seasonal and raw data for the remainder components. The correlograms show P1 lagging P2 experiencing no lag/lead of the other. P3 leads both P1 and P2 by 6 hours. The remainder component correlograms show the Reservoir leading all piezometers. The Reservoir leads P1, P2, and P3 by 24, 24, and 18 hours. The correlation coefficients between all series at the maximum lags are highly significant.

Table 16. Cross-correlation summary for the entire data set.

	Raw Data		**Remainder Component**	
Cross Correlation	**Lag (Days)**	**Max Correlation**	**Lag (Days)**	**Max Correlation**
CCF(P1,P2)	0.25	0.97	0.00	0.979
CCF(P1,P3)	0.00	0.967	0.25	0.978
CCF(P2,P3)	-1.00	0.941	0.25	0.974
CCF(Reservoir,P1)	5.25	0.878	-1.00	0.833
CCF(Reservoir,P2)	20.25	0.793	-1.00	0.794
CCF(Reservoir,P3)	3.50	0.884	-0.75	0.839

Correlation of Reservoir Stage to Piezometer Level

Cross-correlation is generally completed over multiyear periods to reveal general inter-relationships between input and output time series (Cai and Ofterdinger, 2016). Delbart et al. (2014) employed a sliding window cross-correlation method to analyze the temporal variability of groundwater-level response to rainfall in a karst aquifer. Kim and Lee (2017) used a similar windowing approach when comparing rainy season rainfall to hillslope pore water pressures. This sliding window method used by these authors successfully established that relationships between intense rainfalls and groundwater levels are highly variable, even at short time scales (Duvert et al., 2015).

Cross-correlation was completed on the raw data and the remainder component of the decomposed data for periods limited to the reservoir's rising and falling hydrograph limbs. It was found that for the raw data, during the rising limb of the hydrograph, the lag-to-peak correlation is 0 for all years and all data sets. All data sets are largely correlated during these periods, with correlation coefficients at peak lags being high, generally ranging from 0.88 to 0.99.

The raw data correlation to the falling hydrograph limbs provided mixed results. Lag times to peak correlations between piezometers was 0 for all years. This was also true of Reservoir-Piezometer correlations for the years 2015, 2016, and 2018. In 2017 the reservoir lagged all of the piezometers, trailing behind P1, P2, and P3 by 5.75, 10.75, and 10.25 days, respectively. In 2019 the reservoir lagged P1 and P2 by 2 and 7.5 days, but did not lag or lead P3. In 2013 the Reservoir did not lag or lead P1 but lagged P2 and P3 by 11.25 and 1.25 days. The correlation coefficients for lags during these periods were generally high, approximately within the range of 0.88 to 0.99.

The cross-correlation results of the 2014 reservoir hydrograph's falling limb provide puzzling results. There is no lag between piezometer data sets, although correlation coefficients are lower than that of other years, being in the range of 0.6 to 0.8. There is no identifiable lag between the Reservoir and P1 and P3. While this is not strange compared to other years, the correlation coefficients are again low, being 0.50 and 0.72, respectively. The relationship between the Reservoir and P2 is the puzzling part. There is no significant correlation between the two at a lag of 0, and at positive and negative lags, the correlation becomes negative. What makes this especially confusing is the strength of the correlation between P2 and the other piezometers and the strength of the correlation between the other piezometers and the reservoir.

The remainder components provided more straightforward and explainable results. There was no lag associated with maximum correlations for inter-piezometer relationships for both the rising and falling limbs of the reservoir hydrograph. For all years, during both rising and falling reservoir periods, the reservoir leads the piezometers. This lead time ranged from 6 hours to 24 hours, depending on the year. The exception to this was the rising limb for 2013; there was no lag associated between the reservoir and piezometer maximum correlation. The correlation values for the inter piezometer relationships ranged from 0.81-0.99, and the values for the reservoir/piezometer relationships ranged from 0.81-0.96.

Additionally, this analysis was completed for periods where the reservoir level was below all piezometer levels. This was completed for the raw data sets and the remainder components of the decomposed data.

Over the seven years of data, seven low reservoir periods occur at which the reservoir level is below all piezometric levels, occurring yearly within the data set from 2014 to 2020. For all years, there is no lag between piezometers, and correlations are high, in the 0.87 to 0.99 range. The cross-correlation between the reservoir and piezometers is not as straightforward during these periods. In 2014, 2016, 2018, 2019, and 2020 the reservoir and piezometers are either insignificantly correlated at a lag of zero or are lowly correlated (~0.3) and only a few lags away from being insignificantly correlated (~4-days).

2015 and 2017 reservoir and piezometer levels are significantly correlated for these low periods. In 2015 the reservoir led the piezometers maximum correlation by approximately 4-6 days and had maximum correlation coefficients of 0.84-0.86. In 2017 the reservoir lagged the piezometers by 9-15 days and had maximum correlation coefficients at this point in the range of 0.77 to 0.79.

The remainder data for these periods produced nearly identical results to the rising and falling hydrograph limb periods; nothing useful was gleaned from this analysis.

ARIMA Modelling

While powerful and useful in its own right, the STL decomposition method is often considered rudimentary and an initial step. Many different statistical tools exist for this purpose, with the most commonly used to model hydro-climatological time series being artificial neural networks (ANN's) and autoregressive integrated moving average (ARIMA) models (Choubin et al. 2014; Sigaroodi et al. 2014; Choubin et al. 2016). Choubin and Malekian (2017) demonstrated that ARIMA models performed better than ANN models. These findings are in agreement with those of Narayanan et al. (2013). As such, an ARIMA model was chosen to further model the piezometer and reservoir data sets.

The use of ARIMA modelling, also known as Box-Jenkins models (Box and Jenkins, 1976), has been used with great success in the hydrological field. They have seen forecasting streamflow applications (Karamouz and Zahraie, 2004) and monthly temperature, humidity and precipitation (Jahanbakhsh and Babapour Basseri, 2003; Shamsnia et al., 2011). Lee et al. (2009), Lu et al. (2013), and Aflatooni and Mardaneh (2011) have all successfully demonstrated the performance of ARIMA modelling to forecast groundwater levels.

ARIMA is a generalization of the simpler Autoregressive Moving Average (ARMA) and adds the notion of integration to remove non-stationarity. An ARIMA model is a linear regression model comprised of a combination of the two different linear models, an autoregression (AR) model and a moving average (MA) model, and an integration component (I). The autoregressive component uses the dependent relationship between current and previous observations, the integration component uses differencing of the raw observation to make the time series stationary, and the moving average component uses the dependency between an observation and a residual error applied to lagged observations.

Arima models are expressed as ARIMA (p,d,q), where p, d, and q represent the number of autoregressive, integrated, and moving average terms, respectively. The AR term p is the number of lag observations included in the model, the I term d is the number of times the raw data was differenced to achieve stationarity, and the MA term q is the size of the moving average window. A value of 0 can be used for any of the ARIMA parameters, indicating that that parameter was not used.

Differencing is typically limited to d values of 1 or 2. As such, a general ARIMA (p,1,q) model is depicted below :

$$Y_t - Y_{t-1} = \emptyset_1(Y_{t-1} - Y_{t-2}) + \emptyset_2(Y_{t-2} - Y_{t-3}) + \cdots + \emptyset_p\left(Y_{t-p} - Y_{t-p-1}\right) + e_t - \theta_1 e_{t-1} - \theta_2 e_{t-2} - \cdots - \theta_q e_{t-q}$$

where Y_t are observed values at time t, $\emptyset_n$ are regression constants of the autoregression component, θ_1 are regression constants of the moving average component, and e_t is random error.

A requirement to completing an ARIMA model is the need for the data to be nonstationary or be transformed into non-stationary data. Stationarity requires a constant variance, a trend about a mean, and no seasonality. To check the stationarity of the data sets, the Augmented Dickey-Fuller test (ADF) (Dickey and Fuller, 1979) test and the Kwiatkowski-Phillips-Schmidt-Shin

(KPSS) (Kwiatkowski et al., 1992) test were used. The ADF test tests for a unit root's presence commonly referred to as a random walk. The KPSS test checks if a time series is stationary around either a linear trend or a mean. The use of the ADF and KPSS tests allows for determining the number of differencing terms (d) needed for the ARIMA model.

A unit root is a stochastic trend within a time series, meaning that the series' trend can change randomly at any point. It is essential to identify unit roots as they can lead to spurious regressions and other errant behaviour. In time series analysis, a unit root can cause unpredictable results. The ADF test decomposes a fitted autoregressive process into monomials; if any of these monomials have a root of zero, then there is a unit root present (Cryer and Chan, 2008). This test's null hypothesis is that a unit root is present, while the alternate hypothesis is that the series is difference stationary. The results of the augmented dickey fuller test, as seen in Table 17, are that the possibility of a unit root within the data sets can be rejected.

Table 17. Augmented dickey fuller test results.

Data set	**Alternate Hypothesis**	**Dickey-Fuller**	**Lag Order**	**p-value**
P1	Stationary	-3.5466	13	0.0378
P2	Stationary	-3.5818	13	0.0344
P3	Stationary	-3.672	13	0.0257
Reservoir	Stationary	-4.156	13	p<0.01

The KPSS test determines if the series is stationary around a mean or a trend. The test works by creating a linear regression of the series consisting of three components, a random walk, a deterministic trend, and a stationary error. The intercept of the regression is used to determine stationarity (Kwiatkowski et al., 1992). The null hypothesis can be either level (mean) stationarity or stationarity around a trend. The tests' results are that the data sets are neither trend or level stationary with test outputs shown in Table 18. The implication of these results is that differencing is needed to complete an ARIMA model.

Table 18. KPSS test results.

Data set	Null Hypothesis	KPSS	Lag Order	p-value
P1	Level Stationarity	0.1641	9	p>0.1
P2	Level Stationarity	0.1420	9	p>0.1
P3	Level Stationarity	0.9015	9	p<0.01
Reservoir	Level Stationarity	0.1646	9	p>0.1
P1	Trend Stationarity	0.15465	9	0.04279
P2	Trend Stationarity	0.14111	9	0.05906
P3	Trend Stationarity	0.19918	9	0.01631
Reservoir	Trend Stationarity	0.1496	9	0.04697

The testing above is a validation of the lack of stationarity in the data set, but in all reality, it is not entirely needed. All of the data sets violate the seasonality condition of stationarity, which is a common problem in hydrological data. ARIMA models can accommodate seasonality (Nury et al., 2017), with modifications needed to the statistical model depending on the raw data structure, namely the frequency of observations.

Traditionally, in an unautomated process, the AR and MA terms' order would be chosen by examining autocorrelation and partial-autocorrelation plots. This is an unnecessary step, thanks to the R software. The auto.arima function in R uses a variation of the Hyndman-Khandakar algorithm (Hyndman & Khandakar, 2008), combining unit root tests and minimizing the AICc and MLE to obtain an ARIMA model. To create the Fourier coupled model, the Fourier terms of the data set are passed in as an exogenous variable.

The auto.arima function in R does not allow for a long seasonal period, specifically those longer than 350 observations. As the sugar lake data has a yearly seasonality, with 365 observations per year, the seasonal observations exceed this amount. The solution to this is a Fourier coupled model, which has multiple advantages; Fourier terms of different frequencies can be included allowing for multiple seasonal periods, any length of seasonal period can be included, and short-term dynamics are easily handled with an ARIMA error. A disadvantage of this method compared to a seasonal ARIMA model is that the seasonality is assumed to be fixed and not allowed to change over time. In the case of the Sugar Lake data sets, this is not considered an issue. The model is expressed as:

$$y_t = \alpha + \sum_{k=1}^{K} \left[\alpha_k \sin\left(\frac{2\pi kt}{m}\right) + \beta_k \cos\left(\frac{2\pi kt}{m}\right) \right] + N_t$$

Where N_t is the ARIMA process and m is the period of the data set. The value of K is chosen by minimizing the AIC.

The Akaike information criterium (AIC) (Akaike 1974) is an estimator of in-sample prediction error where the general case is

$$AIC = -2Log(L) + 2k$$

where k is the number of parameters in the statistical model and L is the maximized value of the likelihood function for the estimated model. The AIC is, however, a biased estimator, and where there is a large ratio of parameters per data, the bias can be appreciable. A problem with using AIC is that as the realization length increases, an overestimation of the model order occurs (Woodward et al., 2011). This bias can be approximately eliminated by introducing another nonstochastic penalty term (Hurvich and Tsai,1989). This changes to the corrected AIC, denoted as AICc, and is defined as

$$AIC_c = AIC + \frac{2(k+1)(k+2)}{n-k-2}$$

where n is the (effective) sample size, and again k is the total number of parameters. Alternately the Bayesian information criterion (BIC), proposed by Swarz (1978), is commonly used. Simulation studies seem to indicate that BIC performs better in large samples (Bisgaard and Kulahci, 2012). It is defined as

$$BIC = -2Log(L) + kLog(n)$$

Hurvich and Tsai (1989) suggest that the AICc outperforms other model selection criteria, including both the AIC and BIC, when k/n is greater than 10%. Shown below in Figure 58 is the selection process carried out on the PS1301 data set.

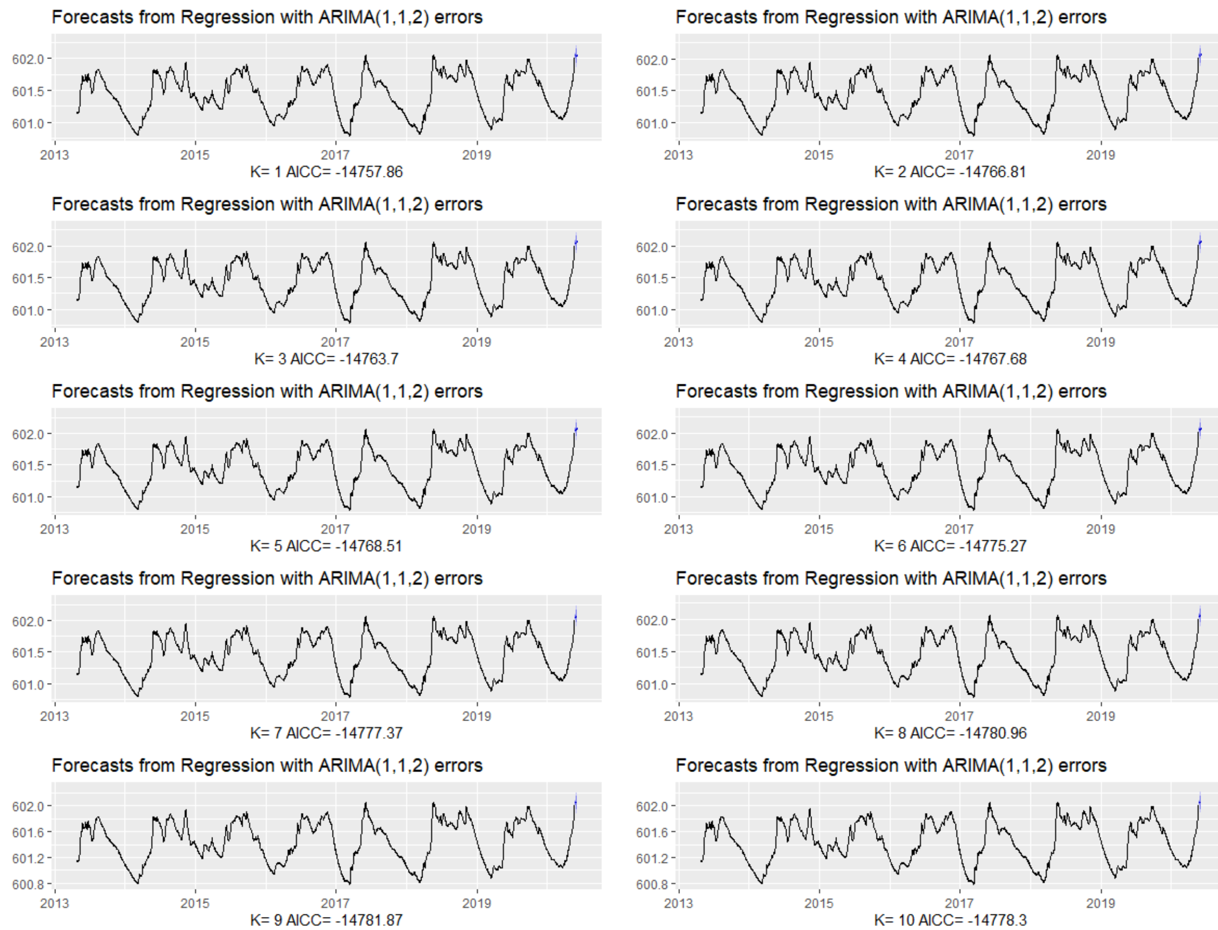

Figure 58. Statistical model selection for P1.

Shown above is the model selection process for the P1 piezometer. The minimized AICc value was found to occur with a k value of 9, i.e., the statistical model best describing the data contains 9 Fourier terms. It can be seen that the ARIMA errors were constant, as an ARIMA (1,1,2) best fist the P1 dynamic component of the statistical model. The AICc values vary little between k values; this is due to the considerable influence of the dominant 365-day seasonal period present within the data. This was the case for all data sets, and all statistical models for the data sets were chosen in the same manner. The AIC, AICc, and BIC were found to be in general agreement for all fitted models. This analysis was completed on the daily data sets to save on computational time. Table 19 below summarizes the results of the model selection.

Table 19. Arima model parameters.

Data set	Arima Parameters (p,d,q)	Fourier k-terms	sigma squared	Log-likelihood	AIC	AICc	BIC
P1	(1,1,2)	9	0.000332	7413.1	-14728.3	-14781.8	-14653.4
P2	(1,1,3)	9	0.000309	7574.9	-15103.7	-15103.3	-14969
P3	(1,1,2)	9	0.000618	6226.8	-12409.5	-12409.1	-12280.7
Reservoir	(2,1,2)	9	0.002025	4453.1	-8860.3	-8859.8	-8725.5

Both the fitted model and the raw data for P1 can be seen below in Figure 59. The raw data set is in blue, and the fitted model is in red. Visually, the model fits well, except for the first term; this is the case for all of the fitted models. This is because the model uses errors from the previous observation to predict the succeeding observation. At time 0, there are no previous observations to aid in forecasting the value at time 1. To validate the goodness of fit, the model residuals must be examined. The residuals of the P1 model are shown in Figure 60.

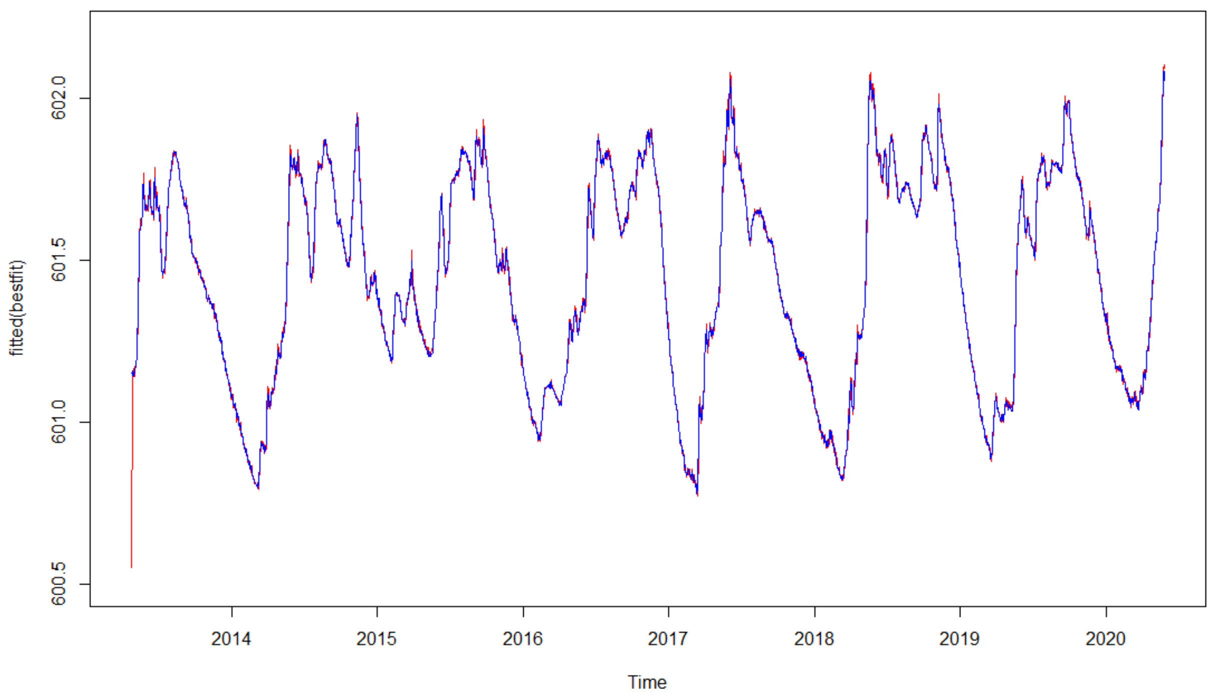

Figure 59. Raw P1 data (blue) overlaid on fitted ARIMA model (red).

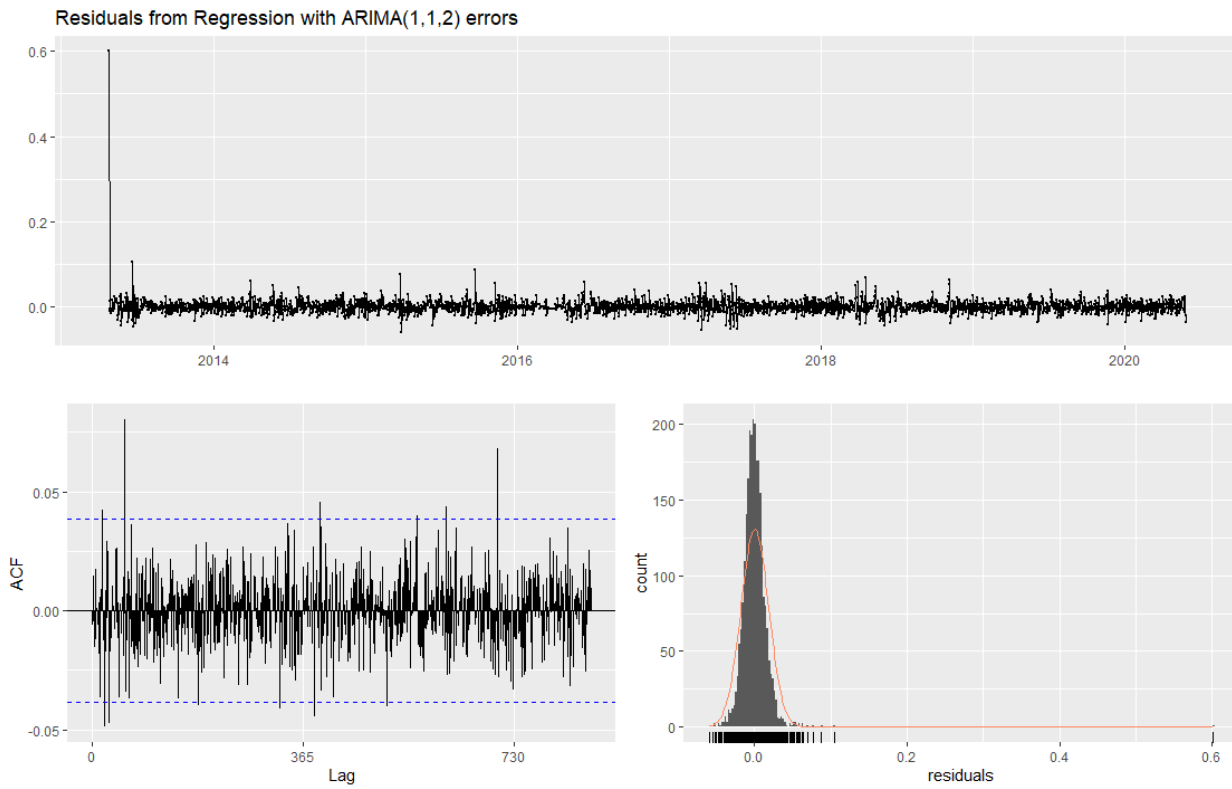

Figure 60. Residuals, ACF of residuals, and residual distribution of P1 ARIMA model.

The residuals of the model show the large error at time 1 more clearly. The residuals of a model are used to evaluate whether a model adequately captured the information within the data set. Residuals should be uncorrelated, have a mean of zero, have a constant variance, and be normally distributed. As seen in Figure 60, the residuals are normally distributed, apart from the one large outlier, have a constant variance, and have a mean of zero. This is the case for all of the fitted models for the Sugar Lake data sets. Visually, the residuals appear to lack any sort of autocorrelation.

To more rigorously confirm the ARIMA modeling's goodness of fit, the Ljung-Box (Ljung and Box, 1978) test was used. The test examines the residuals' autocorrelation by considering a whole set of autocorrelation values as a group rather than individually. The test uses a chi-square distribution table (Cryer and Chan, 2008) to determine significance, and the Ljung-Box statistic, Q, is calculated as

$$Q = n(n+2)\sum_{k=1}^{m}\frac{r_k^2}{n-k}$$

Where n is the time series length, k is the lag number, and r_k is the autocorrelation for lag k. The test's null hypothesis is that the residuals display independence (randomness) in a given time series and are uncorrelated. Results of Jlung-Box testing are shown in Table 20. All fitted models displayed residuals that were not autocorrelated and thus statistically random.

Table 20. Jlung-Box test results.

Data set	**Q**	**Lags (k)**	**p-value**
P1	352.54	517	1
P2	290.72	517	1
P3	414.9	517	0.9966
Reservoir	542.4	517	0.06918

As the ARIMA models were determined to accurately describe the structure of the piezometer and reservoir data, the correlation analysis completed above using the STL decomposition was repeated. Figure 61 shows the correlation coefficients, distribution, and scatterplots of the ARIMA residuals.

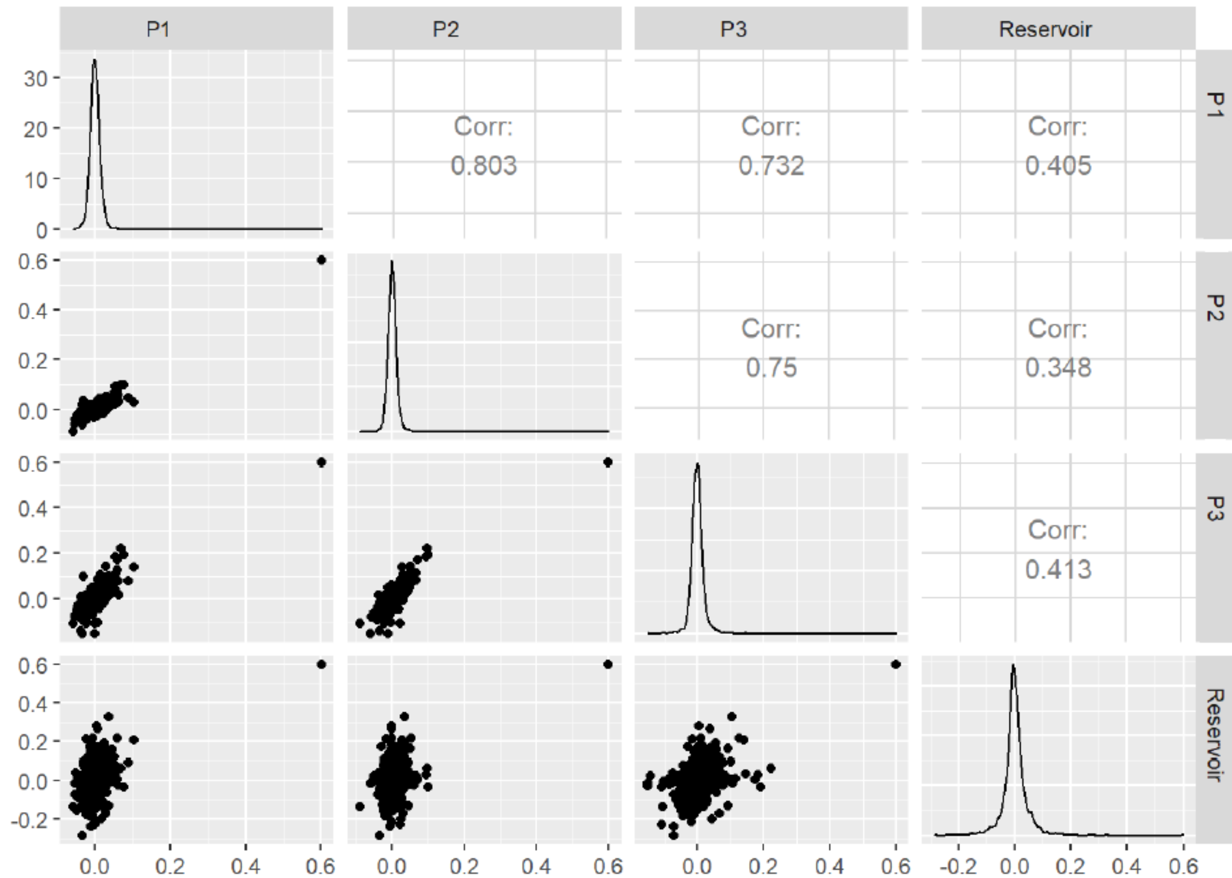

Figure 61. Scatterplots and correlation coefficients of residuals.

The covariance of all relationships is positive, showing that levels fluctuate up and down in unison. Visually, the relationship between the residuals of the data sets is sporadic, with little to no identifiable pattern. There is a distinct grouping of correlation coefficients, with the inter-piezometer correlations being stronger than that of the reservoir-piezometer correlations. This differs from that of the STL remainder correlations, possibly due to the removal of the underlying trend in the ARIMA model that did not occur through the STL method.

Cross-correlation was completed on the residuals of the entire data set. When looking at the data sets as a whole, the data sets are most correlated at a lag of zero.

Cross-correlation was again completed during the rising and falling reservoir hydrograph limbs. The piezometers were most correlated with the rising hydrograph limbs at a lag of zero, with correlation coefficients ranging from 0.65 to 0.89. The exception to this was 2015, where the coefficients ranged from 0.49-0.52 and P1 lead P2 by three days. The reservoir-piezometer correlations during these periods are weaker, generally in the 0.4-0.6 range. In some years, the correlation was not statistically significant. In the cases where the correlation was significant, this almost always occurred at a lag of 0.

The piezometers were most correlated at a lag of zero for the falling limbs, with correlation coefficients ranging from 0.2 to 0.8. Correlation coefficients were generally in the upper end of this spectrum. For the reservoir-piezometer, correlation coefficients ranged from 0.16 to 0.45, with the mean being approximately 0.2. These occurred mostly at a lag of 0 or with the reservoir leading the piezometers by 1 day.

For periods where the reservoir was below all piezometer levels, the piezometers were most correlated at a lag of 0, with coefficients ranging from 0.4-0.85. The correlations between the reservoir and piezometers for these periods were either statistically insignificant or bordering the uncertainty limits.

APPENDIX E - Seepage Modelling

Unsaturated Flow

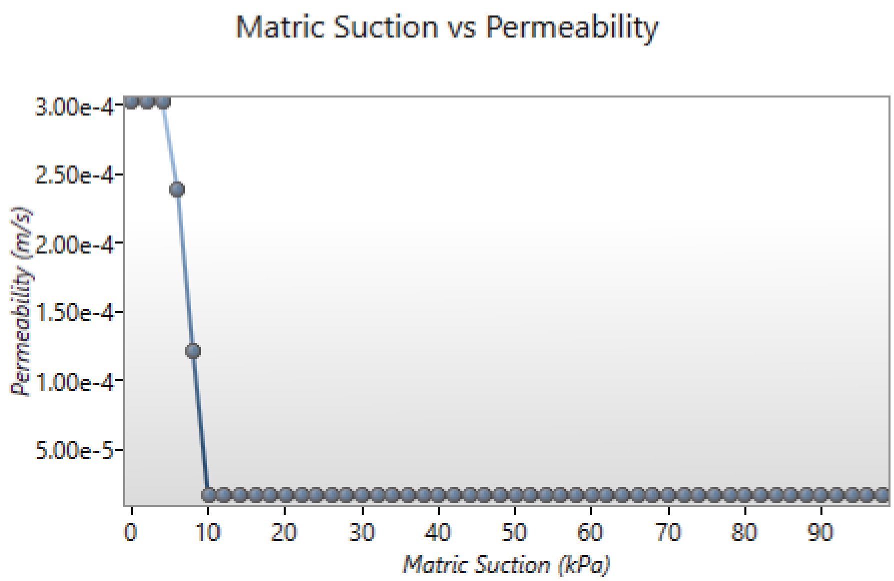

Figure 62. Fill material unsaturated permeability.

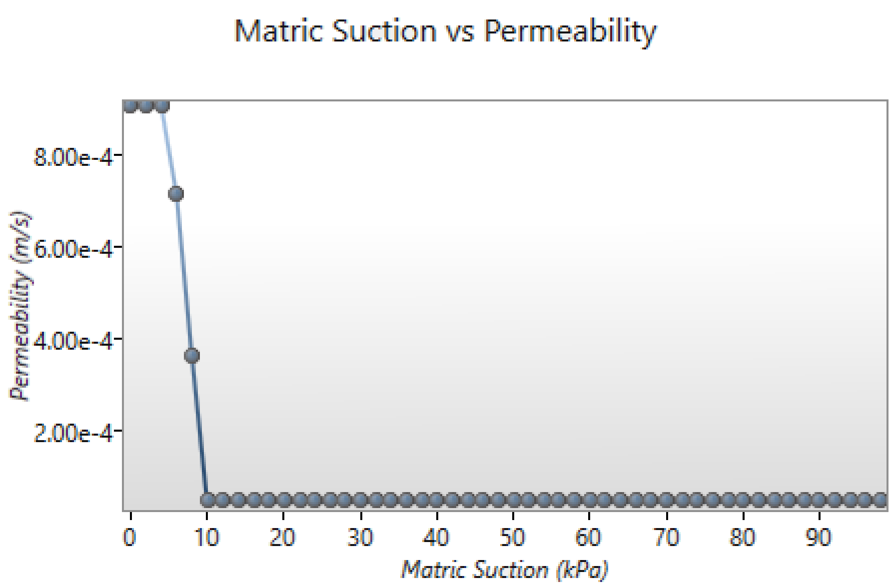

Figure 63. Fluvial material unsaturated permeability.

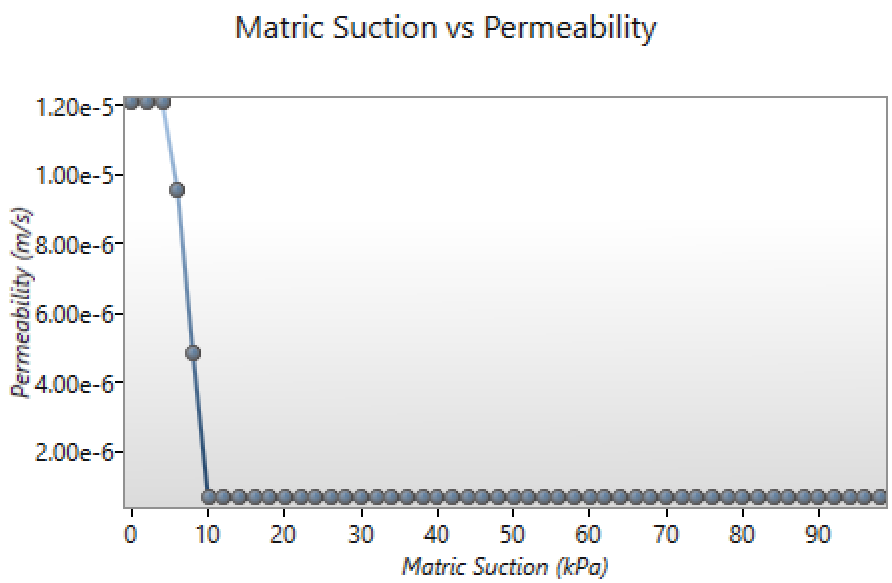

Figure 64. Till material unsaturated permeability.

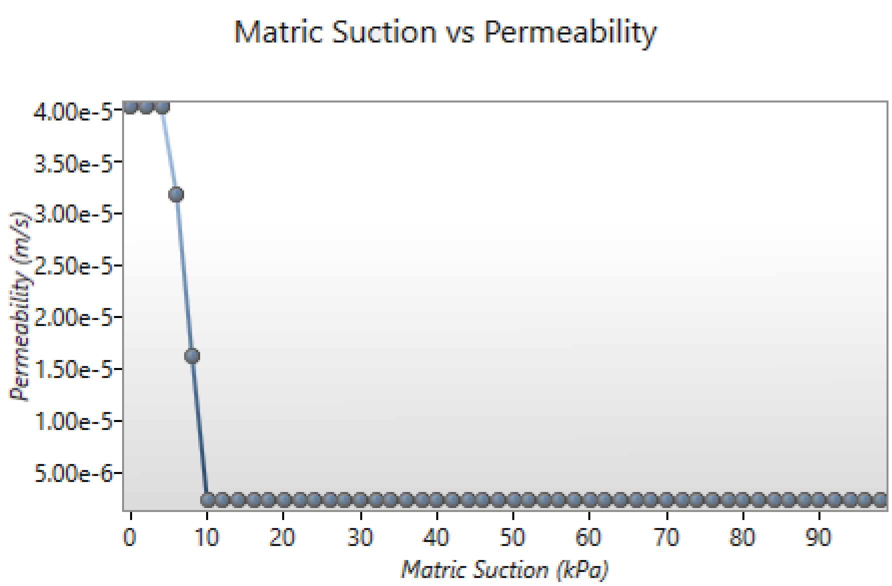

Figure 65. Trench material unsaturated permeability.

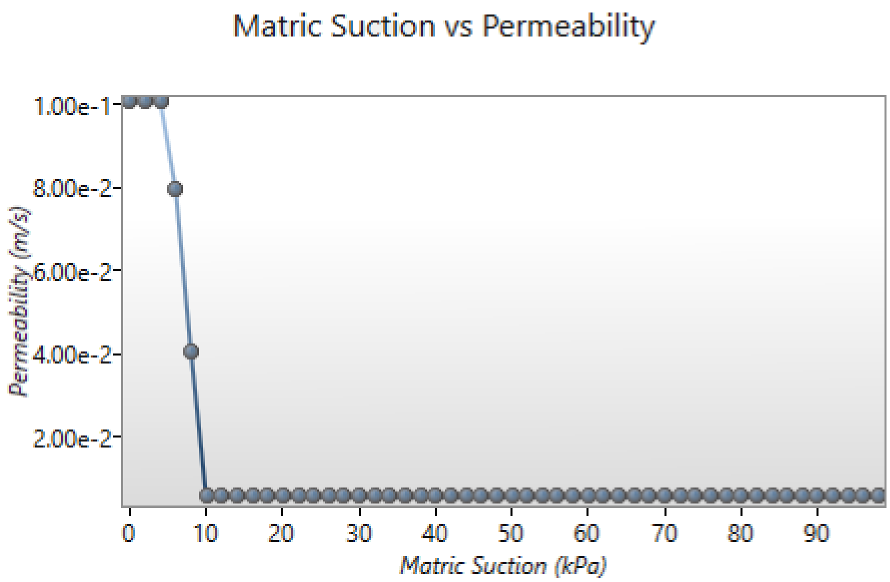

Figure 66. Filter sand material unsaturated permeability.

Calibration Model Results

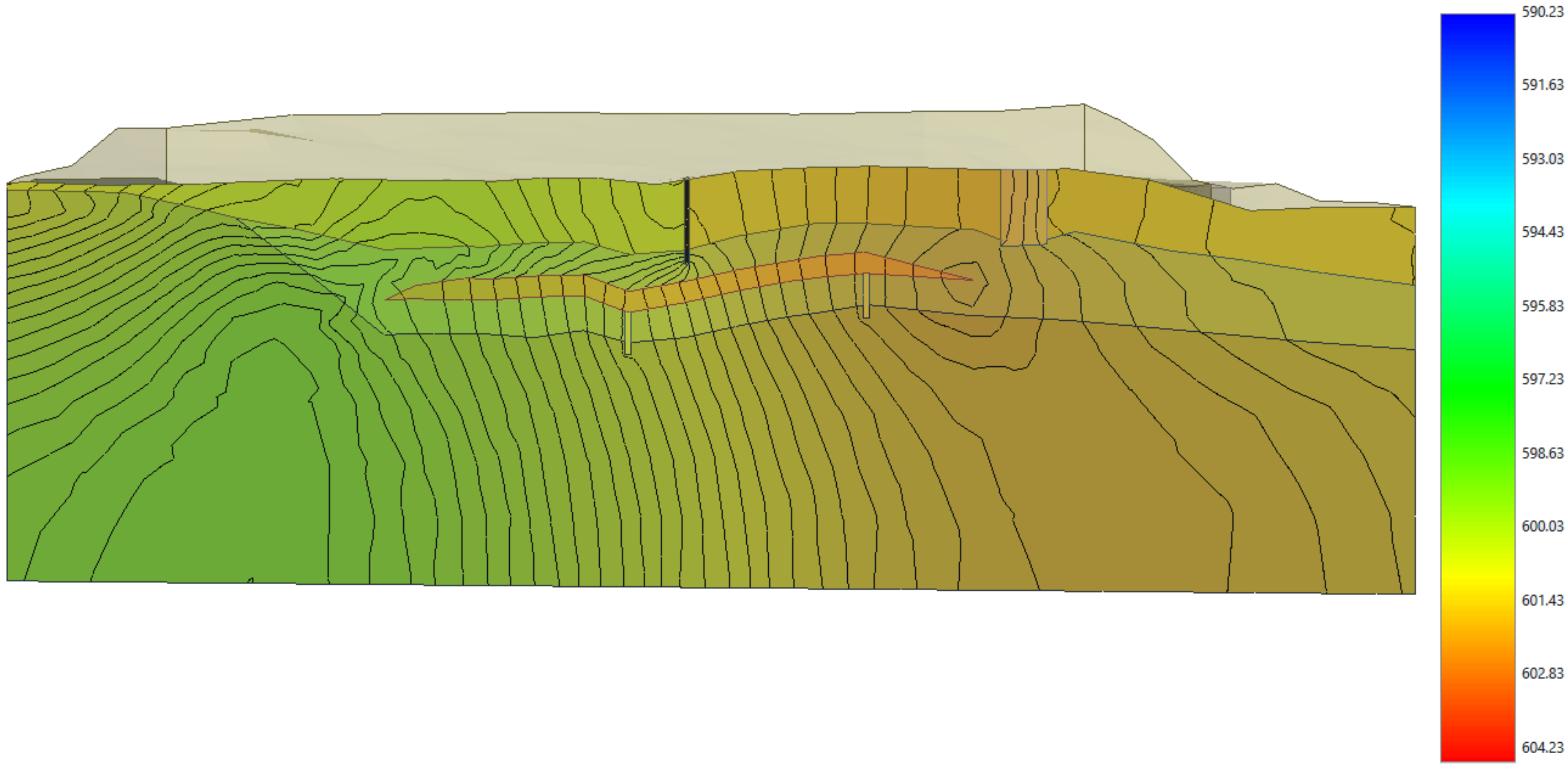

Figure 67. Total head (m) through the P1-P2 cross-section.

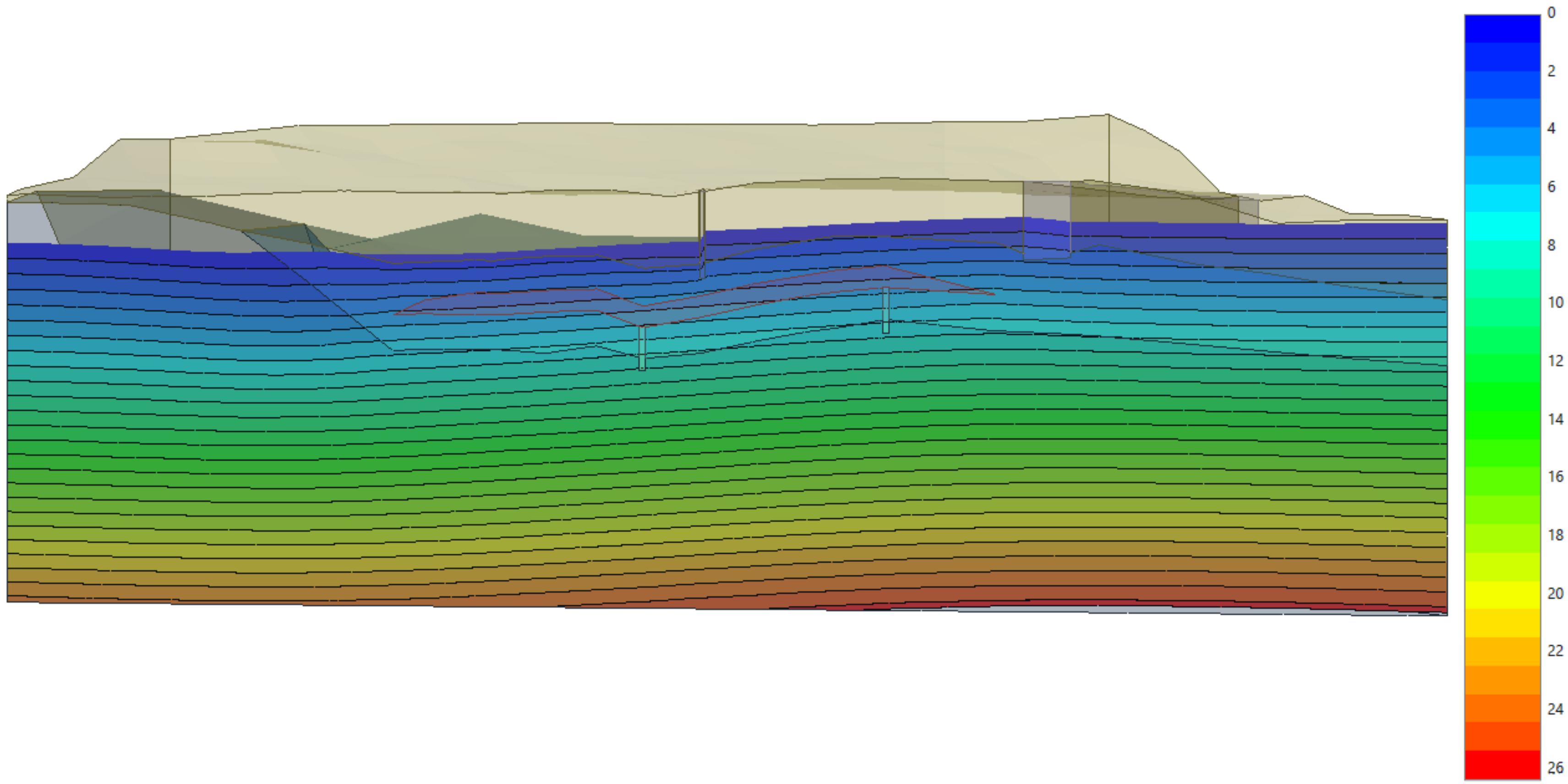

Figure 68. Pressure head (m) through the P1-P2 cross-section.

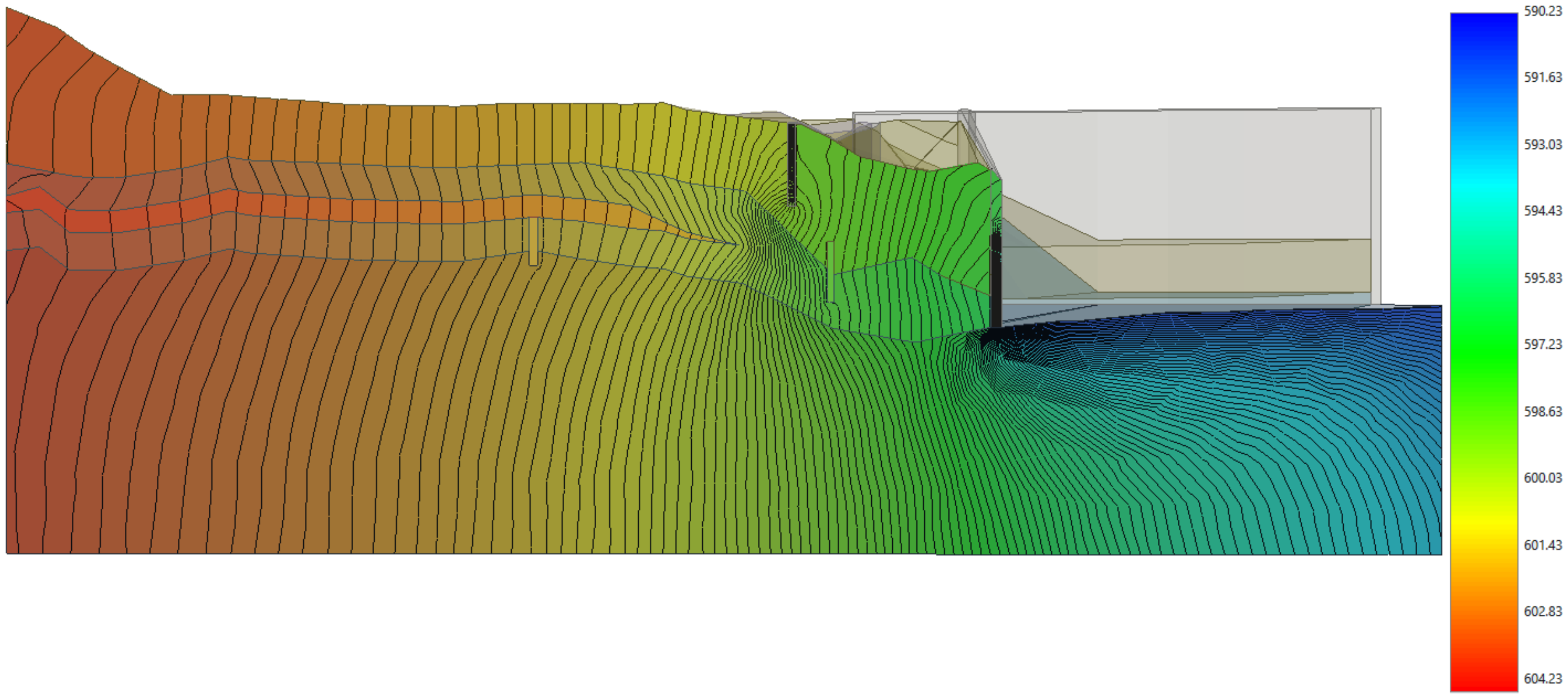

Figure 69. Total head (m) through the P1-P3 cross-section.

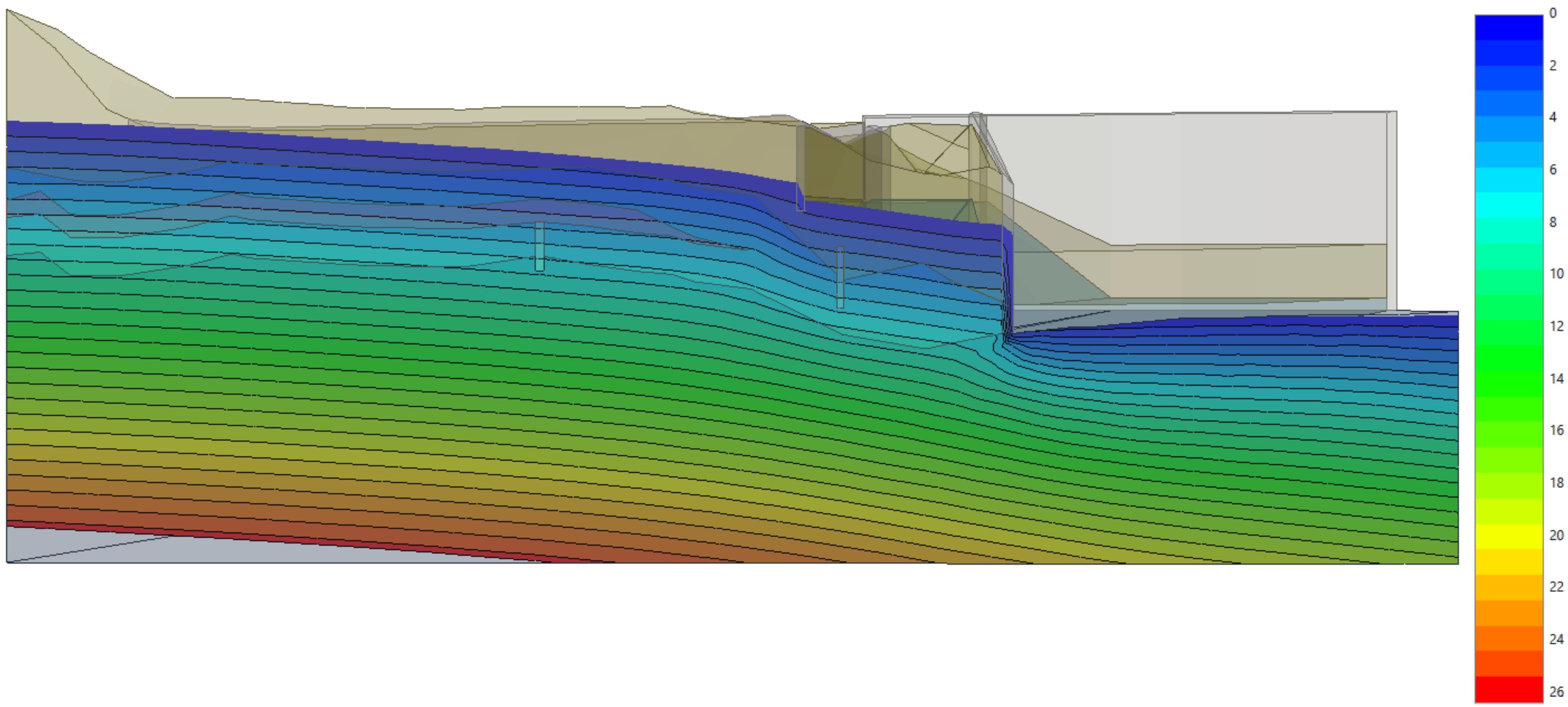

Figure 70. Pressure head (m) through the P1-P3 cross-section.

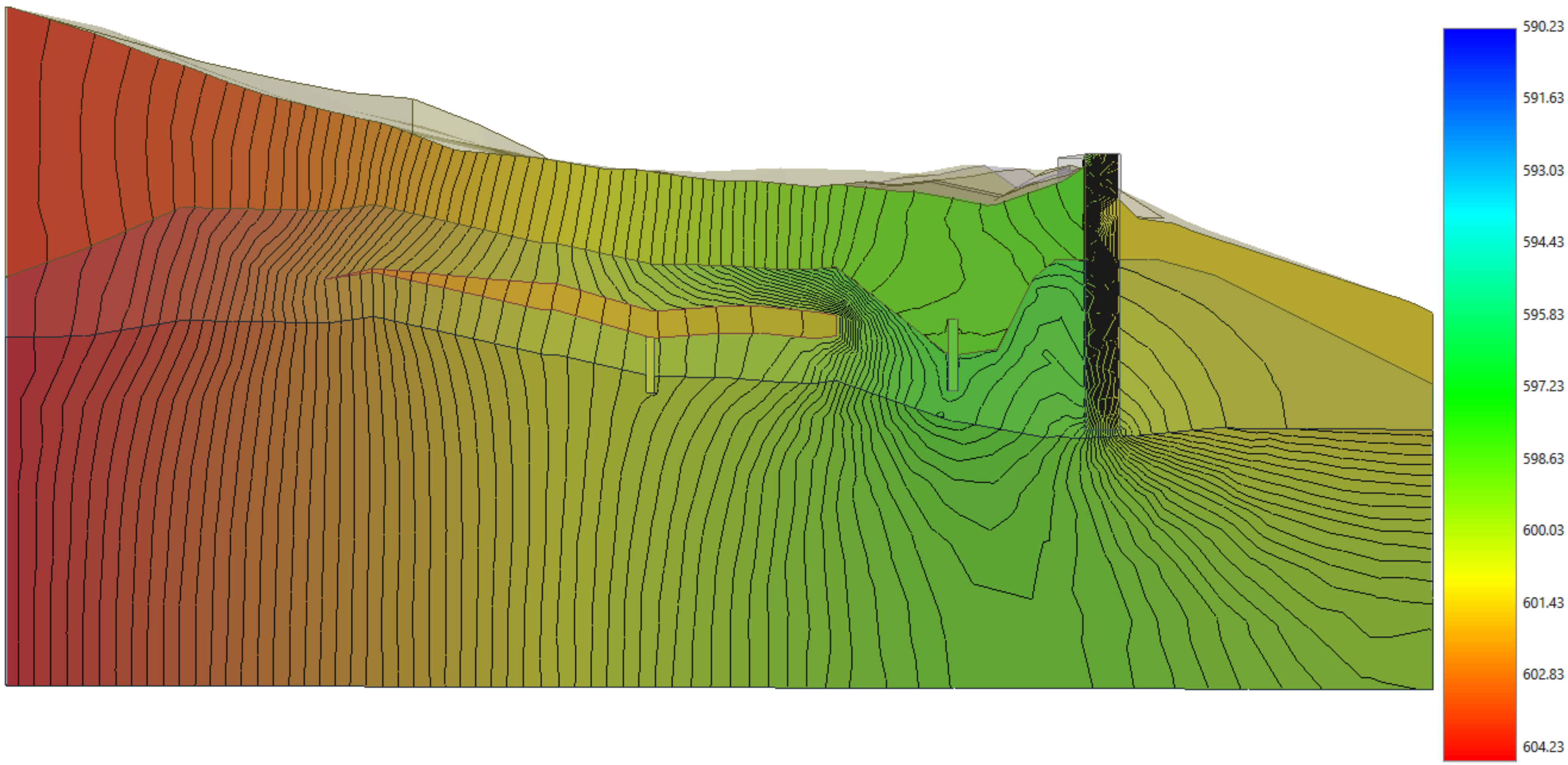

Figure 71. Total head (m) through the P2-P3 cross-section.

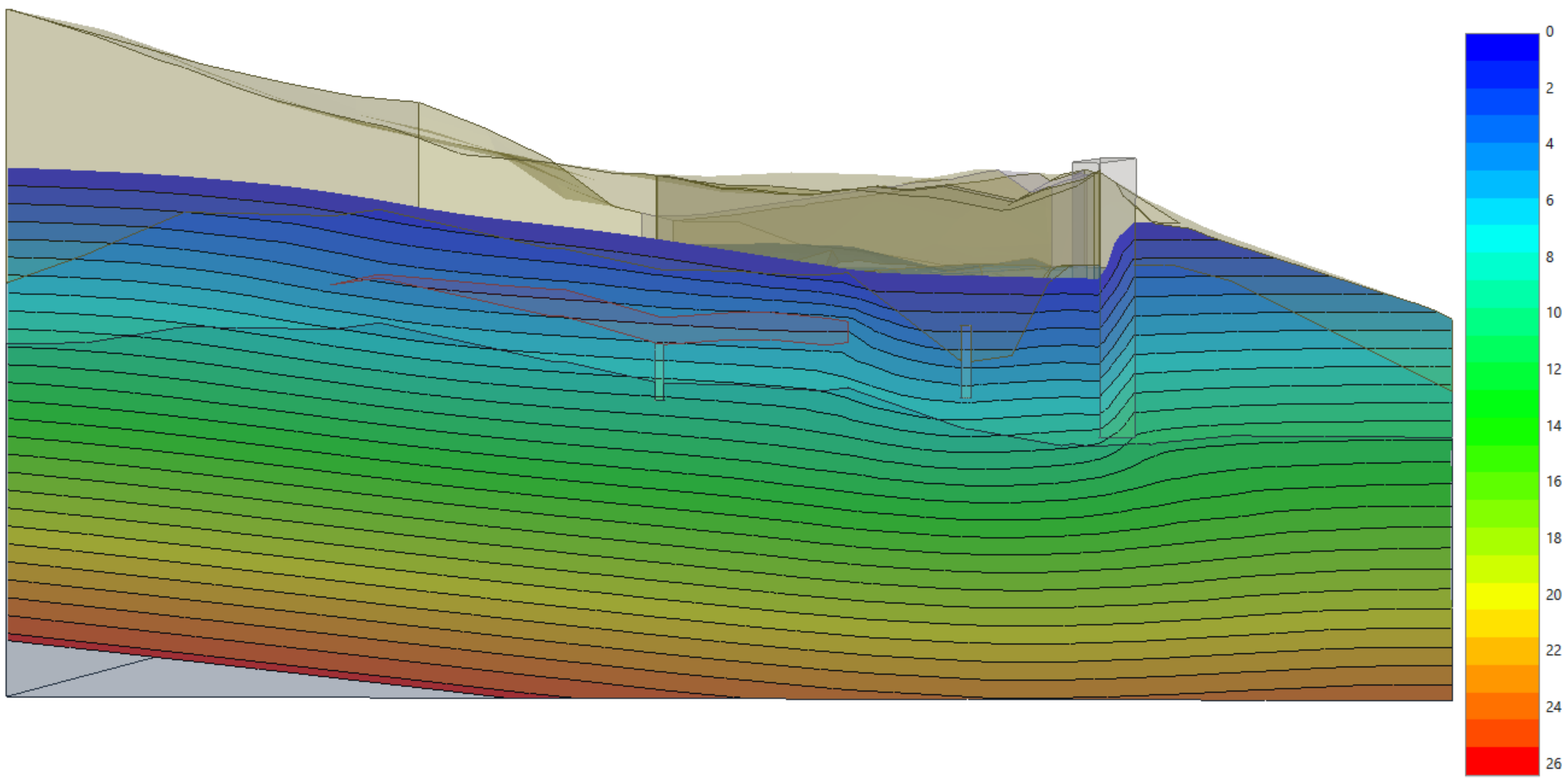

Figure 72. Pressure head (m) through the P2-P3 cross-section.

Sensitivity Analysis Results

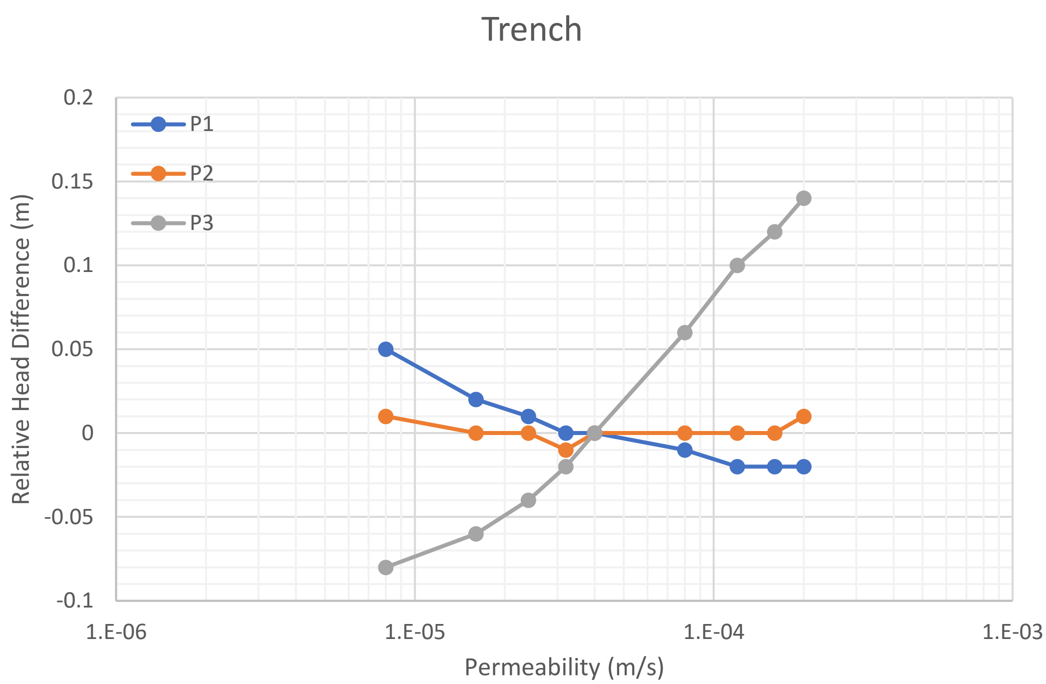

Figure 73. Trench material permeability sensitivity analysis results.

Table 21. Trench material permeability sensitivity analysis results.

Trench Permeability	Model Value			Relative Change		
	P1	P2	P3	P1	P2	P3
8.00E-06	601.93	600.77	598.25	0.05	0.01	-0.08
1.60E-05	601.90	600.76	598.27	0.02	0.00	-0.06
2.40E-05	601.89	600.76	598.29	0.01	0.00	-0.04
3.20E-05	601.88	600.75	598.31	0.00	-0.01	-0.02
4.00E-05	601.88	600.76	598.33	0.00	0.00	0.00
8.00E-05	601.87	600.76	598.39	-0.01	0.00	0.06
1.20E-04	601.86	600.76	598.43	-0.02	0.00	0.10
1.60E-04	601.86	600.76	598.45	-0.02	0.00	0.12
2.00E-04	601.86	600.77	598.47	-0.02	0.01	0.14

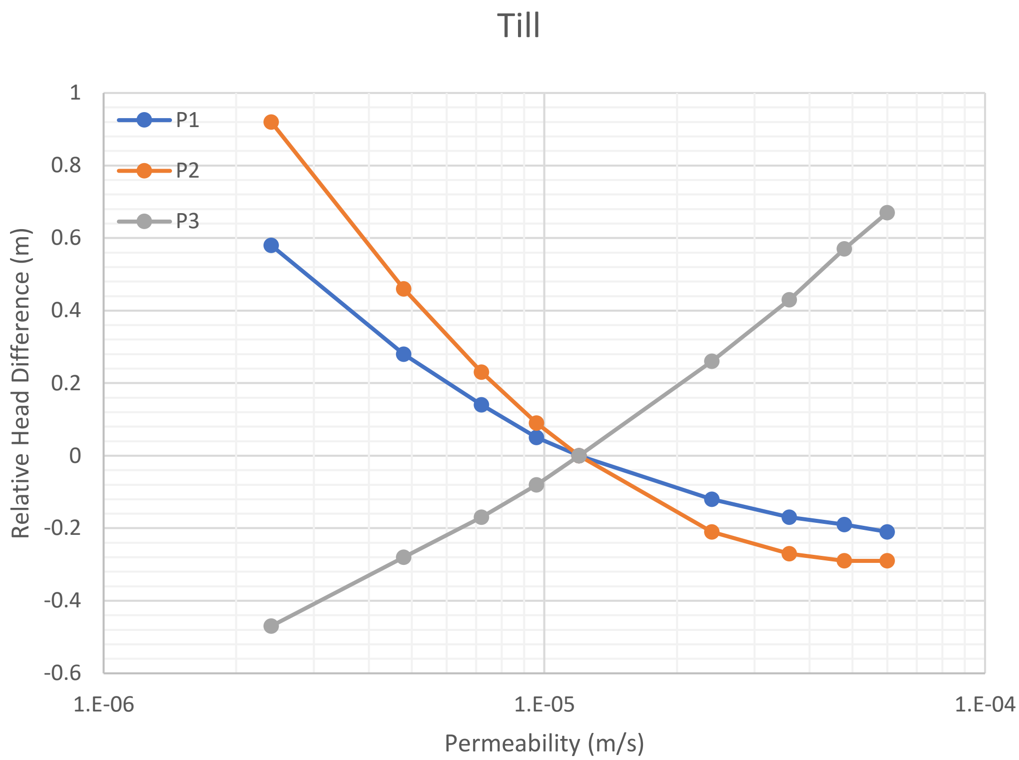

Figure 74. Till material permeability sensitivity analysis results.

Table 22. Till material permeability sensitivity analysis results.

Till Permeability	Model Value			Relative Change		
	P1	P2	P3	P1	P2	P3
2.40E-06	602.46	601.68	597.86	0.58	0.92	-0.47
4.80E-06	602.16	601.22	598.05	0.28	0.46	-0.28
7.20E-06	602.02	600.99	598.16	0.14	0.23	-0.17
9.60E-06	601.93	600.85	598.25	0.05	0.09	-0.08
1.20E-05	601.88	600.76	598.33	0.00	0.00	0.00
2.40E-05	601.76	600.55	598.59	-0.12	-0.21	0.26
3.60E-05	601.71	600.49	598.76	-0.17	-0.27	0.43
4.80E-05	601.69	600.47	598.90	-0.19	-0.29	0.57
6.00E-05	601.67	600.47	599.00	-0.21	-0.29	0.67

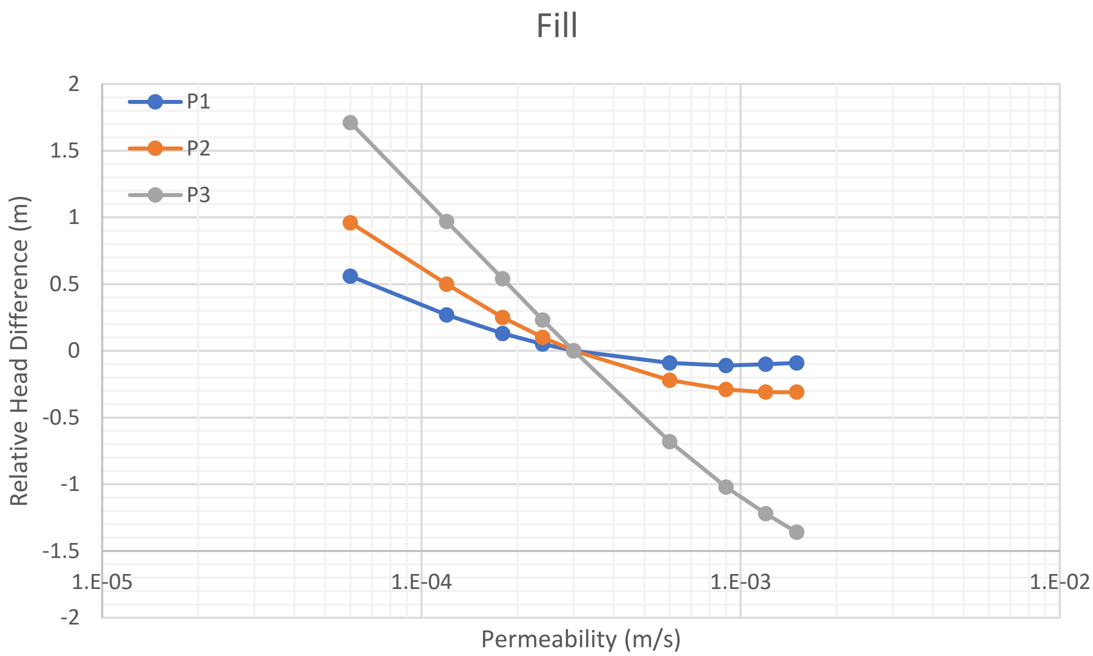

Figure 75. Fill material permeability sensitivity analysis results.

Table 23. Fill material permeability sensitivity analysis results.

Fill Permeability	**Model Value**			**Relative Change**		
	P1	**P2**	**P3**	**P1**	**P2**	**P3**
6.00E-05	602.44	601.72	600.04	0.56	0.96	1.71
1.20E-04	602.15	601.26	599.30	0.27	0.5	0.97
1.80E-04	602.01	601.01	598.87	0.13	0.25	0.54
2.40E-04	601.93	600.86	598.56	0.05	0.10	0.23
3.00E-04	601.88	600.76	598.33	0.00	0.00	0.00
6.00E-04	601.79	600.54	597.65	-0.09	-0.22	-0.68
9.00E-04	601.77	600.47	597.31	-0.11	-0.29	-1.02
1.20E-03	601.78	600.45	597.11	-0.10	-0.31	-1.22
1.50E-03	601.79	600.45	596.97	-0.09	-0.31	-1.36

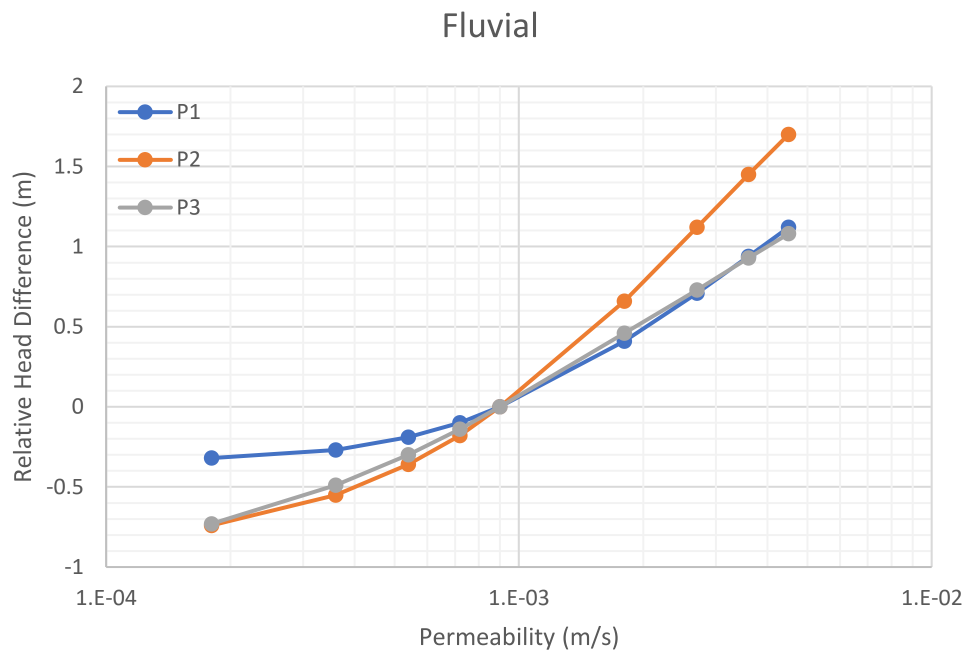

Figure 76. Fluvial material permeability sensitivity analysis results.

Table 24. Fluvial material permeability sensitivity analysis results.

Fluvial Permeability	Model Value			Relative Change		
	P1	P2	P3	P1	P2	P3
1.80E-04	601.56	600.02	597.60	-0.32	-0.74	-0.73
3.60E-04	601.61	600.21	597.84	-0.27	-0.55	-0.49
5.40E-04	601.69	600.4	598.03	-0.19	-0.36	-0.30
7.20E-04	601.78	600.58	598.19	-0.10	-0.18	-0.14
9.00E-04	601.88	600.76	598.33	0.00	0.00	0.00
1.80E-03	602.29	601.42	598.79	0.41	0.66	0.46
2.70E-03	602.59	601.88	599.06	0.71	1.12	0.73
3.60E-03	602.82	602.21	599.26	0.94	1.45	0.93
4.50E-03	603.00	602.46	599.41	1.12	1.70	1.08

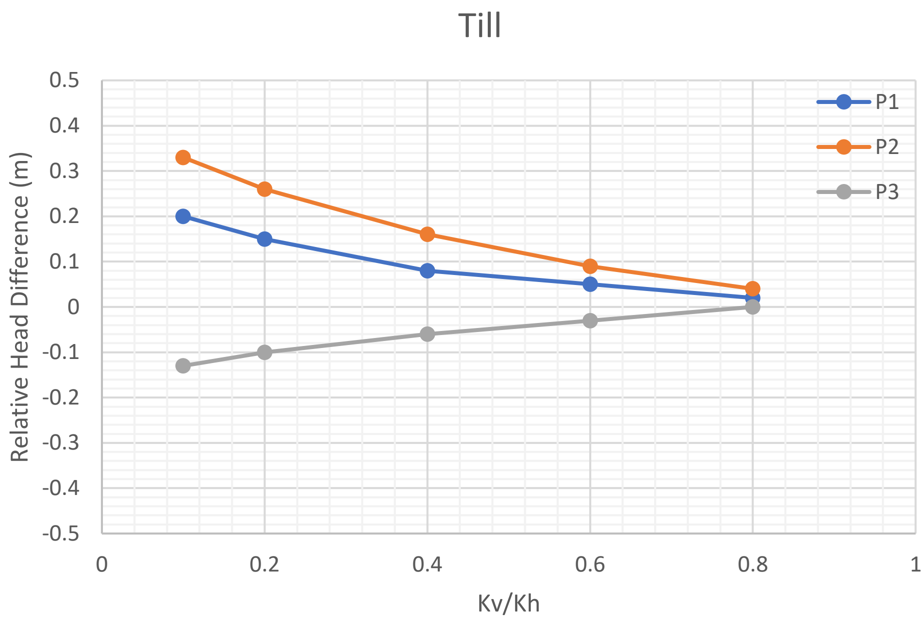

Figure 77. Till material anisotropy sensitivity analysis results.

Table 25. Till material anisotropy sensitivity analysis results.

Till Anisotropy Kv/Kh	Model Value			Relative Change		
	P1	P2	P3	P1	P2	P3
0.8	601.9	600.8	598.33	0.02	0.04	0.00
0.6	601.93	600.85	598.3	0.05	0.09	-0.03
0.4	601.96	600.92	598.27	0.08	0.16	-0.06
0.2	602.03	601.02	598.23	0.15	0.26	-0.10
0.1	602.08	601.09	598.2	0.20	0.33	-0.13

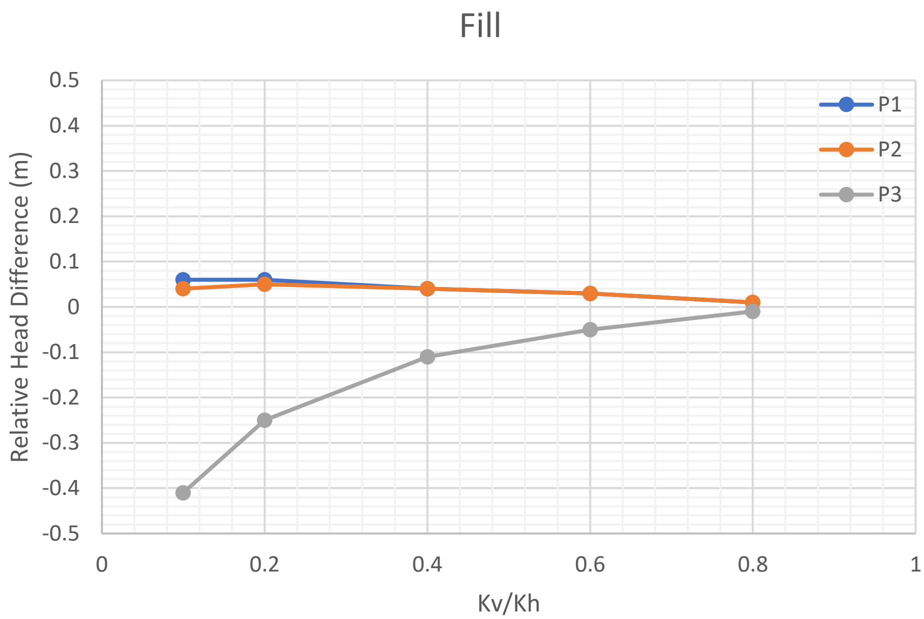

Figure 78. Fill material anisotropy sensitivity analysis results.

Table 26. Fill material anisotropy sensitivity analysis results.

Fill Anisotropy Kv/Kh	Model Value			Relative Change		
	P1	P2	P3	P1	P2	P3
0.8	601.89	600.77	598.32	0.01	0.01	-0.01
0.6	601.91	600.79	598.28	0.03	0.03	-0.05
0.4	601.92	600.8	598.22	0.04	0.04	-0.11
0.2	601.94	600.81	598.08	0.06	0.05	-0.25
0.1	601.94	600.8	597.92	0.06	0.04	-0.41

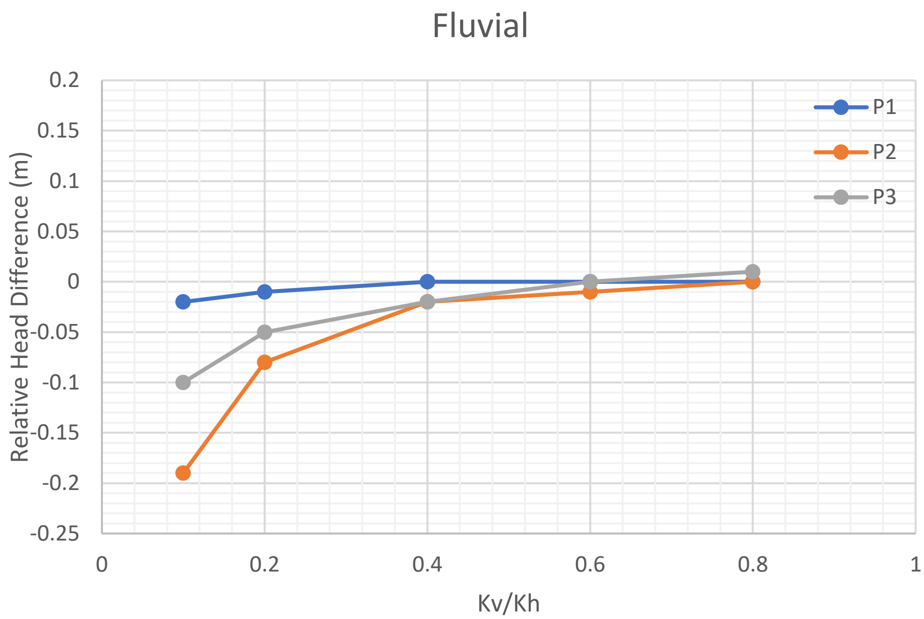

Figure 79. Fluvial material anisotropy sensitivity analysis results.

Table 27. Fluvial material anisotropy sensitivity analysis results.

Fluvial Anisotropy Kv/Kh	Model Value			Relative Change		
	P1	P2	P3	P1	P2	P3
0.8	601.88	600.76	598.34	0.00	0.00	0.01
0.6	601.88	600.75	598.33	0.00	-0.01	0.00
0.4	601.88	600.74	598.31	0.00	-0.02	-0.02
0.2	601.87	600.68	598.28	-0.01	-0.08	-0.05
0.1	601.86	600.57	598.23	-0.02	-0.19	-0.10

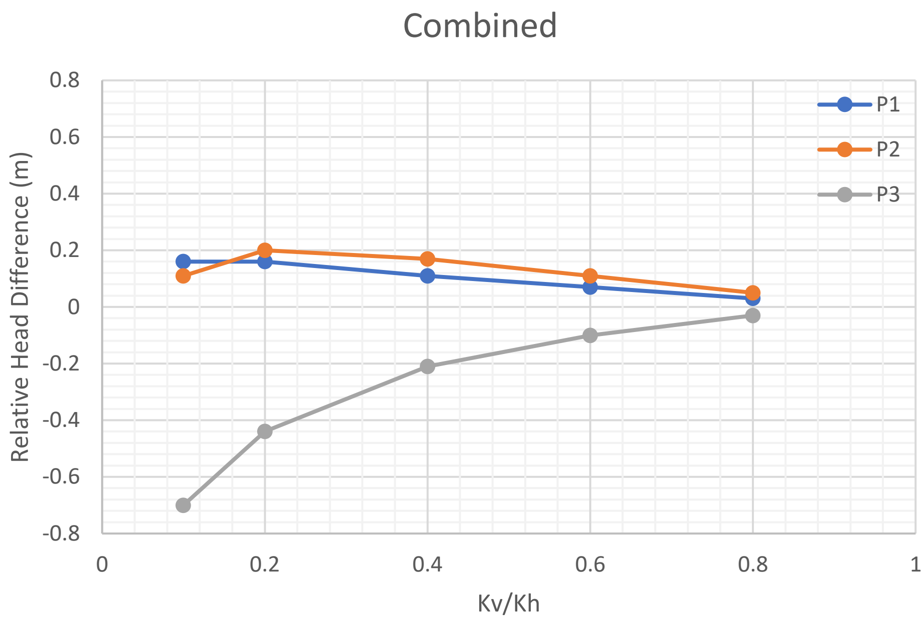

Figure 80. Combined material anisotropy sensitivity analysis results.

Table 28. Combined material anisotropy sensitivity analysis results.

Combined Anisotropy Kv/Kh	**Model Value**			**Relative Change**		
	P1	**P2**	**P3**	**P1**	**P2**	**P3**
0.8	601.91	600.81	598.3	0.03	0.05	-0.03
0.6	601.95	600.87	598.23	0.07	0.11	-0.10
0.4	601.99	600.93	598.12	0.11	0.17	-0.21
0.2	602.04	600.96	597.89	0.16	0.20	-0.44
0.1	602.04	600.87	597.63	0.16	0.11	-0.70

Table 29. Reservoir elevation sensitivity analysis results.

Reservoir Elevation	Model Value			Relative Change		
	P1	P2	P3	P1	P2	P3
602.0	602.02	600.87	598.53	0.14	0.11	0.20
601.4	601.88	600.76	598.33	0.00	0.00	0.00
601.0	601.79	600.69	598.22	-0.09	-0.07	-0.11
600.0	601.61	600.55	597.93	-0.27	-0.21	-0.40
599.0	601.49	600.46	597.70	-0.39	-0.30	-0.63
598.0	601.43	600.42	597.56	-0.45	-0.34	-0.77
597.0	601.39	600.39	597.45	-0.49	-0.37	-0.88
596.0	601.35	600.35	597.34	-0.53	-0.41	-0.99
595.0	601.33	600.33	597.25	-0.55	-0.43	-1.08
594.0	601.29	600.31	597.17	-0.59	-0.45	-1.16

Table 30. Downstream elevation sensitivity analysis results.

Downstream Elevation	Model Value			Relative Change		
	P1	P2	P3	P1	P2	P3
592.5	601.91	600.81	598.46	0.03	0.05	0.13
592.0	601.90	600.79	598.42	0.02	0.03	0.09
591.5	601.89	600.77	598.37	0.01	0.01	0.04
591.1	601.88	600.76	598.33	0.00	0.00	0.00
590.5	601.86	600.72	598.25	-0.02	-0.04	-0.08

Table 31. Groundwater elevation sensitivity analysis results.

Groundwater Elevation	Model Value			Relative Change		
	P1	P2	P3	P1	P2	P3
606.0	602.94	601.82	599.07	1.06	1.06	0.74
605.5	602.59	601.47	598.84	0.71	0.71	0.51
605.0	602.23	601.12	598.60	0.35	0.36	0.27
604.5	601.88	600.76	598.33	0.00	0.00	0.00
604.0	601.54	600.43	598.08	-0.34	-0.33	-0.25
603.5	601.20	600.09	597.81	-0.68	-0.67	-0.52
603.0	600.85	599.73	597.50	-1.03	-1.03	-0.83
602.5	600.53	599.40	597.23	-1.35	-1.36	-1.10